Intravascular Fluorescence lifetime characterization of Atherosclerosis

Dissertation
(Kumulative Dissertation)

zur Erlangung des akademischen Grades
Doctor rerum naturalium (Dr. rer. nat.)

vorgelegt dem Rat der Chemisch-Geowissenschaftlichen Fakultät
der Friedrich-Schiller-Universität Jena

von M.Sc. Julien Bec
geboren am 1. April 1980 in Reims, Frankreich

1. Gutachter

_____

_____

2. Gutachter

_____

_____

3. Gutachter

_____

_____

Tag der öffentlichen Verteidigung: ___.___._____

Contents

List of tables and figures

List of abbreviations

AIT	Adaptive intimal thickening
AMI	Acute myocardial infarction
CCD	Charge coupled device
ECL	Extracellular lipids
ECM	Extracellular matrix
EFA	Early fibroatheroma
F	Fibrous tissue without calcification
FC	Fibrocalcific
FLIm	Fluorescence lifetime imaging
GRIN	Gradient index
HDL	High density lipoproteins
IVPA	Intravascular photoacoustic
IVUS	Intravascular ultrasound
IX	Intimal xanthoma
LAD	Left anterior descending artery
LDL	Low density lipoproteins
LFA	Late fibroatheroma
MCP-PMT	Microchannel plate photomultiplier
MDU	Motor drive unit
mFC	Macrophage Foam Cell
NIRF	Near infrared fluorescence
NIRS	Near infrared spectroscopy
NOR	Normal
PCI	Percutaneous coronary intervention
PIT	Pathologic intimal thickening
PR	Plaque rupture
RCA	Right coronary artery
SMC	Smooth muscle cell
TCFA	Thin cap fibroatheroma
US	Ultrasound

1. Introduction

Cardiovascular disease is one of the leading causes of death in western societies, and accounts for 1 in every four deaths in the United States [1]. Under this umbrella are several conditions, with a large subset related to atherosclerosis. This condition, characterized by the build-up of plaque in the arteries throughout the life of individuals, creates narrowing that can impede blood flow, but also cause heart attacks or strokes when these plaques release material in the blood stream that leads to clotting and complete obstruction of downstream arteries. Total coronary occlusion leads to cell death in the myocardium if blood flow is not restored shortly, by means of either thrombolytic therapy or percutaneous coronary intervention (PCI).

When atherosclerosis manifests itself by a stable reduction of blood flow, it leads to symptoms such as chest pain, discomfort or shortness of breath, and is easily diagnosed by clinicians. In this case, blood flow can typically be restored by PCI with the apposition of stents - metal or polymer scaffoldings - that support the narrowed vessel and restore sufficient cross section. Unfortunately, many patients are diagnosed with cardiovascular disease only when subject to a heart attack. This is due to atherosclerotic lesions that do not present a clinically significant lumen narrowing, such that a plaque rupture or erosion happens before any other symptoms that can lead to identification of the disease.

There currently isn't any reliable way to determine which patients are likely to experience acute myocardial infarction (AMI). Even for patients that have been subject to AMI, determining which lesions are likely to cause future event is challenging with current tools. Therefore, development of imaging techniques able to better characterize atherosclerotic disease may change patient care and lead to improvements in public health.

At the research level, the current understanding of the development of atherosclerotic diseases is based on retrospective autopsy studies as well as preclinical work in cell and animal models. The development of laboratory models that fully capture the complexity of a disease that evolves over decades is

challenging, and *in situ* investigation of atherosclerosis in patients is limited to a few imaging techniques, either full body or catheter based, that only provide limited information.

Therefore, clinical practice, development and evaluation of new therapeutic options, and basic research about atherosclerosis development would benefit from improved characterization techniques suitable for *in vivo* use.

1.1 Medical imaging

When performing diagnostics on patients, medical practitioners gather information through a variety of techniques. Some are basic, such as description of the symptoms by the patient, body temperature measurement, palpation, and have been used since the early days of medicine. Advances in science and technology have opened the way to new approaches, such as the analysis of bodily fluids (such as blood or urine samples), measurement of body functions (such as electrocardiography), tissue level diagnostics (histology), or medical imaging.

Medical imaging consists of creating visual representations of areas of the body that are not accessible via direct examination. It can for example reveal internal structures or functions and is a key component for the diagnostic and treatment of diseases. Most imaging techniques used in the clinical practice are non-invasive, meaning that the imaging instrumentation is outside of the patient's body. The most commonly used are radiography, ultrasound (US), magnetic resonance imaging (MRI), and computed tomography (CT). These techniques are complemented by less common methods such as nuclear imaging.

The choice of imaging technique depends on a variety of factors, namely safety, cost, ability of the contrast mechanism to provide relevant information to the medical practitioner. Not surprisingly, two of the most widespread medical imaging techniques, projectional radiographs (X-rays) and ultrasound are low cost, present negligible risks, and provide great insight into the body's interior structure. When alternative methods do not provide the level of information required for proper diagnostics, clinical practitioners will direct patients to imaging modalities such as MRI, CT, or nuclear imaging (positron emission

tomography or single photon emission computed tomography) that are more costly or present exposure to ionizing radiation. Finally, injection of high attenuation (e.g. iodinated) contrast agent can be combined with projectional radiographs and CT to address the lack of soft tissue contrast, leading to Fluoroscopy also known as X-ray angiography, and contrast enhanced CT respectively. A summary of these clinical non-invasive imaging techniques is provided in table 1.

Imaging Modality	Advantages	Drawback
Projectional radiography	• Low cost • low dose • high spatial resolution	• 2D only • no soft tissue contrast • No molecular contrast
Ultrasound	• Low cost • No exposure to ionizing radiation • Real time image display	• Trade-off between penetration depth and spatial resolution • No molecular contrast
CT	• High spatial resolution • 3D images	• Significant radiation exposure (10 mSv) • No soft tissue contrast
MRI	• 3D images • No exposure to ionizing radiation • Soft tissue contrast	• Limited spatial resolution • Limited acquisition speed • Cost
PET/SPECT	• Molecular contrast	• Requires suitable radiotracer • Exposure to ionizing radiation (25 mSv for PET) • Cost
Fluoroscopy	• High spatial resolution • Visualization of vessel lumen	• 2D only • Significant radiation exposure for multiple image acquisition • Use of potentially harmful contrast agent
Contrast enhanced CT	• High spatial resolution • Visualization of vessel lumen • 3D images	• Significant radiation exposure 20 mSv • Use of potentially harmful contrast agent

Table 1: Description of non-invasive imaging modalities

The availability of non-invasive imaging techniques has enabled breakthroughs in clinical decision making. Nevertheless, limitations in acquisition speed, contrast and spatial resolution mean that imaging of specific conditions is still out of reach from these modalities. Atherosclerosis, described in the following section, is one of

such conditions, and thus requires the development of alternate imaging approaches.

1.2 Basics of Atherosclerosis

The development of plaque, called atherogenesis, consists of a remodeling of the arteries that includes accumulation of lipids under the endothelium. This process is slow and progresses over the entire lifespan of individuals, starting during childhood, and typically does not lead to symptomatic manifestations before middle-age [2]. The development of lesions is complex and still not fully understood after decades of research but is thought to proceed in the following manner.

Circulating low density lipoprotein (LDL) particles accumulate in the endothelium and undergo oxidation via enzymatic action, leading to an inflammatory response. In turn, circulating monocytes are drawn into the sub-endothelial space and differentiate into macrophages [3]. When oxidized LDL gets ingested by macrophages, numerous small lipid inclusions develop into the cytoplasm. They increase in size and turn into macrophage foam cells (mFC). These mFC accumulations, called fatty streaks, may progress into advanced lesions but also regress on their own [2]. The path to more advanced lesions is understood to be driven by apoptosis of these foam cells that release cholesterol in the extracellular space and promote further inflammation. The rate of accumulation of free cholesterol in the endothelium is influenced by the protective effect of high-density lipoproteins (HDL), able to transport cholesterol back into the bloodstream and ultimately to the liver and other organs.

Early fibroatheroma, characterized by the apparition of extracellular lipid pools and decreased cellularity, is considered the first step of atherosclerosis. In that phase, characterized by high levels of inflammation, smooth muscle cells (SMC) secrete proteoglycans in the extracellular space. Lipids bind to these proteoglycans with high affinity and continue to accumulate [4]. The creation of lipid pools leads to mFC and SMC apoptosis, thus generating necrotic debris that increase inflammation. Fibrous tissue also develops close to the endothelium and lead to the typical fibrous plaque lesion, with a lipid-rich necrotic core.
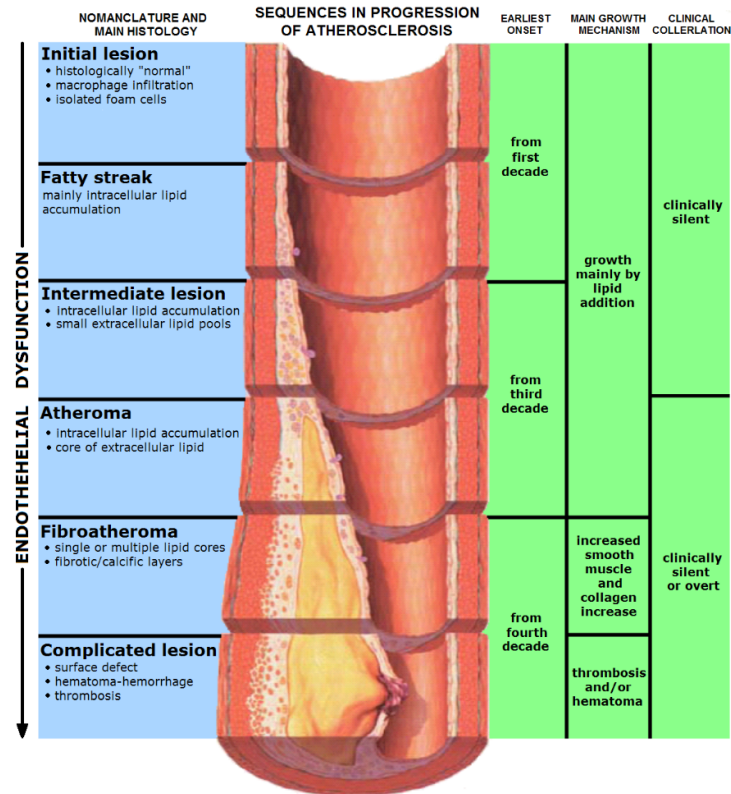
Figure 1: Illustration of different stages of development of atherosclerosis. Endo dysfunction Athero, CC BY-SA 3.0

It can be noted that the increase in plaque thickness does not necessary correspond to a reduction in vessel cross section (stenosis) as media and adventitia are also impacted and expand in a process called outward remodeling. Outward remodeling enables plaque burden accumulation while remaining clinically silent.

In later stages of the disease, enzyme activity degrades the fibrous tissue, and leads to thin cap fibroatheroma (TCFA). The decrease of cap thickness increases the risk of rupture and release of thrombogenic material into the blood stream. The common occurrence of layered lesions created by cycles or rupture and healing indicates that ruptures infrequently lead to clinical manifestation and are an integral part of the plaque development process.

Calcification also appear during this process, typically at the interface between medial SMCs and atherosclerotic lesions [5]. The exact mechanism for vascular calcification is still unknown and subject of active research. Although calcifications have a thrombogenic effect when exposed to the blood stream, they may also have a stabilizing effect on the plaques. Calcifications are one of the hallmarks of disease progression, but they are not always present and are not necessary for the occurrence of cardiac events.
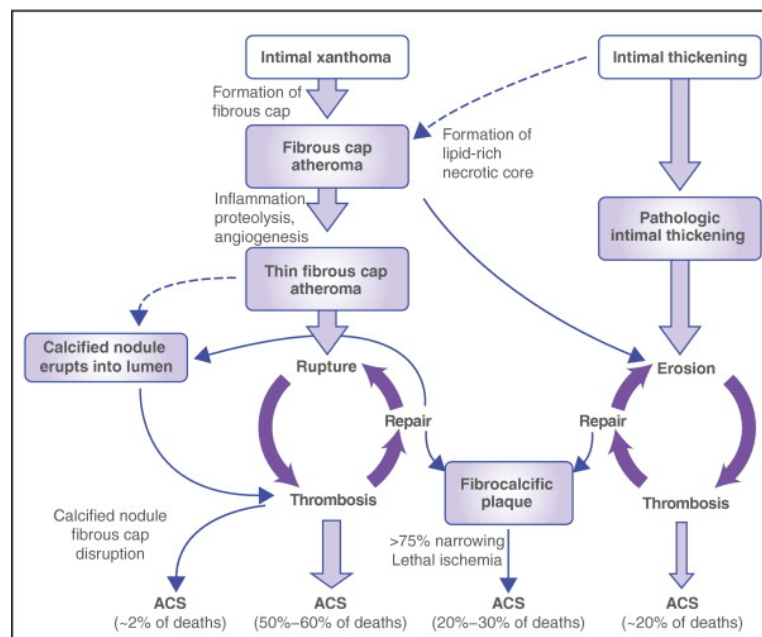
Figure 2, Flow chart of the general concepts of the development of atherosclerosis. Reprinted from The American Journal of Medicine, 122/1, W. Insull, The Pathology of Atherosclerosis: Plaque Development and Plaque Responses to Medical Treatment, S3-S14, Copyright (2009), with permission from Elsevier

Causes for the development of atherosclerotic disease described above are systemic, but certain locations are more likely to develop lesions . More specifically, studies of plaque rupture locations show that one of the critical locations is the upper section of the left anterior descending and left circumflex arteries, typically within 50 mm from the ostium [6]. Local hemodynamic properties, influencing shear stress on the endothelium as well as stress within the vessel wall have been

linked to lesion initiation, development and destabilization through a variety of processes [7].

1.3   Imaging of atherosclerosis

Clinical manifestations of atherosclerosis only occur when blood circulation is restricted or blocked, in the cases of angina pectoris and myocardial infarction respectively [2]. In both cases, the distribution of iodinated contrast detected using fluoroscopy enables easy identification of the stenosed or blocked location and is generally sufficient to perform medical intervention.

Unfortunately, fluoroscopy does not enable the identification of high-risk lesions. Lesions are extensively distributed throughout the vasculature but only few select locations present high-risk features (thin cap, superficial thrombosis, rupture). Additionally, these high-risk lesions are not necessarily associated with a higher degree of stenosis. Therefore, medical treatment of atherosclerotic disease is either reactive (stenting, thrombus removal following AMI) or based on lifestyle and lipid lowering drugs (statins).

Atherosclerotic lesions are typically small (few mm^3), and the locations of the coronary arteries, at the surface of the heart, lead to intense motion due to the myocardium contraction, making imaging of atherosclerosis using noninvasive methods very challenging. Among these efforts, quantification of calcification as a surrogate for disease risk assessment using CT has been performed with limited success [5,8]. Although nuclear imaging is well suited to the study of metabolic disease and inflammation with an array of dedicated radiolabeled probes, the limited spatial resolution and long acquisition times has hindered adoption for imaging of coronary artery disease. MRI faces similar issues of motion artifacts and lack of spatial resolution. Although non-invasive imaging techniques present clear benefits, and advances in instrumentation performance are pushing the boundaries of temporal and spatial resolution, currently available instrumentation is still not suitable for the clinical evaluation of atherosclerosis.

Given the many challenges in performing noninvasive imaging of coronary atherosclerosis, alternative catheter-based imaging techniques have been

developed over the last 25 years [9]. The first of these imaging modalities to have seen clinical adoption is intravascular ultrasound (IVUS). IVUS catheters consist of a small (<1 mm diameter) high frequency ultrasound transducer (20-60 MHz) mounted at the distal end of a rotating imaging coil (typically 30 rotations per second). IVUS enables the acquisition of cross-sectional images of the vessel. A 5-10 mm penetration depth and ~100 μm axial and lateral resolution [9] enables assessment of vessel stenosis, and plaque burden, but limits the detection of small features such as the plaque thickness of TCFA. Additionally, lipid rich lesions are characterized by low signal reflection (hypoechoic region), whereas calcifications appear very distinctly (hyperechoic). Although this information is a clear step forward compared to fluoroscopy, spatial resolution as well as ability to determine plaque composition ultimately do not allow a thorough assessment of lesion characteristics [10]. Quantitative radiofrequency analysis of the backscattered signal showed promising results for the determination of lesion composition but has not been widely adopted in clinical practice [11]. Current advances in IVUS technology include the development of multiple frequency devices that aim at combining penetration depth enabled by lower frequency transducers (30-50 MHz) with the axial and lateral resolution of high frequency transducers (up to 120 MHz) [12].

Optical Coherence Tomography (OCT) is a technique that can be considered an optical analog of IVUS, as it relies on near infrared (typically 1300 nm) backscattered light to generate contrast. In a similar fashion to IVUS, OCT enables depth-resolved measurement along the line of sight (A-line), and cross-sectional images (B-Scan) are obtained by rotation of the device's optical core. A very active research field has led to steady improvements in OCT performance, driven by advances in light sources and detection scheme that leverage innovations in the telecommunication sector. Key features of current intravascular OCT systems are the high A-line rate (>25 kHz) that enables data acquisition at high speed (>100 frames per second), and outstanding axial and lateral resolution (10-30μm). Unfortunately, this is achieved at the detriment of the penetration depth (1-2 mm), that does not enable the assessment of the overall plaque burden in advanced lesions. Additionally, the high scattering of red blood cells at 1300 nm requires

flushing of the blood from the artery segment during imaging. This is typically performed by a 10-20 cc bolus injection of iodinated contrast.

The limitation of OCT and IVUS as standalone imaging techniques have led to the development of hybrid catheter imaging systems that aim to provide improved assessment of plaque characteristics. An obvious combination is IVUS and OCT, that combines the ability to assess overall plaque burden with the exquisite spatial resolution of OCT for the assessment of superficial lesion characteristics. Another direction for multimodal devices has been to combine a morphological imaging technique such as IVUS or OCT with an imaging modality able to provide compositional information. The section below will detail some of these approaches and their expected performances for the assessment of atherosclerotic lesions.

Imaging modalities	Features associated with increased plaque vulnerability						Current status
	Lumen dimensions	Plaque burden and positive remodeling	Lipid component	Cap thick.	Neo-angiogenesis	Inflammation	
NIRS-IVUS	+++	+++	+++	++	-	-	Commercially available
IVUS-OCT	+++	+++	++	+++	++	+	In vivo validation
OCT-NIRF	+++	+	++	+++	++	+++	First in man studies
IVUS-NIRF	+++	+++	+	+	-	+++	Under development
OCT-NIRS	+++	+	+++	+++	++	+	Ex vivo validation
IVUS-IVPA	+++	+++	++	+	+	++	Ex vivo validation
IVUS-FLIm	+++	+++	++	+++	-	+++	In vivo validation

Table 1. Multimodal intravascular imaging comparison. (+++) indicates excellent performance of the modality; (++) moderate performance of the modality; (+) poor performance of the modality; (2) the modality is unable to provide this information; IVUS, intravascular ultrasound; RF-IVUS, radiofrequency analysis of the IVUS backscattered signal; OCT, optical coherence tomography; NIRS, near infrared spectroscopy; NIRF, near infrared fluorescence imaging; IVPA, intravascular photoacoustic imaging; FLIm, fluorescence life time imaging. Adapted from European Heart Journal, 122/1, C. Bourantas, Hybrid intravascular imaging: recent advances, technical considerations, and current applications in the study of plaque pathophysiology, Copyright (2016), with permission from Oxford University Press

Near infrared spectroscopy (NIRS) consists in measuring the absorption spectrum of the arterial wall in the near infrared. It is well known for the ability to characterize lipids and therefore was identified early as a promising approach to identify high risk lesions assumed to be characterized by a large lipid content. Intravascular implementation is performed using two side viewing fiber for light delivery and collection, axially offset such that most of the light propagates through the arterial wall before being collected. A NIRS-IVUS device has been clinically available since the mid-2000s [13] and the ability of the device to predict plaques likely to cause future events are currently being evaluated in clinical trials.

A competing approach also aimed at detecting lipids in the lesions is intravascular photoacoustic (IVPA). Here, pulses of infrared light (typically 1720 nm) are sent to tissue, and absorption of the light leads to local thermal expansion that generate ultrasound waves detected with an ultrasound transducer. Because the presence of the transducer is required for IVPA, combination with IVUS is straightforward. IVPA provides depth resolved information, a clear advantage compared to NIRS where periadventitial adipose tissue may in some cases be mistaken for lipid rich atherosclerotic lesions. Nevertheless, successful implementation for *in vivo* use requires the development of suitable high frequency light sources and is currently the object of active work. Lipid specificity may benefit from the use of dual-wavelength excitation to perform spectroscopic photoacoustic [12]. Safety issues with the delivery of high average power to tissue are significant and may also hinder clinical translation [14]

Another promising approach to further the understanding of atherosclerosis processes is near infrared fluorescence (NIRF). It can detect biological processes with high specificity by combining molecular imaging probes, with dedicated imaging devices. This approach relies on near infrared excitation (typically 750 nm), to take advantage of the higher penetration depth and reduced tissue autofluorescence generated by the excitation light. It has been implemented in combination with both OCT and IVUS. Combination with OCT is particularly

interesting as a single double clad fiber is used for both imaging modalities, enabling integration into devices with the same profile as standard clinical OCT catheters. Additionally, combination with OCT compares favorably with IVUS because both imaging modalities are inherently co-registered as they share the same light path [15]. Co-registration is a key feature as the fluorescence signal is dependent on the distance between the device and the vessel wall and must therefore be corrected to provide information about the probe concentration in tissue. Typical applications of NIRF-OCT are the detection of fibrin, a molecule associated with thrombus, to assess the risk of thrombus formation following stent implantation, or the detection of inflammation using a cysteine protease-activatable NIRF imaging agent [16]. The reliance on molecular probes is creating regulatory challenges that limit the translation potential in human, as few molecular probes are currently cleared for use in human.

Fluorescence lifetime imaging (FLIm) relies on excitation of endogenous fluorophores using pulsed UV light to provide tissue compositional information. This technique presents key features that make it a compelling choice to perform coronary artery disease lesion assessment when used in combination with a morphological imaging technique such as IVUS or OCT. The ability to perform time resolved measurement of fluorescence emission over a plurality of wavelength bands enables the identification of different fluorophores. Both lifetime and spectral information is ratiometric by nature and is therefore not directly impacted by changes in excitation/ collection geometry due to varying probe to vessel wall distance over the field of view. It is necessary to flush blood from the imaged area as blood absorption is high in the UV-visible range. This constraint is shared with OCT, routinely used in clinical practice. FLIm can be implemented in various ways, including full field or fiber-based point scanning techniques. The latter is most relevant for the implementation of FLIm as an intravascular imaging technique. Successful implementation relies on the development of high-speed data acquisition methods, and development of dedicated imaging catheters, described in section 2.

An alternative technique to fluorescence for the identification of tissue composition is Raman spectroscopy. This optical technique consists in the delivery of monochromatic light to a sample, and precise spectrally resolved measurement of the scattered light. The scattering phenomenon consist of Rayleigh scattering, also called elastic scattering, where photons change direction but maintain their energy, and therefore wavelength, and inelastic scattering, where photon energy is changing. Scattering leading to a decrease in energy, corresponding to an increase in wavelength, is called stokes Raman scattering, whereas in increase in energy, leading to a reduction of wavelength, is caused anti-stokes Raman scattering. The study of inelastic scattering component of light exiting the tissue provides information related to chemical bonds. Because different bonds lead to different levels of inelastic scattering, spectral properties of the inelastically scattered light provides information about chemical composition of samples. The information provided by Raman spectroscopy is typically much more specific than information provided by fluorescence, but implementation is challenging: only a small fraction of incoming photons undergoes inelastic scattering so signal levels are low, thus requiring extended acquisition time compared to fluorescence, and rejection of elastically scattered light is critical. Additionally, the collected signal also includes autofluorescence contribution, typically orders of magnitude higher than Raman contributions, as well as Raman background generated within the instrument, removed during post processing. Raman is widely implemented as a microscopy technique [17] but fiber-based implementations are possible [18,19]. The fiber probe design needs to enable rejection of inelastically scattered light and Raman signal generated with the fiber itself, and maximize collection efficiency, and is thus consists of fiber bundles with integrated dielectric filters, limiting the possibilities of miniaturization. For the same reasons, implementation as a side viewing probe able to perform helical scanning is yet to be achieved. Although implementation of Raman spectroscopy into a device compatible with spectroscopic interrogation of the coronary vasculature is unlikely in the near future, the ability of Raman signal to provide label free, non-invasive detailed compositional information makes it a compelling tool for cardiovascular research applications.

1.4   Outline of thesis

Successful implementation of FLIm for intravascular imaging relies on the development of dedicated instrumentation and data processing techniques. The second chapter of this work will focus on the different stages of the development of such instrumentation. This includes the implementation of a high speed FLIm data acquisition subsystem, the description of the integration of the FLIm subsystem with an IVUS clinical platform for combined morphological and compositional information, and the design, fabrication and testing of bimodal FLIm-IVUS catheters. Optical performances of intravascular FLIm catheters are limited using conventional distal end optics, so a novel freeform side viewing optic has been developed specifically for this application to address the shortcomings of the first multimodal FLIm-IVUS catheter design. The design and performances evaluation of this improved device are presented. Finally, a combined FLIm-Raman integrated imaging system used for comparative imaging studies of coronary artery samples will be described.

The instrumentation developed for this project enabled original imaging studies. In a third chapter, we will describe the evaluation of the FLIm-IVUS imaging system *in vivo* in animal model, followed by a study on diseased human coronary samples, aimed at furthering the understanding of sources of FLIm contrast. Results from comparative imaging of diseased human coronary samples using both FLIm and Raman spectroscopy will be presented.

A summary of the key results and findings of this work will be presented in English and German in the fourth and fifth chapter, respectively.

2. Optical instrumentation development

2.1   Basics on fluorescence and time resolved fluorescence

Fluorescence describes the effect where light is temporarily absorbed by a molecule and reemitted at a longer wavelength. More specifically, incoming electromagnetic

radiation energizes an orbital electron from the ground state to an excited singlet state. The relaxation to the ground state may lead to the emission of another photon. The path to the ground state may include non-radiative transitions (vibrational relaxation) such that the energy of the emitted photon is inferior to the energy of the absorbed photon, leading to a red-shifted emission called stokes shift.
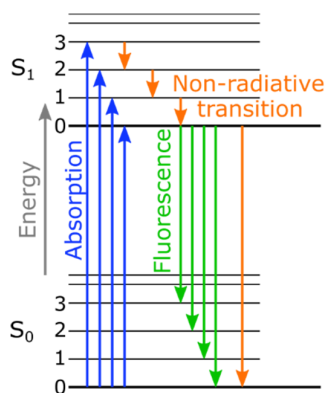
Fig. 3. Simplified Jablonski diagram that illustrates the transitions corresponding to the absorption and emission of photons observed during fluorescence processes.

A fluorescent molecule can absorb and emit photons over specific wavelength ranges, determined by the available energy levels. This characteristic means that the fluorescence absorption and emission spectral properties may be used to identify fluorescence molecules.

Additionally, the molecule remains in the excited state for a short duration before transitioning back to the ground state. This decay time varies between molecules and a measure of this property provides additional information that can be used in addition to spectral properties to discriminate different fluorophores.

Biological fluorophores typically present wide overlapping emission spectra, so identification of species based on spectral properties alone is challenging (figure 4). Adding lifetime provides therefore a useful additional dimension to generate tissue contrast.
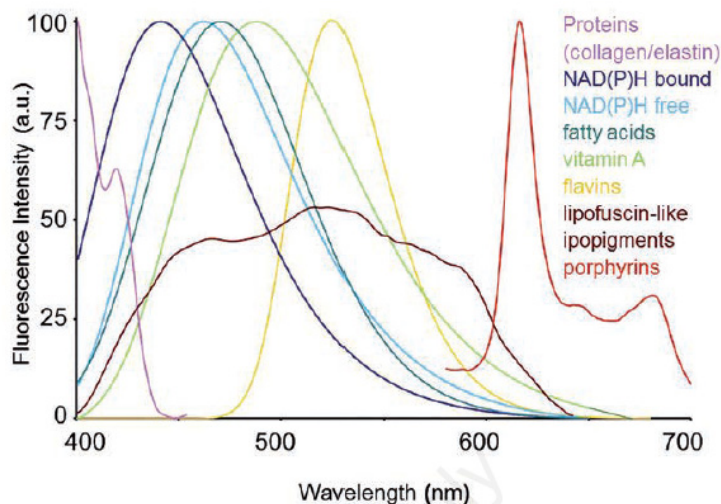
Figure 4, Emission spectra of principal endogenous fluorophores encountered in autofluorescence studies. Reprinted from *European Journal of Histochemistry*, *58*(4), Croce, A., & Bottiroli, G. Autofluorescence spectroscopy and imaging: a tool for biomedical research and diagnosis, Copyright (2014). CC 4.0

2.2   Overview of possible implementations

Measurement of the wavelength properties is typically done by either dispersing the light using a prism or grating, or filtering the light using discrete filters, to measure the amount of emitted light at different wavelengths. As described in the previous section, this information can be complemented by the measurement of the fluorescence decay rate or lifetime. This phenomenon happens over a few nanoseconds, so dedicated fast instrumentation is required.

The most common implementation, use routinely for microscopy applications, is time correlated single photon counting [20]. In this method, short (tens of picoseconds) light pulses are sent to the sample. Fluorescence light is collected and sent to a fast photodetector. Excitation pulse energy and instrument collection efficiency are set so that at most one fluorescence photon is detected for each excitation pulse. For each collected photon, the instrumentation can precisely determine the delay between the excitation pulse and the arrival of the fluorescence photon. By reproducing this process over hundreds to thousands of photons, it is possible to build a histogram of fluorescence photon arrival times, from which fluorescence decay properties can be derived. This method enables the

acquisition of high statistics data because there are few limits to how many photons can be collected from the sample. The main drawback is a slow acquisition speed, even with high repetition rate light sources. An alternative method is to use a gated detector, where the gate, synchronized with the excitation laser, is controlled by an adjustable delay mechanism such that different delay steps cover the whole decay time and enable recovery of the complete decay profile.

With both methods, many excitation pulses are required to reconstruct the fluorescence decay of a single measurement point, a major disadvantage for imaging in intravascular setting where tissue is rapidly moving and where imaging acquisition needs to be performed while flushing blood from the imaging area.

For this work, we have used a time resolved fluorescence measurement technique that enables acquisition of fluorescence decays over multiple spectral bands from a single excitation photon. This technique, refined over more than 10 years of development at UC Davis and other research institutions, will be described in the following section [21,22].

2.3   *High speed FLIm instrumentation*

The approach used here is described as a pulse sampling technique [23]. It is conceptually simple: the fluorescence emission, generated by a high energy excitation pulse (~µJ/pulse), is sampled by a high-speed digitizer. It is fast because each target location can be characterized by a single excitation pulse. This scheme relies on the availability of fast, high gain photodetectors such as microchannel plate photomultipliers (MCP-PMT) and high bandwidth and high sampling rate electronic, and the quality of the data is limited by the ability to collect a high number of fluorescence photons from each excitation pulse.

Earlier implementations of pulse sampling time resolved fluorescence relied on Nitrogen lasers, able to generate 337 nm pulses of sub-nanosecond duration (~700 ps), and high energy (up to 100 µJ), albeit at lower repetition rate (30 Hz typical) [24]. Because of the high pulse energy, the optical throughput of the excitation and collection paths of the instrument are not critical. This type of laser

is well suited for point measurements, where the ability to perform single wavelength measurements in less than a second is sufficient. When combined with a scanning spectrometer or filter wheel to perform wavelength resolved measurements, the scanning speed of the spectrometer (mechanical rotation of the grating) or rotation of the filter wheel is a limitation so a laser repetition rate of tens of Hertz is again sufficient.

Time resolved fluorescence images are created by the combination of many individual point measurements, at least hundreds of points, and typically thousands, depending on the size of the area of interest and the required spatial sampling. Laser repetition rate becomes therefore a key factor for a practical implementation of fluorescence lifetime imaging. Imaging of *ex vivo* samples can be performed over several minutes because the main limitations to a prolonged data acquisition sequence are drying of samples and limited throughput when imaging many samples. As discussed in previous sections, optical imaging in intravascular setting requires to displace blood from the field of view by means of a flushing agent. This is especially true for fluorescence when using UV excitation, because of the high extinction coefficient of blood in the UV region (~485 cm-1 at 355 nm) [25]. Bolus injection of flushing agents are well accepted in clinical practice [26] but limit the duration of an imaging sequence to a few seconds. To enable the acquisition of fluorescence lifetime images in such short time frame, we adopted 355 nm pulsed UV fiber laser (80 ps pulses, Fianium, UK) with a repetition rate of 20 KHz.

As described earlier, the ability to perform time resolved fluorescence measurements over different wavelength bands is key to enable differentiation of various fluorophores. This is achieved here by splitting the fluorescence signal in four bands using a combination of dichroic mirrors and bandpass filters. This compares advantageously to scanning monochromators or motorized filter as this arrangement does not require moving parts and all spectral bands can be acquired simultaneously. Because pulse sampling methods relies on costly high-speed detectors and sampling electronics, simply duplicating the detection channels for each wavelength range of interest is not practical. Instead, the system includes

varying lengths of delay fiber that perform temporal multiplexing, such that the fluorescence light from different spectral bands reaches the photodetector delayed in time. The incremental length of the delay fibers is determined to generate sufficient delay (45 ns) to prevent overlap between signals of different spectral bands.

The photodetector used for this instrument is a multialkali photocathode MCP-PMT (R3809U-50, Hamamatsu, Japan). This device presents a short rise time (160 ps), a low transit time spread (25 ps), and a photocathode area suitable for the coupling of light delivered by the four delay fibers (11 mm diameter). The PMT is coupled to a 40 dB gain, high bandwidth (3GHz) amplifier (AM-1607-3000, MITEQ, NY) and the resulting signal is then sampled by a high-speed digitizer (12.5 GS/s, 3 GHz, 8-bit, 512 Mbytes, PXIe-5185, National Instruments, Austin, TX).
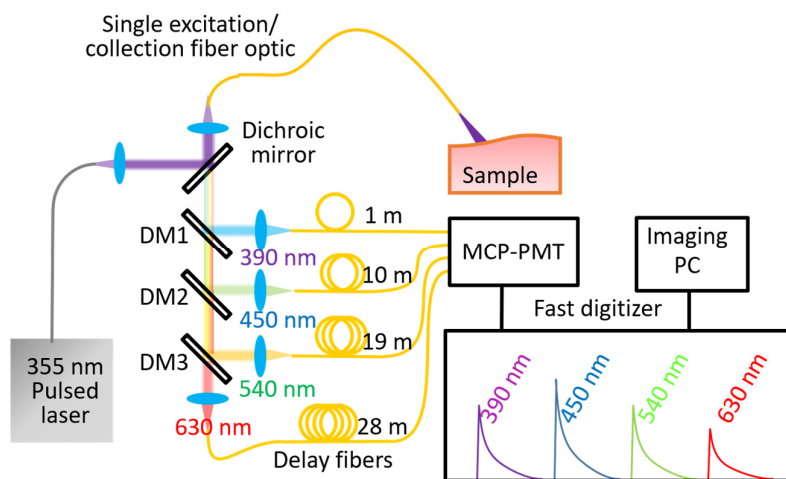
Figure 5: Schematic of multispectral time resolved fluorescence lifetime measurement instrumentation. A single photodetector and high-speed digitizer are used for the acquisition of time resolved fluorescence in four different spectral bands from a single excitation pulse, using a temporal multiplexing scheme implemented with varying lengths of delay fibers.

2.4   FLIm-IVUS instrumentation requirements for in vivo use [P1]

The FLIm acquisition system above relies on a single multimode fiber for delivery of the excitation light as well as collection of the fluorescence signal generated by

the tissue. This implementation is much easier to integrate into miniature imaging probes than the fiber bundles using separate fibers for the excitation and collection paths that are typically used for such measurements. This enabled the fabrication of a low profile FLIm-IVUS imaging device reported previously [27]. Unfortunately, this previous system relied on separate FLIm and IVUS imaging cores, integrated in a dual lumen device that performed sequential scanning of the sample. This approach is well suited to imaging of *ex vivo* samples [28] but not to acquire co-registered FLIm and IVUS data in presence of motion, a key requirement in an imaging system developed for *in vivo* use.

A suitable fully integrated FLIm-IVUS catheter system requires:

- An integrated imaging catheter where both imaging modalities are packaged into a single imaging core.
- An integrated motor drive unit (MDU) to perform imaging core rotation and ultrasound radiofrequency as well as optics rotary coupling
- An integrated data acquisition system

The different elements of the system will be described in the following sections.

2.5   Integrated FLIm IVUS imaging catheter

Coronary arteries are characterized by an inner diameter of 3-5 mm at the ostium (branching location from ascending aorta) that reduces further as they branch out. Intravascular imaging devices for the imaging of atherosclerosis are not required to be able to image each artery segment. The distribution of critical lesions is following patterns and is highest in the upper sections of the left anterior descending artery (LAD), right coronary artery (RCA), and circumflex artery (see figure 6). In these locations, the inner diameter of healthy arteries is ~3 mm, but stenosis due to development of atherosclerotic lesions leads to a reduction in vessel lumen sizes, that dictates a typical imaging section diameter of ~1 mm (see table 2).
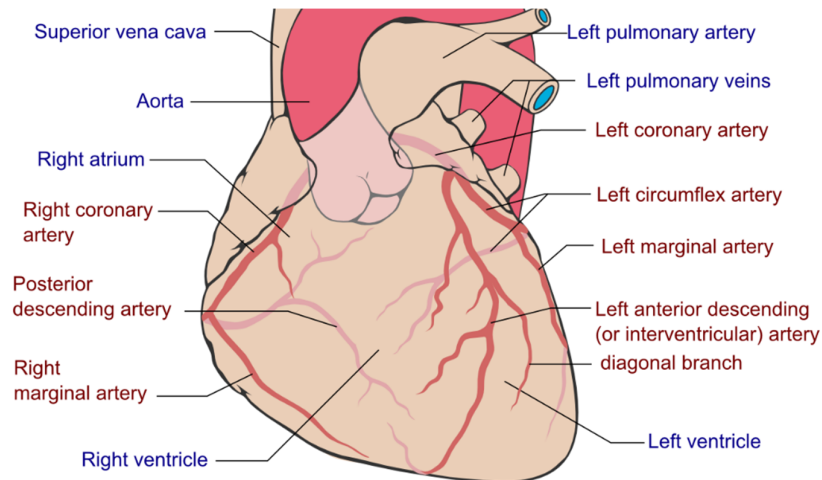
Figure 6. Anatomical terminology of coronary vasculature. Coronary.pdf: Patrick J. Lynch, medical illustrator derivative work [1]: Fred the Oyster (talk) adaption and further labeling: Mikael Häggström - Coronary.pdf, CC BY-SA 3.0

Other common features are a working length of ~135 cm to access the coronary arteries via femoral access, and an integrated pullback system that enables the combined translation and rotation of the imaging core within the device's sheath to perform helical scanning without displacement of the sheath with respect to the vessel.

Name (Manufacturer)	Modality	Crossing profile (F)	Frame rate (fps)	Pullback speed (mm/s)
Dragonfly C7(Abbott)	OCT	2.7	100	25
OptiCross (Boston Scientific)	IVUS	3.1	30	1
Revolution (Philips)	IVUS	3.2	30	1
TVC-MC9 (InfraredX)	IVUS+NIRS	3.2	16	0.5
FLIm-IVUS (UC Davis)	**IVUS+FLIm**	**3.6**	**30**	**4-10 mm/s**

Table 2. Characteristics of some clinical intravascular devices currently available for imaging of coronary arteries, and custom FLIm-IVUS catheter. Intravascular devices cross section dimensions are typically expressed in French (F), a measure of distance defined as one third of a millimeter.

Finally, the devices must be able to function in presence of sharp bends (bending radius < 15 mm), commonly encountered at the coronary ostium and within the coronary artery tree.

The integrated FLIm-IVUS catheter designed for this project [P1] was derived from a clinical IVUS catheter (Boston Scientific OptiCross). The imaging core, described in figure 7 is composed of custom distal-end housing and torque coil, and a hub that provides a mechanical connection for rotation as well as an electrical and optical interface. The ultrasound channel consists of a 40 MHz ultrasound transducer located in the distal section of the housing. The optical channel consists of a 200 µm core high-OH fused silica fluorine doped multimode fiber, terminated with an aluminum coated prism. Both channels are disposed in a tandem configuration, with reduced axial offset (450 µm from the center of the transducer to the center of the prism). To further improve coregistration, the ultrasound beam is tilted by 4º backward, whereas the prism is integrated with fiber to provide a 10-degree forward tilt of the optical beam, to achieve an overlap of the beam at a distance of ~1 mm. The tilt of the ultrasound transducer presents the additional benefit of limiting back-reflection artifacts from the device's sheath.

Manufacturing of the probe is a delicate, multi-step process. The ultrasound is first bonded into the housing and wired using a thin coaxial cable (46 Ga). Electrical connections between wire core and gold anode of the transducer, and wire shield and conductive backing of the transducer (cathode) are performed with conductive silver epoxy. The pre-assembled fiber optic and prism are then aligned and bonded into the housing. Both fiber and coaxial cable are inserted into the torque coil, bonded to the distal housing with cyanoacrylate adhesive. The proximal end of the torque coil is then bonded to the hub. The coaxial cable is connected to a small high-frequency filtering printed circuit assembly located inside of the hub that integrates the electrical pins visible in figure 7. The proximal end of the fiber optic is routed through an opening inside of the printed circuit assembly and inserted and bonded into the ferrule and polished in place. The distal end housing and torque coil are custom elements fabricated to accommodate the two imaging channels, leading to an increase of the imaging core diameter (FLIm-IVUS: 830 µm, Boston Scientific OptiCross: 570 µm).
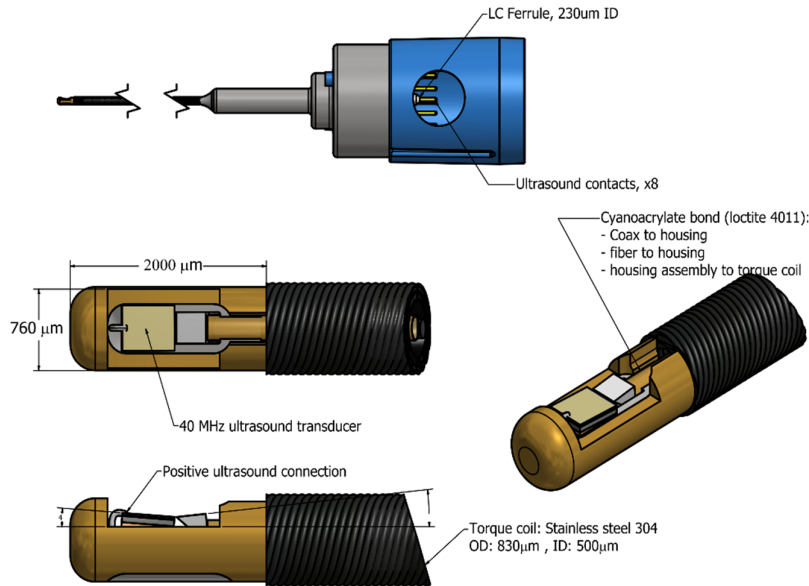
Figure 7. Details of the FLIm-IVUS catheter imaging core. Top view: complete imaging core with details of electrical and optical interfaces integrated in the hub. Bottom view: close-up of the imaging core distal end illustrating the integration of ultrasound and optical channels.

The sheath, described in figure 8, is composed of a shaft and telescope. The telescope is directly derived from the OptiCross IVUS catheter whereas the shaft has been adapted to fulfill the requirement of the FLIm-IVUS device. It presents a larger inner diameter (1.02 mm) required to accommodate the increased dimensions of the imaging core, and the shaft imaging section consists of a custom polymethylpentene extrusion (MX004, Mitsui Chemicals) that presents both low ultrasound impedance (~1.8 Mrayls) and suitable optical properties (high transparency, low autofluorescence).
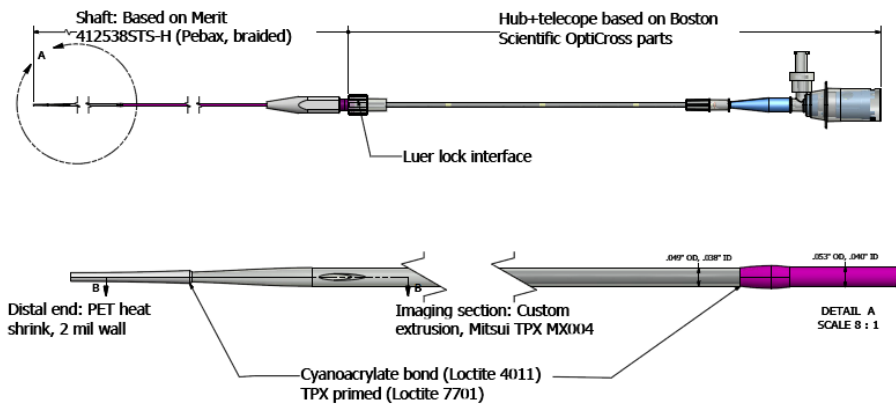
Figure 8: Details of the FLIm-IVUS imaging sheath. The imaging section has a section of 3.7 Fr and enables a 50 mm pullback.

2.6   Integrated FLIm-IVUS motor drive unit

The motor drive unit provides rotation and pullback motions and integrates a rotary interface for the ultrasound radiofrequency signal as well as the optical channel. It is derived from a clinical Boston Scientific motor drive, extensively modified to accommodate an optical channel. The modifications, visible in figure 9, consist in a modification of the catheter shaft to include a spring-loaded intermediate fiber optic stub for reliable connection with the optical channel of the catheter hub (label 1). The fiber stub extends to the end-face coupled rotary joint located in the handle of the MDU (label 2), for transmission of the optical signal to the WSM via a fiber optic patch cord (label 3). The motor and gearbox that drives the rotation of the shaft was offset with a gear train to enable the positioning of the rotary joint in line with the shaft (label 4). Finally, the pullback motor was modified to achieve increased pullback speeds required for FLIm imaging (label 5). Despite these modifications, the FLIm-IVUS MDU keeps similar dimensions as the original MDU and is compatible with all accessories of the Boston Scientific MDU (pullback sled, sterile bag).
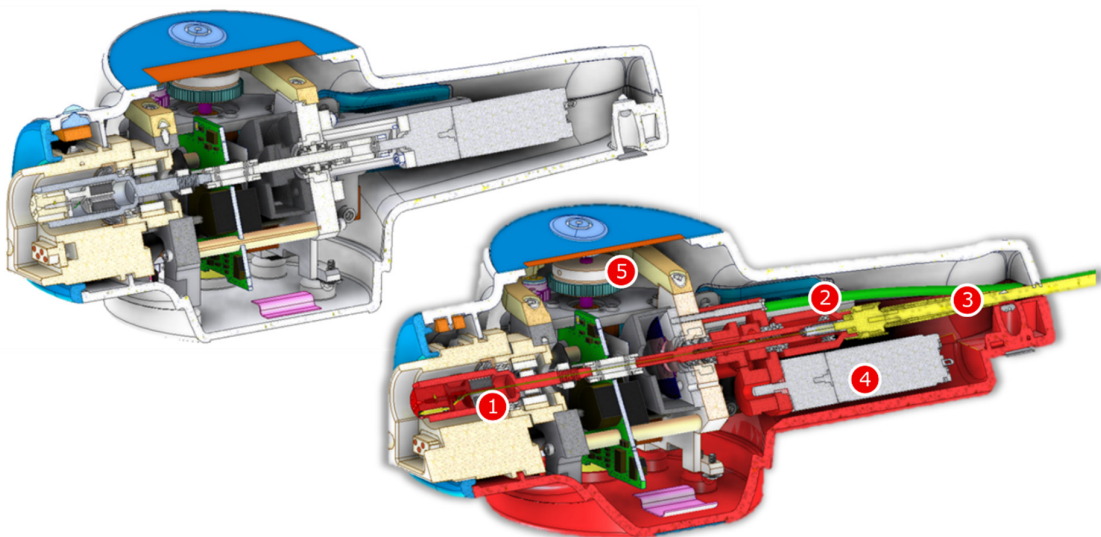
Figure 9: MDU modifications. Left: original motor drive unit (MDU). Right: modified MDU. Parts modified to integrate an optical channel with rotary joint are highlighted in red.

2.7 Integrated FLIm and IVUS data acquisition

The FLIm-IVUS system is closely derived from the clinical IVUS system (iLab) and leverages the clinical user interface to provide real time display of IVUS images: it is therefore possible to use IVUS images guide the positioning of the FLIm-IVUS catheter to an area of interest, before proceeding with a bimodal acquisition sequence. A drawback of the clinical console is that no external synchronization is available, and therefore the IVUS data obtained from the clinical console cannot be co-registered with FLIm data. To address this key requirement, the iLab acquisition unit was modified to provide an analogical IVUS signal output, connected to a dedicated digitizer synchronized with the FLIm digitizer (see figure 10). During bi-modal scans, IVUS and FLIm signal are synchronized to less than a microsecond. The combination of spatial registration of FLIm and IVUS data, enabled by the overlapping imaging beams, and precise synchronization of the data acquisition of both modalities enables the acquisition of a perfectly co-registered multimodal dataset.
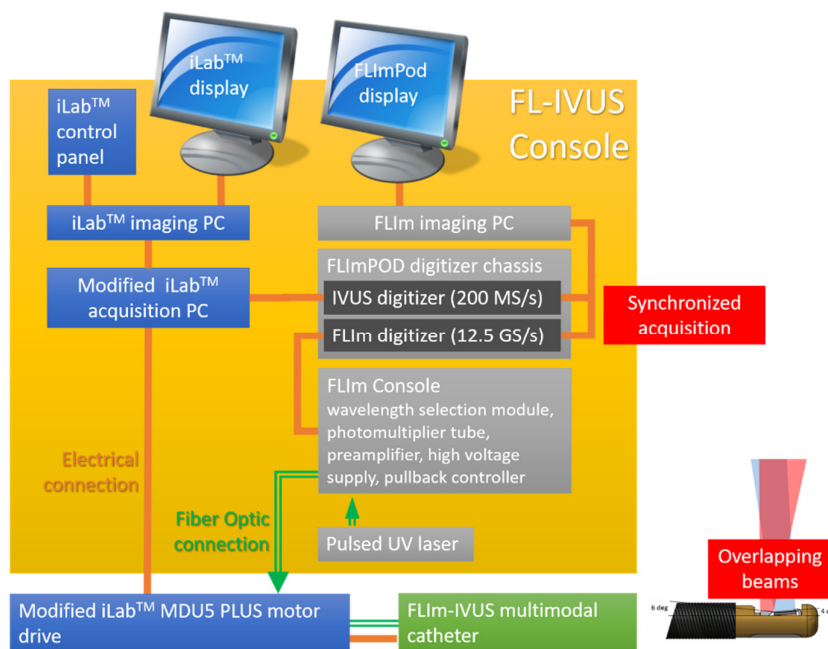
Figure 10: Description of the data acquisition scheme that enables the acquisition of co-registered FLIm and IVUS data using a combination of overlapping imaging beams and synchronized data acquisition.

The frame rate of the IVUS system is determined by the rotation speed of the imaging core of 30 turns per second. The FLIm-IVUS acquisition sequence was fixed at 5 s, a duration compatible with blood clearing using a bolus injection. It consists therefore of 150 ultrasound B-scans (cross sectional images). Each B-scan is composed of 256 ultrasound depth resolved measurements (A-scans). The FLIm subsystem sends UV excitation pulses at a frequency of 20 kHz, thus leading to 100 000 measurements in the same 5 s period. Data processing was performed using a 4-fold average to increase signal to noise ratio, leading to 25 000 independent FLIm measurements. This corresponds to 167 measurements per catheter rotation.

2.8   FLIm and IVUS data processing

A typical approach for extracting fluorescence decay parameters consists of using multi-exponential techniques [29]. Exponential functions match the relaxation dynamics of fluorescence systems, but because the formulation is non-linear with respect to decay parameters, least square evaluation of coefficients requires computationally intensive iterative optimization. Here, FLIm data was processed using a constrained least square Laguerre basis expansion technique [30]. Weighted Laguerre polynomials form an orthogonal basis of function that have applications in dynamic systems modeling [31]. When performing least square deconvolution with Laguerre expansion, fluorescence decays are expressed as a linear combination of Laguerre basis functions and thus estimation of expansion coefficients is comparatively simpler than multiexponential methods. A drawback of the Laguerre approach is that the basis functions present oscillations, so estimations of the fluorescence decay in the presence of noise may lead to non-physical solutions (non-necessarily monotone decreasing). This is addressed by the adoption of additional constraints, namely that the resulting fluorescence estimation is positive, decaying and convex, thus limiting the results to physically realistic functions [32]. Using this method, for each pullback, fluorescence lifetime and intensity were derived for each of the four channels of the instrument and 25 000 measurement locations.

IVUS images are reconstructed by first extracting the envelope of the RF signal, with log compression, to obtain the A-line scans. 256 A-line scans were then combined into a cross sectional image (B-scan). The processed IVUS data obtained from one pull-back consists of approximately 150 frames.

Bimodal FLIm-IVUS images are reconstructed by registering each FLIm-derived parameter to the right frame and angular position based on time stamp information available for both IVUS and FLIm data. 3D surface rendering was obtained using a segmentation of the IVUS data to recover the geometry of the vessel lumen.

The feasibility of acquiring multimodal data with this FLIm-IVUS system and data processing method was demonstrated *in vivo* in swine model and applied to imaging studies of *ex vivo* human coronary artery samples (Chapter 3).

2.9 High performance free-form optics for iv- FLIm imaging [P2]

During testing of the FLIm-IVUS catheter described in the previous sections, the presence of non-uniform rotational distortion (NURD) was apparent (Figure 11). NURD is an imaging artifact caused by variations of the rotation speed of the distal end of the device, in turn leading to non-uniform angular sampling. It is a common occurrence in intravascular imaging devices if the torsional stiffness of the imaging core (provided by the torque coil) is low or the frictions between imaging core and sheath are high, leading to a stick and release cyclical oscillation of the imaging core.
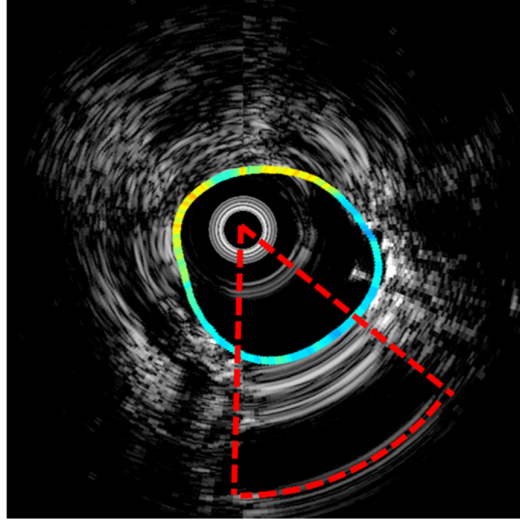
Figure 11: illustration of non-uniform rotational distribution (NURD). Asymmetric friction leads to a non-uniform rotation that leads to uneven angular sampling. Repeat measurements at similar angles are visible in the sector highlighted in red.

The friction between the core and sheath is influenced by the bending radius of the catheter, the torsional stiffness of the torque coil and the bending stiffness of the imaging core. The bending radius is dependent on the path of the catheter, itself constrained by anatomical characteristics of the aorta and coronary vessels. The design of the torque coil consists of two counter-wound layers optimized to provide high torsional stiffness and low bending stiffness so only minimal improvements can be expected by refining the torque coil design. The main NURD contributor identified in the FLIm-IVUS catheter design is the bending stiffness of the multimode fiber. The dimensions of the core (200 μm) were chosen to maximize signal collection efficiency but lead to a much higher bending stiffness than typical single mode fibers used for intravascular OCT, for example. The bending stiffness of a fiber is proportional to its area moment of inertia:

$$I_x = \frac{\pi.d^4}{64}$$
                                                            Eq. 1

The multimode fiber used here, with a 220 µm cladding diameter, presents therefore an ~860% increase in bending stiffness compared to a 125 µm cladding diameter single mode fiber.

Reducing the multimode fiber diameter would address the NURD issue, at the expense of collection efficiency, proportional to the square of the fiber diameter. The reduction of fiber cross section could be compensated by the adoption of a distal end focusing optics to increase collection efficiency, but the miniature optics currently used for intravascular optical devices such as OCT – gradient index (GRIN) lens or fused ball lens designs - are not suitable for intravascular FLIm (Figure 12).
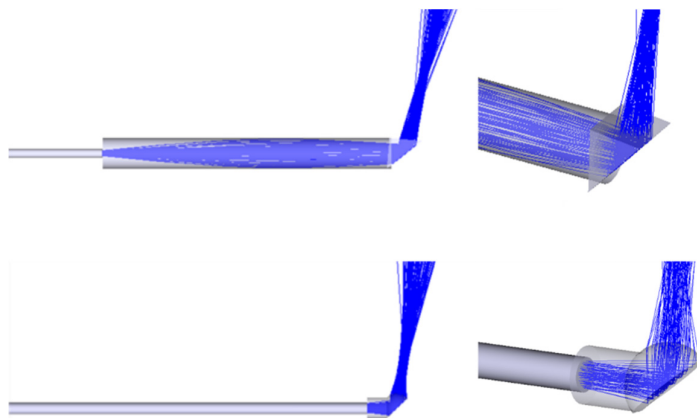
Figure 12: Illustration of side-viewing intravascular imaging probes distal end optics used in combination with a 100 µm core fiber. Top: 0.2 NA lithium doped GRIN lens. The low NA of the lens leads to a >5 mm element, not suitable for use in a high flexibility catheter. Bottom: ball lens. Beam expansion requires the splicing of dissimilar fiber diameters. Use of the ball lens in liquids requires the addition of a short length of tubing to cap the lens. This increases bulk, complexity and introduces astigmatism.

GRIN based side viewing optics for intravascular application typically rely on silver doped GRIN element, available with numerical apertures (NA) of up to 0.5. In that case, the optics typically consist of the fiber, assembled with a glass rod where the optical beam is expending, followed by a short length of GRIN optic used as a micro-lens to focus the light at a sufficient working distance, and a prism to reflect the light in a radial direction [33]. Unfortunately, silver doped GRIN

elements present strong absorption and autofluorescence at 355 nm and cannot be used for our application [34]. An alternative dopant, lithium, presents optical properties suitable for use with UV light, at the cost of a reduced NA (~0.2). Focusing the light from a 0.22 NA multimode fiber means that some of the light coupled to the fiber's highest modes cannot be guided by the optic. But more importantly, the limited NA leads to a much longer element for an identical pitch (Length of 0.25 pitch lens: 3.05mm (0.2 NA) vs. 1.15 mm (0.5 NA)). The optical assembly that provides a working distance of ~1.5mm, typical for intravascular devices, would have a length of more than 5 mm (see figure 12). Reducing the rigid length of the imaging core is a key factor to enable navigation in tortuous anatomy such as the coronary vasculature, so this UV compatible GRIN optics is not suitable.

A second approach is to use a polished fused ball lens to provide reflection via total internal reflection of the polished face and focusing by the spherical surface of the ball. Such fibers are manufactured routinely for OCT applications by splicing a short length of no core fiber at the end of the single mode fiber, and fusing the distal end of no core fiber into a sphere, polished at an angle in a final step [33]. For use in combination with multimode fibers, it is necessary that the no core fiber diameter is larger than the multimode fiber to allow for unconstrained beam expansion. Splicing of dissimilar fiber sizes is in itself a challenging process. The design optimization is also heavily constrained as selection of the probe's working distance is determined by the ability to form a sphere of the right curvature. Finally, a FLIm-IVUS application requires the imaging core to be submerged in liquids. Because the design relies on index mismatch for total internal reflection as well as focusing, it is necessary to enclose the optic into a glass capillary, further increasing bulk and complexity.

A novel design or side viewing fiber optic was developed to address these limitations [P2]. It consists of a short length of pure fused silica, terminated with a curved, reflective coated surface that performs radial redirection of the beam as well as focusing (Figure 13). When using a broadband reflective coating, the design is suitable for UV-Visible-IR operation with negligible chromatic aberrations as

light only travels in pure silica and reflection off the curved surface is not dependent on wavelength. It is suitable for operation in air as well as immersed in liquid without any additional steps and enables correction of astigmatism introduced by a catheter sheath. Further description of the manufacturing process and evaluation of optical performance is described in [P2]
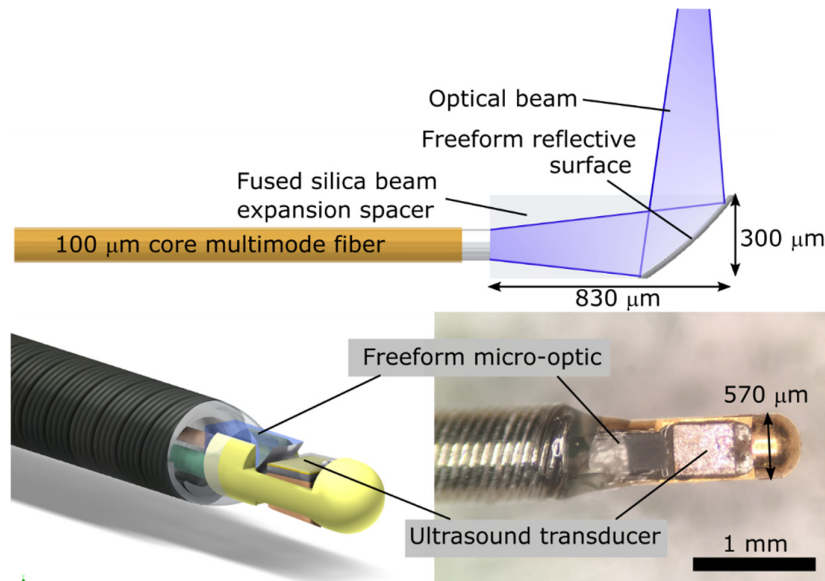
Figure 13: Schematic of freeform reflective micro-optics (top). Computer representation of micro-optic integrated in the distal housing of an improved FLIm-IVUS imaging core (bottom left). Close up of a fabricated imaging core (bottom right). The torque coil is carried over from the previous generation of imaging core and could be replaced with a reduced dimensions coil to bring the dimensions of the imaging section to ~3.1 Fr.

2.10 FLIm-Raman imaging as a validation tool

Raman spectroscopy relies on precise measurement of inelastically scattered light (Stokes and anti-Stokes scattering) from samples. Because inelastic scattering is determined by vibrational states of molecular bonds, the presence of specific bonds can be identified from the spectral shift observed in the collected light. Raman spectroscopy can be implemented using a variety of source wavelength; therefore, spectral shifts are typically expressed in wavenumber, a quantity independent from the excitation wavelength, according to Eq. 2:

$$Raman\ shift\ [cm^{-1}] = \frac{10^7}{\lambda_{ex}[nm]} - \frac{10^7}{\lambda[nm]}$$
<div align="right">Eq.2</div>

Raman instrumentation is conceptually simple, as it consists of a monochromatic light source, combined with a filter used for rejection of elastically scattered light and a wavelength dispersion mechanism. In practice, accurate measurements necessitate a narrow emission light source with stable center frequency, and effective blocking of the excitation light using steep dielectric filters. High signal to noise ratio/ high spectral resolution measurements are achieved by using high quality dispersion elements such as transmission gratings, combined with low noise photodetectors, typically cooled charge coupled devices (CCD).

Raman is a point measurement technique often used in analytical chemistry to identify compounds or characterize and monitor processes. For heterogeneous samples, additional information is provided by mapping the spectroscopic signature for a series or locations. This approach is very valuable for the study of biological systems, typically at the microscopic level leading to interrogated volumes of a few cubic micrometers. For mapping of larger samples, the use of lower lateral resolution fiber optic probes scanned over the sample are an alternative to tiling of microscopy images, and lead to faster data acquisition for a given area at the cost of a reduced lateral resolution.

These fiber optic probes typically consist of bifurcated probes with a fiber for delivery of excitation light, multiple fibers for signal collection, and may include distal end optics to improve signal collection and lateral resolution. Filters are integrated at the distal end of the probe, in direct correspondence to the excitation and collection fibers, to block Raman signal generated in the delivery fiber, and block excitation light propagation into the collection fibers, respectively.

This arrangement is amenable to multimodal imaging, because it is straightforward to replace one of the collection fibers with a fiber dedicated to an additional optical modality, with minimal impact on Raman signal collection performance. Such fiber optic probe is used for the integration of FLIm with Raman

spectroscopy as reported in [P3]. It is derived from a probe previously reported [18], and used for combined FLIm-Raman imaging of an ex vivo human sample [35]. This trifurcated probe consists of a central FLIm excitation/ collection fiber without any filter element (first leg of the probe), connected to the FLIm instrumentation described in section 2.3. One of the peripheral fibers, in combination with a low pass filter, is connected to the Raman light source (second leg of the probe). 7 peripheral fibers, in combination with a long pass filter, are used for Raman collection and connected to the spectrometer (third leg). The last peripheral fiber, unfiltered, can be used for bifurcated fluorescence imaging and is typically not used.

The probe can be used as a point measurement device or mounted on a raster scanning stage to generate bimodal spectroscopic images. Among the advantages of the combination of these two spectroscopic images, we can list the ability to quickly scan large areas by leveraging the high point measurement speed (100-1000 points/second), to identify areas where higher specificity measurements enabled by Raman spectroscopy, can be directed. Another potential use is performing comparative imaging, where samples are being imaged using both FLIm and Raman techniques, such that relationships between information provided by each modalities can be systematically investigated. This is the subject of [P3].

3. Towards in vivo characterization of atherosclerotic lesions

The FLIm-IVUS catheter system presented above is designed to be suitable for imaging of coronary arteries. The physical characteristics of this bimodal catheter are close to other comparable intravascular imaging devices and the 5 s imaging sequence is compatible with blood clearing using a bolus injection of flushing solution. The ability of the FLIm-IVUS system to acquire co registered images in realistic conditions was evaluated in swine. The system was then used to perform imaging studies on ex vivo human samples to further investigate how FLIm

information can supplement morphological information from IVUS to better characterize atherosclerotic lesions [P1].

3.1   In vivo validation of intravascular FLIm-IVUS

A key factor to optimize *in vivo* data acquisition is the determination of flushing parameters. In clinical practice, flushing for OCT imaging is performed using iodinated contrast. Iodinated contrast is transparent in the visible-IR range, presents adequate viscosity and osmolarity properties, and is already in use in catheterization procedures because it is the standard-of-care contrast agent for angiography. Unfortunately, we observed strong absorption at wavelengths below 400 nm (Figure 14).
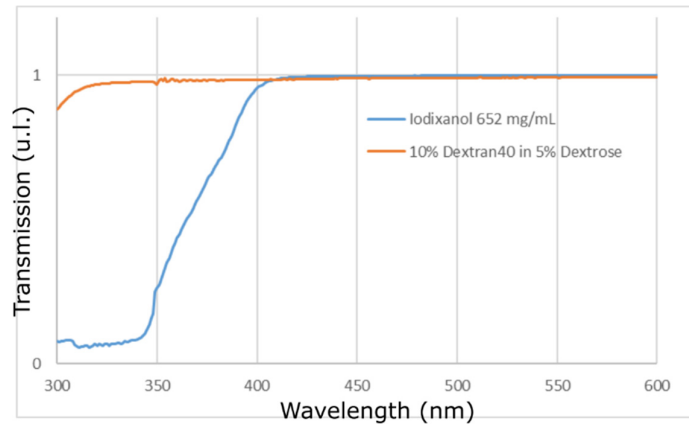
Figure 14: Transmission spectra of 1mm thick samples of iodinated contrast (Visipaque 320, corresponding to 652 mg/mL Iodixanol) and 10% Dextran40 solution. Both solutions present outstanding transparency in the visible region (>400 nm) but strong absorption of iodinated contrast in the near UV prevent its use for FLIm imaging.

Dextran solution used in some clinical settings as an alternative flushing agent presents excellent transparency and suitable viscosity and osmolarity properties (Table 2). Two different Dextran solutions were tested: a combination with sodium chloride alone, and a combination of dextrose and sodium chloride. Better stability of the electrocardiogram was observed for the Dextran/ dextrose/ NaCl solution. This is consistent with other publications evaluating different flushing agents [36]; this solution was therefore chosen for our experiments.

	Blood	Visipaque 320 (Iodinated contrast)	0.9% NaCl (saline)	10% Dextran 40, 0.9% NaCl	10% Dextran 40, 5% dextrose, 0.14% NaCl
Transmission at 355 nm (1mm path)	NA	35%	98%	>97%	>97%
Viscosity (cP)	3-4	11.8	0.69	~4	~4
Osmolarity (mOsmol/kg water)	280-300	290	308	310	310
Comments		Preferred OCT flushing solution	• Requires high flow (>10 mL/s) • T-wave drop • Hypotension	• Good flushing performances • T-wave drop • Hypotension	• Good flushing performances • No noticeable EKG changes

Table 2: Characteristics of different flushing agents used for optical coronary artery imaging.

Tests were performed using an automated injection system (Medrad Advanta, Warrendale, PA) to provide more consistency and flexibility in determining injection rates and duration. A 7Fr guide was inserted in the left main coronary stem. The FLIm-IVUS device was inserted in the mid LAD. Repeat 20 mm bimodal imaging pullbacks were performed. Displacement of blood could be tracked using IVUS because speckles due to blood scattering subside when the flushing solution reaches the imaging plane of the device, typically 3 s after the start of the injection. The injection was maintained for another 5 s, corresponding to the end of the pullback sequence. We observed that injection rates of 3 mL/s or more were necessary to perform efficient flushing. No clear improvement was observed by increasing the flushing rate past 4 mL/s. It can be noted that the quality of the flush is strongly dependent on the proper insertion of the guide catheter into the left stem. High flushing flows (>5 mL/s) have led to occasional unseating of the guide catheter from the artery ostium and is not recommended.

These imaging tests were performed in healthy swine (~75 kg, ~5 months) that presented healthy vessels. No contrast was therefore expected in the FLIm images, and the ability to acquire robust data *in vivo* was assessed by the mean and standard deviations of the recovered lifetime for various fluorescence signal intensities (Figure 15).
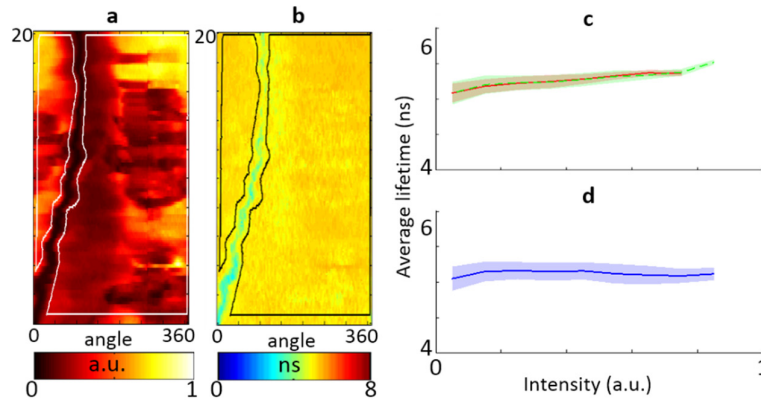
Figure 15: En-face FLIm images of healthy arteries. Fluorescence intensity (a) and lifetime (b) en face images were segmented to remove the guide wire. Lifetime values and standard deviation in function of signal intensity, for repeat acquisitions at the same location (c) and averaged over 5 different locations (d). Minimal variations of lifetime values across the field of view, despite large variations in intensity, demonstrate that FLIm data can be collected in conditions representative of clinical use. Adapted from [P1] CC 4.0

An illustration of the ability of FLIm to detect features based on fluorescence lifetime and spectral information was demonstrated by imaging a stent with fluorescence targets deployed in the LAD [P2].

3.2   Imaging study of ex vivo human coronary samples using a FLIm-IVUS catheter

Intravascular imaging devices are invasive devices that present significant risks and therefore regulatory requirements for testing in human subjects are stringent. Additionally, studies in human subject are complex because unlike imaging studies in oncology, for example, no samples are available for further analysis to confirm findings from imaging, and clinical validations typically consist of outcome studies, where the location of culprit lesions in future acute coronary events is compared with earlier imaging data.

For these reasons, a first important step consists in the evaluation of intravascular imaging devices on *ex vivo* human samples. As outlined in section 1.2, the entire adult population is affected by some level of atherosclerosis, so most *ex vivo* coronary specimens are likely to present lesions that can be used for an initial assessment of the ability of the device to identify optical signature relevant to

plaque pathophysiological characteristics. For this study, samples were obtained from the University of Pennsylvania heart transplant program in compliance with the University of Pennsylvania and University of California, Davis institutional review boards, either from heart transplant patients or organ donors.

Coronary artery segments were harvested from hearts, chilled in isopentane, frozen in liquid nitrogen and sent to our laboratory. Before imaging, samples were thawed, mounted in custom holders and immersed in a 37 ºC phosphate buffered saline bath. A circulation system was used to flush the artery during imaging to prevent vessel collapse. After imaging, the artery and holder were submerged in formalin solution; the solution was circulated inside of the sample to maintain lumen shape during the fixation process and facilitate future co-registration.
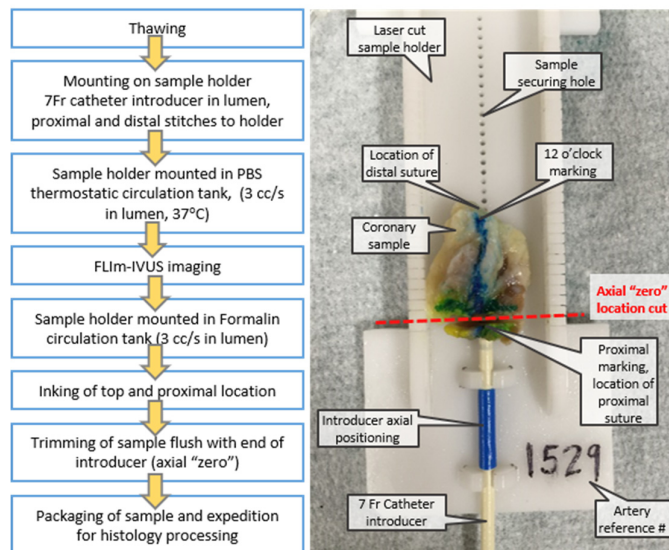
Figure 16. Workflow of sample preparation and imaging. Fluid circulation in artery lumen during imaging and fixation prevents lumen collapse and improves registration accuracy. Proximal and distal suturing of sample on holder limit axial shrinking during fixation.

FLIm-IVUS data was processed using the method described in section 2.8. Histology sections were first coarsely registered with imaging frames based on axial location and angular alignment from sample inking.
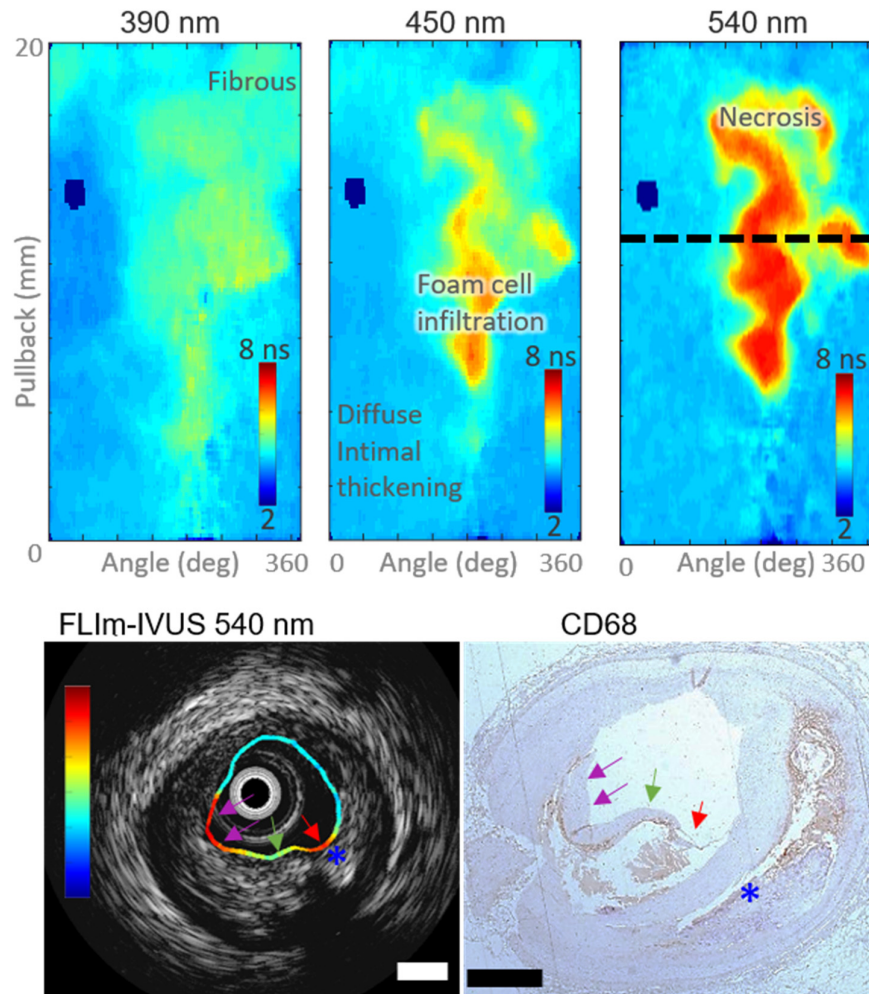
Figure 17: FLIm-histology comparison. Fibrous tissue and fibrous caps can be distinguished by increased lifetimes at 390 and 450 nm. Diffuse intimal thickening has shorter lifetimes than all other components in all wavelength ranges. Foam cell infiltration causes increased lifetimes at both 450 nm and 540 nm, as does necrosis. The dashed line indicates the location of the FLIm-IVUS cross-section and CD68 image. This region includes a fibrous cap infiltrated with foam cells (purple arrowheads), fibrous cap (green arrowhead), and a thin fibrous cap overlying necrotic core (red arrowhead). The penetration depth of FLIm is ~150 um, thus we FLIm does not see the deeper necrotic calcified core, but it is visible with IVUS (blue asterisk). Scale bar = 1 mm.

Fine registration was performed by identifying landmarks in IVUS and histology. The presence of eccentric lumen, branches, and calcifications provides a variety of landmarks that facilitates the histology registration process. FLIm information is

withheld during the fine registration step to prevent biasing of the results that could arise from providing both histology and FLIm during the registration process.

Systematic assessment of FLIm signature in comparison with various histological features on 30+ artery samples is still ongoing, but early results have shown some clear associations between FLIm parameters and presence of early stage plaque (390 nm channel), and mFC infiltration (540 nm channel).

3.3   FLIm- Raman spectroscopy comparative imaging study [P3]

Sources of FLIm contrast are not easily identified based on histological findings alone. mFC infiltration could be easily linked with increase in 540 nm lifetime but the source of 390 nm lifetime could not be univocally associated with any specific histological finding. 390 nm FLIm contrast is clearly linked with plaque boundaries, but not all plaques present the same increase in 390 nm lifetime. Measurement of pure compounds to allow for identification of possible species responsible for the observed lifetime increase presents limitations. For a start, several species (collagen, elastin, some lipids) present a peak fluorescence emission at shorter wavelengths [37]. Additionally, fluorescence decay properties of molecules are modulated by their microenvironment, such that measurement of pure compounds may not accurately reflect their emission properties in tissue [38]. Here, we decided to leverage the ability of Raman spectroscopy to provide a detailed signature of tissue composition to identify possible sources of FLIm contrast. More specifically, Raman spectral features, corresponding to the presence of specific molecular bonds, are routinely used to identify molecular species with high specificity [39].

For this work, the combined FLIm/Raman instrumentation described in 2.10 was used to image human coronary artery samples. Raman data acquisition is inherently slower than fluorescence due to the lower efficiency of the Raman process. For this study, extended exposure times (10s) for each location were used

to maximize signal SNR. The speed limitation made imaging of the whole sample surface with Raman impractical, therefore imaging was performed sequentially. At first, the entire surface was scanned with FLIm (~1-2 min depending on sample size). Select regions of interest were then defined to include transition regions between low lifetime regions (healthy) and increased lifetime regions to perform Raman data acquisition. When possible, regions presenting lifetime increase in only one channel were selected, to facilitate the identification of compounds related to lifetime increases in a single FLIm spectral band.

Raman data was processed (wavenumber calibration, baseline correction, normalization) to obtain spectra for each location. The comparison with FLIm data was performed via a multivariate linear regression approach, to identify which Raman feature is most related to variations in fluorescence lifetime. A first approach would be to develop a linear model that predicts FLIm values based on Raman spectra. Directly using the Raman intensities as independent variables of the regression presents issues. Indeed, when an independent variable is highly correlated with a combination of one or more other independent variables, the contribution of that independent variable is influenced by other independent variables. This multicollinearity issue leads to unreliable estimations of the regression coefficients. This is clearly the case with Raman spectra, where neighboring wavenumbers are highly correlated. An option is to perform a PCA and use the loadings as independent variables. This addresses the multicollinearity issue but regression coefficients become hard to interpret as they present features for multiple wavenumbers at once. An alternative is to consider the FLIm parameters as the independent variables, and use a linear regression model to predict Raman intensities, followed by a computation of the coefficient of determination for each wavenumber to see if significant amount of the Raman data variance can be explained by the FLIm model.

The main finding of the study was that lower wavelength (<400 nm) FLIm contrast was linked with LDL accumulation, characterized by Raman as a combination of cholesterol and ß-Carotene [40,41]. This finding is interesting because it suggests that conclusions from previous imaging studies that associated lifetime contrast in

that wavelength band with varying amounts of collagen based on histological finding, needs revisiting [28,42].

Imaging validation studies on the basis of comparative imaging present challenges, due for example to the difference in penetration depths or the need to create hybrid instrumentation with possible degradations of the performances of each single imaging modality. Nevertheless, imaging based validations also present strong benefits. Indeed, a critical bottleneck of histology based validation of imaging techniques is the need for extensive human intervention for sample processing (grossing, fixation, sectioning, staining), histology interpretation (extraction of relevant histological features), and registration with imaging data. Here, the availability of a co-registered imaging dataset means that after definition of the data processing methods, minimal human intervention is required. It becomes therefore possible to greatly increase the number of samples of a study with minimal additional workload beyond the initial data acquisition step.

4. Summary

Cardiovascular diseases are one of the leading causes of deaths and atherosclerosis is the main culprit. This condition is characterized by the build-up of plaque in the arteries throughout the life of individuals that creates narrowing that can impede blood flow, but also cause heart attacks or strokes when these plaques release thrombogenic material in the bloodstream. Because of its clinical relevance, medical research of atherosclerosis is a very active field. Decades of research efforts have led to improved understanding of the disease mechanisms, but a full understanding of atherosclerosis pathophysiology is still elusive. Imaging of lesions with non-invasive modalities is challenging, because a suitable modality would require high spatial resolution to image millimeter sized lesions, high temporal resolution to deal with large motion of the beating heart, and molecular sensitivity to provide information regarding the physiological processes at play. Therefore, most observations in human are originating from artery studies that provide a snapshot of lesions but do not enable to follow the development over time. Animal models have been developed to facilitate research on atherosclerosis, but replicating the decades-long lesion development process in time scales suitable for medical research is challenging. Alternatively, in vitro studies based on cellular models of atherosclerosis have been developed, but fail to capture some of the effects thought to be critical for lesion development, such as hemodynamics.

An imaging device able to fully characterize lesions *in vivo* in patient and enable repeat snapshots that capture lesion development would be a great asset for researchers and clinicians alike. Unfortunately, no such instrument is currently available. In the pursuit of the perfect intravascular imaging device, imaging research is split between improvements in imaging techniques currently available in clinical settings such as intravascular ultrasound (IVUS), or intravascular optical coherence tomography, and development of catheter-based implementations of a variety of biomedical imaging techniques, such as fluorescence, photoacoustic, Raman spectroscopy, or near-infrared spectroscopy.

Fluorescence lifetime imaging (FLIm), widely used as a label free microscopy imaging technique, provides a biochemical signature of tissue based on

autofluorescence properties. Here, we developed an integrated FLIm-IVUS imaging catheter system, derived from a clinical IVUS system, suitable for the interrogation of coronary arteries *in vivo*. This system maintains the benefits of the clinical system, such as real time IVUS image display, useful for selections of areas of interest, and a form factor suitable for use in clinical setting. In addition, it is able to perform acquisitions of co-registered FLIm and IVUS data at high speed. High FLIm data acquisition speeds of up to 20000 fluorescence decay measurements over four different spectral channels are performed in five seconds. This speed is made possible by a pulse sampling acquisition scheme with temporal multiplexing of the different spectral bands, developed by our group. Dedicated low profile (3.7 Fr), flexible, FLIm-IVUS catheters were designed, fabricated and tested. The motor drive unit from the clinical system was redesigned to integrate an optical channel without adversely affecting IVUS performance [P1].

The ability of this instrument to acquire robust FLIm data in vivo was evaluated in swine model. Data acquisition procedure parameters (flushing fluid, flow rate) were optimized to demonstrate that the FLIm-IVUS system proposed here is suitable for data acquisition in conditions representative of percutaneous interventions in human patients.

Imaging of ex vivo human samples using the catheter system confirmed the benefit of a bimodal system. IVUS capability provides accurate morphological information that facilitates accurate registration with histology sections for FLIm imaging validation. We could also demonstrate that based on FLIm contrast, locations of macrophage foam cells accumulations could be identified from the 540 nm instrument channel. Strong contrast was also observed in the 390 nm spectral band of the instrument. This contrast may be related to the presence of extracellular lipids and could provide additional information about early stages of lesion development.

Further optimization of optical and mechanical performance of the catheter was achieved with the development of a monolithic freeform reflective optics. This novel type of side viewing optic was developed to address limitations of currently available side viewing optics (gradient index or angled polished ball lenses) that

make them unsuitable for intravascular FLIm. The freeform optics demonstrates improved optical performances in compact, fluorescence background free, monolithic element, and is suitable for use in liquids without the need of an additional cap. In comparison to the first version of the bimodal instrument that relies on a 200 µm core fiber for FLIm excitation delivery and signal collection, the adoption of the distal end optic enables the use of a 100 µm core fiber optic with minimal degradation of collection efficiency. This new implementation presents increased flexibility (16x reduction in fiber bending stiffness) and enables improvements lateral resolution [P2].

Finally, a pilot comparative imaging study of ex vivo human artery samples was performed combining the pulse sampling FLIm data acquisition technique with Raman spectroscopy, by means of a bimodal forward-viewing optical probe. Methods based on multiple regression techniques were developed for the automated analysis of FLIm contrast sources using Raman spectroscopy data. Results from this pilot study confirmed the link between fluorescence emission above 500 nm and presence of superficial macrophage foam cells, whereas increase in lifetime below 400 nm was associated with the presence of carotenoids and low density lipoproteins. The approach described here is well suited to the study of a large number of samples as, unlike traditional imaging validation based on histology, this comparative imaging approach does not require human intervention for sample processing, section registration and extraction of histological features [P3].

Development of dedicated intravascular instrumentation combined with further understanding of the information provided by FLIm by means of histological studies as well as comparative imaging will improve the relevance of FLIm as a practical tool for the investigation of atherosclerosis. Future work will focus on regulatory activities to enable studies in human subject, where the ability of FLIm to provide the biochemical signature of lesions *in vivo* may be leveraged to improve understanding of the disease natural history, develop new drugs, and possibly be used in clinical settings to improve patient treatment.

5. Zusammenfassung

Herz-Kreislauf-Erkrankungen sind eine der häufigsten Todesursachen, und Arteriosklerose ist der Hauptverursacher. Dieser Zustand ist durch die Ansammlung von Plaques in den Arterien verursacht, welche sich im Laufe des Lebens bei einer Parson ansammeln können. Diese Plaques können eine Verengung hervorruft, welche den Blutfluss behindern, aber auch Herzinfarkte oder Schlaganfälle verursachen kann, wenn dieses thrombogenes Material in den Blutkreislauf abgeben. Aufgrund ihrer klinischen Relevanz ist die medizinische Erforschung der Atherosklerose hoch aktuell. Zwar haben jahrzehntelange Forschungsanstrengungen zu einem besseren Verständnis der Krankheitsmechanismen geführt, ein lückenloses Verständnis der Pathophysiologie der Atherosklerose, ist jedoch noch nicht gegeben. Zum Beispiel ist die Abbildung von Läsionen mit nicht-invasiven Modalitäten bis heute eine Herausforderung, da die geeignete Modalität nicht nur eine hohe räumliche Auflösung zur Abbildung von Läsionen in Millimetergröße und eine hohe zeitliche Auflösung zur Bewältigung großer Bewegungen des schlagenden Herzens ermöglichen muss, sondern auch eine molekulare Empfindlichkeit erfordert, um Informationen über physiologische Prozesse zu bestimmen. Durch diese komplexen Anforderungen stellen die meisten durchgeführten Arterienuntersuchungen beim Menschen, eine Momentaufnahme der Läsionen da, und bieten jedoch keine Möglichkeit, die Entwicklung zeitlich zu verfolgen. Es wurden Tiermodelle entwickelt, um die Erforschung von Arteriosklerose zu erleichtern, aber die Nachbildung des jahrzehntelangen Entwicklungsprozesses von Läsionen in für die medizinische Forschung geeigneten Zeiträumen bleibt eine Herausforderung. Alternativ wurden in-vitro Studien entwickelt, die auf zellulären Atherosklerose-Modellen basieren, jedoch einige der Effekte, die für die Entwicklung von Läsionen als kritisch angesehen werden, wie z. B. die Hämodynamik, nicht erfassen.

Ein bildgebendes Gerät, das in der Lage ist, Läsionen in vivo bei Patienten vollständig zu charakterisieren und wiederholte Schnappschüsse zu ermöglichen,

die die Entwicklung von Läsionen erfassen, wäre für Forscher und Kliniker gleichermaßen von großem Nutzen. Leider ist derzeit kein solches Instrument verfügbar. Bei der Suche nach dem perfekten Gerät für die intravaskuläre Bildgebung wird die bildgebende Forschung aufgeteilt in Verbesserungen der Bildgebungstechniken, die derzeit in klinischen Umgebungen wie der intravaskulären Ultraschalltomographie (IVUS) oder der intravaskulären optischen Kohärenztomographie verfügbar sind, und in die Entwicklung katheterbasierter Implementierungen einer Vielzahl biomedizinischer Bildgebungsverfahren wie Fluoreszenz, Photoakustik, Raman-Spektroskopie oder Nahinfrarot-Spektroskopie.

Die Fluoreszenzlebensdauer-Bildgebung (FLIm), die häufig als markierungsfreie mikroskopische Bildgebungstechnik verwendet wird, liefert eine biochemische Signatur von Gewebe auf der Grundlage der Autofluoreszenzeigenschaften. Im Rahmen der Promotion wurde ein integriertes FLIm-IVUS-Bildgebungskathetersystem entwickelt, das von einem klinischen IVUS-System abgeleitet wurde und für die Abfrage von Koronararterien in vivo geeignet ist. Dieses System behält die Vorteile des klinischen Systems, wie die Echtzeit-IVUS-Bilddarstellung bei, die für die Auswahl von Bereichen von Interesse nützlich ist und einen Formfaktor, der für die Verwendung in der klinischen Umgebung geeignet ist. Darüber hinaus können mit ihm gemeinsam registrierte FLIm- und IVUS-Daten mit hoher Geschwindigkeit erfasst werden. Hohe FLIm-Datenerfassungsgeschwindigkeiten von bis zu 20000 Fluoreszenzabklingmessungen über vier verschiedene Spektralkanäle können in fünf Sekunden durchgeführt werden. Diese Geschwindigkeit wird durch ein von unserer Gruppe entwickeltes Impulsabtastungserfassungsschema mit zeitlichem Multiplexen der verschiedenen Spektralbänder ermöglicht. Im Rahmen der Arbeit wurden spezielle flexible FLIm-IVUS-Katheter mit einem kleinen Durchmesser (3,7 Fr) entworfen, hergestellt und getestet. Weiterhin wurde die Motorantriebseinheit aus dem klinischen System so umgestaltet, dass sie einen optischen Kanal integriert, ohne die IVUS-Bildgebung nachteilig zu beeinflussen [P1].

Die Fähigkeit dieses Instruments, robuste FLIm-Daten in vivo zu erfassen, wurde im Schweinemodell demonstriert. Die Parameter des Datenerfassungsverfahrens (Spülflüssigkeit, Durchflussrate) wurden optimiert, um zu zeigen, dass das hier vorgeschlagene FLIm-IVUS-System für die Datenerfassung unter Bedingungen geeignet ist, die für perkutane Eingriffe bei menschlichen Patienten repräsentativ sind.

Die Abbildung von ex-vivo Humanproben unter Verwendung des Kathetersystems bestätigte den Nutzen eines bimodalen Systems. Die IVUS-Funktion bietet genaue morphologische Informationen, die eine präzise Registrierung mit histologischen Schnitten für die FLIm-Bildgebungsvalidierung ermöglichen. Wir konnten auch zeigen, dass auf der Grundlage des FLIm-Kontrasts Positionen von Makrophagen-Schaumzell-Ansammlungen aus dem Instrumentenkanal von 540 nm identifiziert werden konnten. Ein starker Kontrast wurde auch im 390-nm-Spektralbereich beobachtet. Dieser Kontrast kann mit dem Vorhandensein extrazellulärer Lipide zusammenhängen und zusätzliche Informationen über frühe Stadien der Läsionsentwicklung liefern.

Eine weitere Optimierung der optischen und mechanischen Leistung des Katheters wurde mit der Entwicklung einer monolithischen Freiform-Reflexionsoptik erreicht. Diese neuartige Seitenblickoptik wurde entwickelt, um Einschränkungen der derzeit verfügbaren Seitenblickoptik (Gradientenindex oder abgewinkelte polierte Kugellinsen), die sie für intravaskuläres FLIm ungeeignet machen, zu beseitigen. Die Freiformoptik zeigt verbesserte optische Eigenschaften bei kompakten, fluoreszenzhintergrundfreien, monolithischen Elementen und eignet sich zur Verwendung in Flüssigkeiten, ohne dass eine zusätzliche Kappe erforderlich ist. Im Vergleich zur ersten Version des bimodalen Instruments, das für die FLIm-Anregung und die Signalerfassung auf einer 200-µm-Kernfaser beruht, ermöglicht die Verwendung der distalen Endoptik die Verwendung einer 100-µm-Kernfaser mit minimaler Verschlechterung der Detektionseffizienz. Diese neue Implementierung bietet eine erhöhte Flexibilität (16-fache Reduzierung der

Faserbiegesteifigkeit) und ermöglicht gleichzeitig eine Verbesserung der lateralen Auflösung [P2].

Schließlich wurde eine Pilotstudie zur vergleichenden Bildgebung von ex-vivo-Proben menschlicher Arterien durchgeführt, bei der die FLIm-Datenerfassungs mit der Raman-Spektroskopie mittels einer bimodalen optischen Vorwärtssichtsonde kombiniert wurde. Für die automatisierte Analyse von Daten aus der FLIm und Raman-Spektroskopie wurden Methoden basierend auf multiplen Regressionstechniken entwickelt. Die Ergebnisse dieser Pilotstudie bestätigten den Zusammenhang zwischen der Fluoreszenzemission über 500 nm und dem Vorhandensein oberflächlicher Makrophagenschaumzellen, wohingegen die Erhöhung der Lebensdauer unter 400 nm mit dem Vorhandensein hervorgehobener Lebensdauerverlängerungen bei Carotinoiden und Lipoproteinen niedriger Dichte (LDL) verbunden war. Der hier beschriebene Ansatz eignet sich gut für die Untersuchung einer großen Anzahl von Proben, da im Gegensatz zur herkömmlichen Bildgebungsvalidierung auf der Grundlage der Histologie für diesen Ansatz der vergleichenden Bildgebung keine Eingriffe des Menschen zur Probenverarbeitung, Schnittregistrierung und Extraktion von histologischen Merkmalen erforderlich sind [P3].

Die Entwicklung dedizierter intravaskulärer Instrumente in Kombination mit einem besseren Verständnis der von FLIm bereitgestellten Informationen mittels histologischer Studien, sowie einer vergleichenden Bildgebung, wird die Relevanz von FLIm als praktisches Instrument für die Untersuchung von Arteriosklerose erhöhen. Zukünftige Arbeiten werden sich auf regulatorische Aktivitäten konzentrieren, um Studien direkt am Menschen zu ermöglichen. Dies wird es ermöglichen das Potential von FLIm, d.h. die markerfreie Erfassung von biochemische Signatur von Läsionen in vivo, besser zu nutzten und so ein besseres Verständnis über den Krankheitsverlaufs und neue Therapiemöglichkeiten für die Versorgung von Patienten zu gewährleisten.

Bibliography

1. "CDC, NCHS. Underlying Cause of Death 1999-2013 on CDC WONDER Online Database, released 2015," (2015).
2. W. Insull Jr., "The Pathology of Atherosclerosis: Plaque Development and Plaque Responses to Medical Treatment," Am. J. Med. **122**, S3–S14 (2009).
3. H. C. Stary, A. B. Chandler, S. Glagov, J. R. Guyton, W. Insull, M. E. Rosenfeld, S. A. Schaffer, C. J. Schwartz, W. D. Wagner, and R. W. Wissler, "A definition of initial, fatty streak, and intermediate lesions of atherosclerosis. A report from the Committee on Vascular Lesions of the Council on Arteriosclerosis, American Heart Association.," Circulation **89**, 2462–2478 (1994).
4. Flood Christofer, Gustafsson Maria, Pitas Robert E., Arnaboldi Lorenzo, Walzem Rosemary L., and Borén Jan, "Molecular Mechanism for Changes in Proteoglycan Binding on Compositional Changes of the Core and the Surface of Low-Density Lipoprotein–Containing Human Apolipoprotein B100," Arterioscler. Thromb. Vasc. Biol. **24**, 564–570 (2004).
5. T. M. Doherty, K. Asotra, L. A. Fitzpatrick, J.-H. Qiao, D. J. Wilkin, R. C. Detrano, C. R. Dunstan, P. K. Shah, and T. B. Rajavashisth, "Calcification in atherosclerosis: bone biology and chronic inflammation at the arterial crossroads," Proc. Natl. Acad. Sci. U. S. A. **100**, 11201–11206 (2003).
6. M.-K. Hong, G. S. Mintz, C. W. Lee, B.-K. Lee, T.-H. Yang, Y.-H. Kim, J.-M. Song, K.-H. Han, D.-H. Kang, S.-S. Cheong, J.-K. Song, J.-J. Kim, S.-W. Park, and S.-J. Park, "The Site of Plaque Rupture in Native Coronary Arteries: A Three-Vessel Intravascular Ultrasound Analysis," J. Am. Coll. Cardiol. **46**, 261–265 (2005).
7. B. R. Kwak, M. Bäck, M.-L. Bochaton-Piallat, G. Caligiuri, M. J. A. P. Daemen, P. F. Davies, I. E. Hoefer, P. Holvoet, H. Jo, R. Krams, S. Lehoux, C. Monaco, S. Steffens, R. Virmani, C. Weber, J. J. Wentzel, and P. C. Evans, "Biomechanical factors in atherosclerosis: mechanisms and clinical implications†," Eur. Heart J. **35**, 3013–3020 (2014).
8. J. M. Tarkin, M. R. Dweck, N. R. Evans, R. A. P. Takx, A. J. Brown, A. Tawakol, Z. A. Fayad, and J. H. F. Rudd, "Imaging Atherosclerosis," Circ. Res. **118**, 750 (2016).
9. M. E. Brezinski, G. J. Tearney, N. J. Weissman, S. A. Boppart, B. E. Bouma, M. R. Hee, A. E. Weyman, E. A. Swanson, J. F. Southern, and J. G. Fujimoto, "Assessing atherosclerotic plaque morphology: comparison of optical coherence tomography and high frequency intravascular ultrasound.," Heart **77**, 397 (1997).
10. T. Ma, B. Zhou, T. K. Hsiai, and K. K. Shung, "A Review of Intravascular Ultrasound–Based Multimodal Intravascular Imaging: The Synergistic Approach to Characterizing Vulnerable Plaques," Ultrason. Imaging (2015).
11. S. Brugaletta, H. M. Garcia-Garcia, P. W. Serruys, A. Maehara, V. Farooq, G. S. Mintz, B. de Bruyne, S. P. Marso, S. Verheye, D. Dudek, C. W. Hamm, N. Farhat, F. Schiele, J. McPherson, A. Lerman, P. R. Moreno, B. Wennerblom, M. Fahy, B. Templin, M.-A. Morel, G. A. van Es, and G. W. Stone, "Relationship Between Palpography and Virtual Histology in Patients With Acute Coronary Syndromes," Intracoronary Imaging PROSPECT Study **5**, S19–S27 (2012).

12. T. Ma, M. Yu, J. Li, C. E. Munding, Z. Chen, C. Fei, K. K. Shung, and Q. Zhou, "Multi-frequency intravascular ultrasound (IVUS) imaging," IEEE Trans. Ultrason. Ferroelectr. Freq. Control **62**, 97–107 (2015).

13. R. D. Madder, M. Husaini, A. T. Davis, S. Van Oosterhout, J. Harnek, M. Götberg, and D. Erlinge, "Detection by near-infrared spectroscopy of large lipid cores at culprit sites in patients with non-st-segment elevation myocardial infarction and unstable angina," Catheter. Cardiovasc. Interv. **86**, 1014–1021 (2015).

14. M. Wu, A. Fw van der Steen, E. Regar, and G. van Soest, "Emerging Technology Update Intravascular Photoacoustic Imaging of Vulnerable Atherosclerotic Plaque," Interv. Cardiol. Lond. Engl. **11**, 120–123 (2016).

15. H. Yoo, J. W. Kim, M. Shishkov, E. Namati, T. Morse, R. Shubochkin, J. R. McCarthy, V. Ntziachristos, B. E. Bouma, F. A. Jaffer, and G. J. Tearney, "Intra-arterial catheter for simultaneous microstructural and molecular imaging in vivo," Nat Med **17**, 1680–1684 (2011).

16. Jaffer Farouc A., Vinegoni Claudio, John Michael C., Aikawa Elena, Gold Herman K., Finn Aloke V., Ntziachristos Vasilis, Libby Peter, and Weissleder Ralph, "Real-Time Catheter Molecular Sensing of Inflammation in Proteolytically Active Atherosclerosis," Circulation **118**, 1802–1809 (2008).

17. Keisaku Hamada, Katsumasa Fujita, Nicholas Isaac Smith, Minoru Kobayashi, Yasushi Inouye, and Satoshi Kawata, "Raman microscopy for dynamic molecular imaging of living cells," J. Biomed. Opt. **13**, 1–4 (2008).

18. S. Dochow, D. Ma, I. Latka, T. Bocklitz, B. Hartl, J. Bec, H. Fatakdawala, E. Marple, K. Urmey, S. Wachsmann-Hogiu, M. Schmitt, L. Marcu, and J. Popp, "Combined fiber probe for fluorescence lifetime and Raman spectroscopy," Anal. Bioanal. Chem. **407**, 8291–8301 (2015).

19. M. Jermyn, K. Mok, J. Mercier, J. Desroches, J. Pichette, K. Saint-Arnaud, L. Bernstein, M.-C. Guiot, K. Petrecca, and F. Leblond, "Intraoperative brain cancer detection with Raman spectroscopy in humans," Sci. Transl. Med. **7**, 274ra19 (2015).

20. W. Becker, A. Bergmann, and C. Biskup, "Multispectral fluorescence lifetime imaging by TCSPC," Microsc. Res. Tech. **70**, 403–409 (2007).

21. Y. Sun, R. Liu, D. S. Elson, C. W. Hollars, J. A. Jo, J. Park, Y. Sun, and L. Marcu, "Simultaneous time- and wavelength-resolved fluorescence spectroscopy for near real-time tissue diagnosis," Opt. Lett. **33**, 630–632 (2008).

22. D. R. Yankelevich, D. Ma, J. Liu, Y. Sun, Y. Sun, J. Bec, D. S. Elson, and L. Marcu, "Design and evaluation of a device for fast multispectral time-resolved fluorescence spectroscopy and imaging," Rev. Sci. Instrum. **85**, (2014).

23. R. Cubeddu, D. Comelli, C. D'Andrea, P. Taroni, and G. Valentini, "Time-resolved fluorescence imaging in biology and medicine," J. Phys. Appl. Phys. **35**, R61–R76 (2002).

24. Q. Fang, T. Papaioannou, J. A. Jo, R. Vaitha, K. Shastry, and L. Marcu, "Time-domain laser-induced fluorescence spectroscopy apparatus for clinical diagnostics," Rev. Sci. Instrum. **75**, 151–162 (2004).

25. "Optical Absorption of Hemoglobin," http://omlc.ogi.edu/spectra/hemoglobin/index.html.

26. Y. Ozaki, H. Kitabata, H. Tsujioka, S. Hosokawa, M. Kashiwagi, K. Ishibashi, K. Komukai, T. Tanimoto, Y. Ino, S. Takarada, T. Kubo, K. Kimura, A. Tanaka, K. Hirata, M. Mizukoshi, T. Imanishi, and T. Akasaka, "Comparison of Contrast Media and Low-Molecular-Weight Dextran for Frequency-Domain Optical Coherence Tomography," Circ. J. **76**, 922–927 (2012).

27. D. Ma, J. Bec, D. R. Yankelevich, D. Gorpas, H. Fatakdawala, and L. Marcu, "Rotational multispectral fluorescence lifetime imaging and intravascular ultrasound: bimodal system for intravascular applications," J. Biomed. Opt. **19**, 066004–066004 (2014).

28. H. Fatakdawala, D. Gorpas, J. W. Bishop, J. Bec, D. Ma, J. A. Southard, K. B. Margulies, and L. Marcu, "Fluorescence Lifetime Imaging Combined with Conventional Intravascular Ultrasound for Enhanced Assessment of Atherosclerotic Plaques: an Ex Vivo Study in Human Coronary Arteries," J Cardiovasc. Transl. Res. (2015).

29. J. R. Lakowicz, *Principles of Fluorescence Spectroscopy* (Third edition. New York : Kluwer Academic/Plenum, [2006] ©2006, 2006).

30. J.-M. I. Maarek, L. Marcu, W. J. Snyder, and W. S. Grundfest, "Time-resolved Fluorescence Spectra of Arterial Fluorescent Compounds: Reconstruction with the Laguerre Expansion Technique," Photochem. Photobiol. **71**, 178–187 (2000).

31. P. Van den Hof, B. Wahlberg, P. Heuberger, B. Ninness, J. Bokor, and T. Oliveira e Silva, "Modelling and Identification with Rational Orthogonal Basis Functions," 12th IFAC Symp. Syst. Identif. SYSID 2000 St. Barbara CA USA 21-23 June 2000 **33**, 445–455 (2000).

32. J. Liu, Y. Sun, J. Qi, and L. Marcu, "A novel method for fast and robust estimation of fluorescence decay dynamics using constrained least-squares deconvolution with Laguerre expansion," Phys. Med. Biol. **57**, 843 (2012).

33. M. J. Gora, M. J. Suter, G. J. Tearney, and X. Li, "Endoscopic optical coherence tomography: technologies and clinical applications [Invited]," Biomed. Opt. Express **8**, 2405–2444 (2017).

34. "GRINTECH GmbH Gradient Index Optics," https://www.grintech.de/en/gradient-index-optics/.

35. S. Dochow, H. Fatakdawala, J. E. Phipps, D. Ma, T. Bocklitz, M. Schmitt, J. W. Bishop, K. B. Margulies, L. Marcu, and J. Popp, "Comparing Raman and fluorescence lifetime spectroscopy from human atherosclerotic lesions using a bimodal probe," J. Biophotonics **9**, 958–966 (2016).

36. M. J. Suter, M. Kashiwagi, K. A. Gallagher, S. K. Nadkarni, N. Asanani, A. Tanaka, G. B. Conditt, A. Tellez, K. Milewski, G. L. Kaluza, J. F. Granada, B. E. Bouma, and G. J. Tearney, "Optimizing flushing parameters in intracoronary optical coherence tomography: an in vivo swine study," Int. J. Cardiovasc. Imaging **31**, 1097–1106 (2015).

37. A. C. Croce and G. Bottiroli, "Autofluorescence spectroscopy and imaging: a tool for biomedical research and diagnosis.," Eur. J. Histochem. EJH **58**, 2461 (2014).

38. S. Draxler and M. E. Lippitsch, "Lifetime-Based Sensing: Influence of the Microenvironment," Anal. Chem. **68**, 753–757 (1996).

39. I. ur. Rehman, Zanyar. Movasaghi, and Shazza. Rehman, "Vibrational spectroscopy for tissue analysis," http://www.crcnetbase.com/isbn/9781439836088.

40. A. Lattermann, C. Matthäus, N. Bergner, C. Beleites, B. F. Romeike, C. Krafft, B. R. Brehm, and J. Popp, "Characterization of atherosclerotic plaque depositions by Raman and FTIR imaging," J. Biophotonics **6**, 110–121 (2013).
41. C. Stiebing, L. Schmölz, M. Wallert, C. Matthäus, S. Lorkowski, and J. Popp, "Raman imaging of macrophages incubated with triglyceride-enriched oxLDL visualizes translocation of lipids between endocytic vesicles and lipid droplets," J. Lipid Res. **58**, 876–883 (2017).
42. J. Park, P. Pande, S. Shrestha, F. Clubb, B. E. Applegate, and J. A. Jo, "Biochemical characterization of atherosclerotic plaques by endogenous multispectral fluorescence lifetime imaging microscopy," Atherosclerosis **220**, 394–401 (2012).

Publications

[P1] In vivo label-free structural and biochemical imaging of coronary arteries using an integrated ultrasound and multispectral fluorescence lifetime catheter system (2017)

Reprinted from [1. J. Bec, J. E. Phipps, D. Gorpas, D. Ma, H. Fatakdawala, K. B. Margulies, J. A. Southard, and L. Marcu, 2017. In vivo label-free structural and biochemical imaging of coronary arteries using an integrated ultrasound and multispectral fluorescence lifetime catheter system, Nature Scientific Reports, 7, 8960] in accordance with the Creative Commons license CC BY 4.0

Erklärungen zu den Eigenanteilen des Promovenden sowie der weiteren Doktoranden/Doktorandinnen als Koautoren an der Publikation.

[1]J. Bec, [2]J. E. Phipps, [3]D. Gorpas, [4]D. Ma, [5]H. Fatakdawala, [6]K. B. Margulies, [7]J. A. Southard, and [8]L. Marcu, "In vivo label-free structural and biochemical imaging of coronary arteries using an integrated ultrasound and multispectral fluorescence lifetime catheter system," Scientific Reports 7, 8960 (2017).								
Beteiligt an (Zutreffendes ankreuzen)								
	1	2	3	4	5	6	7	8
Konzeption des Forschungsansatzes	X							X
Planung der Untersuchungen	X						X	X
Datenerhebung	X	X			X		X	
Datenanalyse und Interpretation	X	X	X	X		X		
Schreiben des Manuskripts	X	X						X
Vorschlag Anrechnung Publikationsäquivalent	1.0							

SCIENTIFIC REP♥RTS

OPEN

In vivo label-free structural and biochemical imaging of coronary arteries using an integrated ultrasound and multispectral fluorescence lifetime catheter system

Julien Bec [1], Jennifer E. Phipps[1], Dimitris Gorpas[1,4], Dinglong Ma[1], Hussain Fatakdawala[1,5], Kenneth B. Margulies[2], Jeffrey A. Southard[3] & Laura Marcu[1]

Existing clinical intravascular imaging modalities are not capable of accurate detection of critical plaque pathophysiology in the coronary arteries. This study reports the first intravascular catheter combining intravascular ultrasound (IVUS) with multispectral fluorescence lifetime imaging (FLIm) that enables label-free simultaneous assessment of morphological and biochemical features of coronary vessels *in vivo*. A 3.7 Fr catheter with a fiber-optic channel was constructed based on a 40 MHz clinical IVUS catheter. The ability to safely acquire co-registered FLIm-IVUS data *in vivo* using Dextran40 solution flushing was demonstrated in swine coronary arteries. FLIm parameters from the arterial wall were consistent with the emission of fluorophores present in healthy arterial wall (collagen, elastin). Additionally, structural and biochemical features from atherosclerotic lesions were acquired in *ex vivo* human coronary samples and corroborated with histological findings. Current results show that FLIm parameters linked to the amount of structural proteins (e.g. collagen, elastin) and lipids (e.g. foam cells, extracellular lipids) in the first 200 μm of the intima provide important biochemical information that can supplement IVUS data for a comprehensive assessment of plaques pathophysiology. The unique FLIm-IVUS system evaluated here has the potential to provide a comprehensive insight into atherosclerotic lesion formation, diagnostics and response to therapy.

Myocardial infarction due to plaque rupture is a leading cause of sudden cardiac death[1]. Due to positive remodeling, high plaque burden may occur without significant stenosis, and therefore cannot be reliably identified using conventional angiography. Intravascular ultrasound (IVUS) enables identification of plaque burden due to its high penetration depth (up to 10 mm[2]) but lacks the spatial resolution to identify small scale features such as details of the intima[3], or biochemical changes linked with atherosclerotic lesion formation and evolution. Optical coherence tomography (OCT) provides improved spatial resolution ($<20\,\mu m^2$) that enables highly detailed visualization of fibrous cap and intima morphology as well as some level of detection of macrophages[4] at the cost of penetration depth, thus limiting the ability to assess plaque burden. Direct access to biochemical information could prove valuable for the study of atherosclerotic lesion pathophysiology. Previous studies showed that spectroscopic techniques including near infrared (NIR)[5,6], Raman[7] and fluorescence[8,9] have the potential to provide

[1]Department of Biomedical Engineering, University of California Davis, Davis, 95616, CA, USA. [2]Cardiovascular Institute, Perelman School of Medicine, University of Pennsylvania, Philadelphia, 19104, PA, USA. [3]UC Davis Health System, Division of Cardiovascular Medicine, University of California Davis, Sacramento, 95817, CA, USA. [4]Present address: Institute of Biological and Medical Imaging, Helmholtz Zentrum, München, Germany. [5]Present address: Abbott, Sylmar, CA, USA. Correspondence and requests for materials should be addressed to L.M. (email: lmarcu@ucdavis.edu)
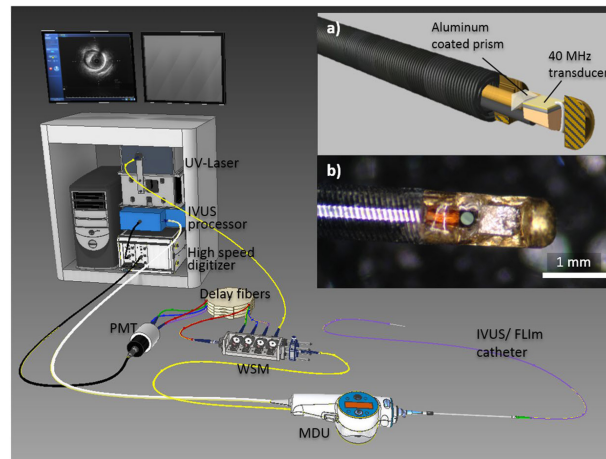
Figure 1. System overview. The system, able to display IVUS images in real time using the clinical interface, is composed of a 3.7 Fr IVUS/FLIm catheter, an IVUS motor drive unit (MDU) modified to accommodate an optical channel, connected to a wavelength selection module (WSM). The WSM enables both coupling of the pulsed excitation light and spectral decomposition of the collected fluorescence signal. The signal from each band is sent to the photomultiplier tube (PMT) using different lengths of optical delay lines that enables measurement over four wavebands using a single detector. When acquiring bimodal data, co-registration is insured by sampling both FLIm and IVUS signal with a single digitizer.

biochemical information. Thus there is a growing interest in developing "orthogonal" multimodal techniques combining biochemical and structural imaging capabilities[10, 11], which is the focus of this study.

Previous studies have demonstrated that fluorescence lifetime techniques based on UV- light induced tissue autofluorescence[12, 13] can complement IVUS to better identify distinct coronary plaque pathologies. In previous work, we developed a catheter with a small cross-section profile (3.2 Fr) relying on sequential scanning of the field of view by independent FLIm and IVUS imaging cores integrated into a single sheath and imaging section[14]. The catheter was then used to interrogate *ex vivo* human coronary arteries. The study showed that this label-free technique combining IVUS and FLIm can differentiate between 8 different plaque subtypes, identifying for example thin cap fibroatheroma (TCFA) with 90% sensitivity and 100% specificity using pathological features such as the presence of macrophages in the fibrous cap. Thus, this bi-modal technique is suitable for identification of plaque phenotypes known to be responsible for acute coronary syndromes. However, the embodiment of the FLIm-IVUS catheter technology used in this previous work was not suitable for *in vivo* use, as the device was not flexible enough and the sequential scanning scheme limited the ability to co-register data in the presence of motion. Additionally, *in vivo* coronary imaging requires displacement of blood with an optically transparent solution.

We demonstrate here how we successfully addressed these challenges by integrating IVUS and FLIm elements into a compact, single rotational intravascular catheter (3.7 Fr) able to simultaneously acquire co-registered structural (via IVUS) and biochemical (via FLIm) images of coronary arteries *in vivo* in a single pull-back. The technical performance of the bi-modal system assessed with artery phantoms. The ability of the system to acquire robust bi-modal data in coronary arteries *in vivo* using standard percutaneous coronary intervention techniques in combination with a Dextran solution bolus flush was demonstrated in healthy swine. Imaging of a few representative diseased human samples was performed and showed that different types of lesions in diseased coronary arteries, identified via histology, are characterized by FLIm biochemical signatures consistent with findings from earlier studies.

New imaging techniques for evaluation of plaque pathophysiology are of great interest to both improve the understanding of mechanisms driving plaque formation as well as support the development of new preventative, pharmaceutical and interventional therapies[10]. By providing this information, the presented device could become a valuable addition to the field of cardiovascular imaging.

Results

FLIm-IVUS imaging catheter system.
The bi-modal imaging system was developed based on a Boston Scientific iLab™ IVUS system and is composed of a custom IVUS/FLIm rotational catheter, a modified Boston Scientific motor drive unit (MDU), and data acquisition and display units of both IVUS and FLIm sub-systems (Fig. 1).
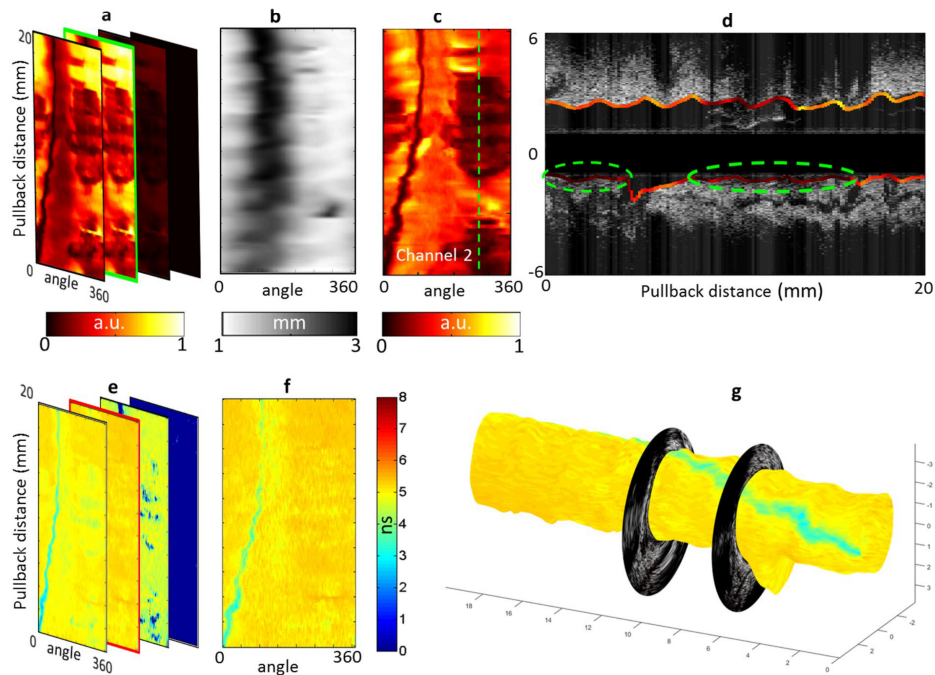
Figure 2. Ability to acquire co-registered FLIm/IVUS data *in vivo* in coronary arteries was evaluated in swine. Intensity *en face* image of a section of left circumflex artery acquired *in vivo* in pig (**a**). A distance map derived from IVUS (**b**) enables distance correction of the intensity image (**c**). For each of the four channels, a lifetime image is derived (**e**). Channel 2 presents the most fluorescence due to presence of collagen and elastin and shows very uniform background as expected from a healthy pig (**f**). The FLIm data can be combined with IVUS to provide bimodal 3D renderings (**g**) as well as sections of the vessel (**d**) (30° orientation, corresponds to the dashed line of panel c).

The size (3.7 Fr) of the FLIm/IVUS catheter reported here is compatible with coronary imaging. In its current configuration, the IVUS performance (central frequency and bandwidth) is similar to the standard 40 MHz OptiCross catheter. The modified MDU provided a robust interface with the catheter, with optical coupling losses of less than 1 dB through the MDU.

The system enables scans of a 20 mm section of vessel in 5 seconds with a rotation speed of 1800 rpm, providing 25000 independent multispectral fluorescence lifetime point measurements of the vessel surface (20 kHz laser repetition rate, 4 time average per point), co-registered with IVUS data. The data analysis software allows for display of the intensity *en face* images derived from FLIm within seconds following the scan and the fast data processing based on Laguerre technique enables the computation and display of lifetime maps from all 4 spectral channels in less than 2 minutes following the end of the scan.

In vivo FLIm/IVUS imaging of healthy coronary arteries.

The ability of the bi-modal imaging system to access coronary arteries, flush the blood from the field of view and acquire robust autofluorescence data *in vivo* was evaluated in two swines. The characterization was focused on the following: (i) ability of the catheter to access tortuous anatomy, (ii) ability to flush blood from the field of view, (iii) ability to image a range of vessel diameters, and (iv) ability to discriminate targets based on lifetime and spectral information.

Swine data obtained from a co-registered FLIm/IVUS acquisition performed *in vivo* in a 3 mm diameter section of the circumflex artery using a 5 cc/s flushing rate are presented in Fig. 2. Strong fluorescence emission was recorded in channels 1 and 2 (Fig. 2a), whereas emission is low in channel 3 and absent in channel 4, matching the emission of collagen and elastin (see supplemental material). A map of the probe-to-vessel wall distance (Fig. 2b) was extracted from IVUS data and used to correct for the effect of probe-to-wall distance on the intensity data (Fig. 2c). We observe the guidewire shadow as well as low intensity areas centered on the green dotted line shown in Fig. 2c. A longitudinal section across this line (Fig. 2d) shows that the catheter is in contact with the wall in these areas. In this
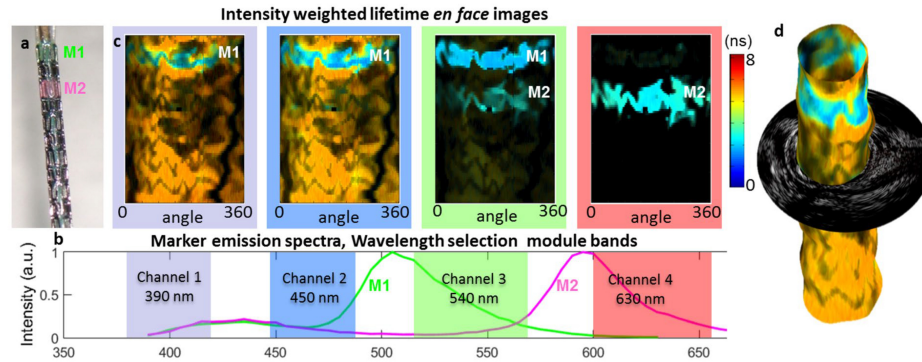
Figure 3. The ability of FLIm to resolve targets using fluorescence lifetime and spectral contrast was evaluated *in vivo* in swine coronary arteries. *In vivo* images of stented section of swine circumflex artery. Fluorescent markers M1 & M2 are painted onto the stent to provide fluorescence contrast (**a**), present broad emission spectra (**b**). M1 emission presents a short (~3 ns) lifetime and can be easily discriminated from healthy vessel background (~5.3 ns) in channels 1 and 2. M2 has weaker emission in channels 1 and 2 but is readily identified in channel 4 (**c**). The ability to resolve fluorescent features based on both spectral and temporal parameters makes FLIm a powerful technique to discriminate areas of interest. Combining FLIm and IVUS images enables 3D rendering (**d**).

configuration, blood can be trapped between the device and the vessel wall: the increased absorption of light from blood in both excitation and autofluorescence emission wavelengths creates these low intensity areas.

Fluorescence lifetime is an inherently ratiometric technique and presents the ability to extract lifetime values independent from intensity for all but the lowest measured fluorescence signal (typically SNR > 15 dB, as reported previously[15]). This property is verified by computing lifetime maps retrieved from each channel (Fig. 2e,f). After excluding the guidewire location, we verified that recovered lifetime values were uniform across the field of view as expected from a healthy artery. The recovered values for this 3 mm diameter vessel were as follows 4.98 ± 0.20 ns (channel 1), 5.19 ± 0.12 ns (channel 2), 4.55 ± 0.29 ns (channel 3), and no significant emission in channel 4. This was achieved in spite of wide variations of intensity over the field of view and noticeable signal absorption by blood in some areas, as described above. The independence of the lifetime information from signal intensity is further presented in the supplemental material. 3D rendering of the fluorescence lifetime image was also created to enable easy co-location of FLIm and IVUS features (Fig. 2g).

The ability of the catheter system to differentiate targets based on FLIm information (lifetime, spectra) was evaluated by acquiring multimodal data in a stented section as presented in Fig. 3. Fluorescence targets were painted on the stent (Fig. 3a) to provide contrast with respect to the vessel wall autofluorescence. Intensity weighted lifetime maps, where the color represents the lifetime value and the brightness represents the amount of signal, are displayed for each channel (Fig. 3c). As presented in the normalized emission spectra of both markers (Fig. 3b), the marker M1 emission is overlapping with the vessel autofluorescence emission in channels 1 and 2, but can be readily identified in these channels due to its shorter lifetime (~3.3 ns). Additional discrimination is provided by the spectral information: the peak emissions of markers M1 and M2 in channels 3 and 4 respectively provide clear identification of the location of the markers. The 3D rendering (Fig. 3d) obtained by combining FLIm and IVUS information illustrates how areas of interest identified using FLIm data can be localized within the vessel morphology representation.

Imaging large vessels presents challenges for fluorescence signal acquisition as the excitation collection efficiency decreases with probe-to-wall distance. When imaging a 5 mm diameter section of vessel, the collected fluorescence signal in the region of interest farthest from the probe was reduced by 14.5 dB with respect to the area reported for the 3 mm vessel. For this second region, the recovered lifetime values (e. g. 5.14 ± 0.33 ns in channel 2) were comparable with those obtained for smaller vessels (5.19 ± 0.12 ns in channel 2), and ensure that the system can collect data for all vessel diameters expected during coronary intervention. To evaluate the flushing parameters, the flushing flow was varied between 2 cc/s and 8 cc/s. While flushing flow below 4 cc/s did not lead to proper clearing of the blood from the field of view, no noticeable difference in flushing efficiency were identified for both smaller and larger vessel between 4, 6 and 8 cc/s flushing rates.

Ex vivo plaque characterization using FLIm and IVUS data. We present results from two representative cases chosen from human coronary arteries imaged *ex vivo* to illustrate the typical contrast provided by FLIm in diseased vessels. We will also use this data to illustrate how FLIm-derived compositional features can complement the IVUS-derived morphological features (e.g. lumen geometry, plaque thickness and presence of calcifications) enabling a more comprehensive evaluation of plaque pathophysiology. The cases consist of datasets of co-registered IVUS and multispectral FLIm from 20 mm-long arterial segments, with matching histology
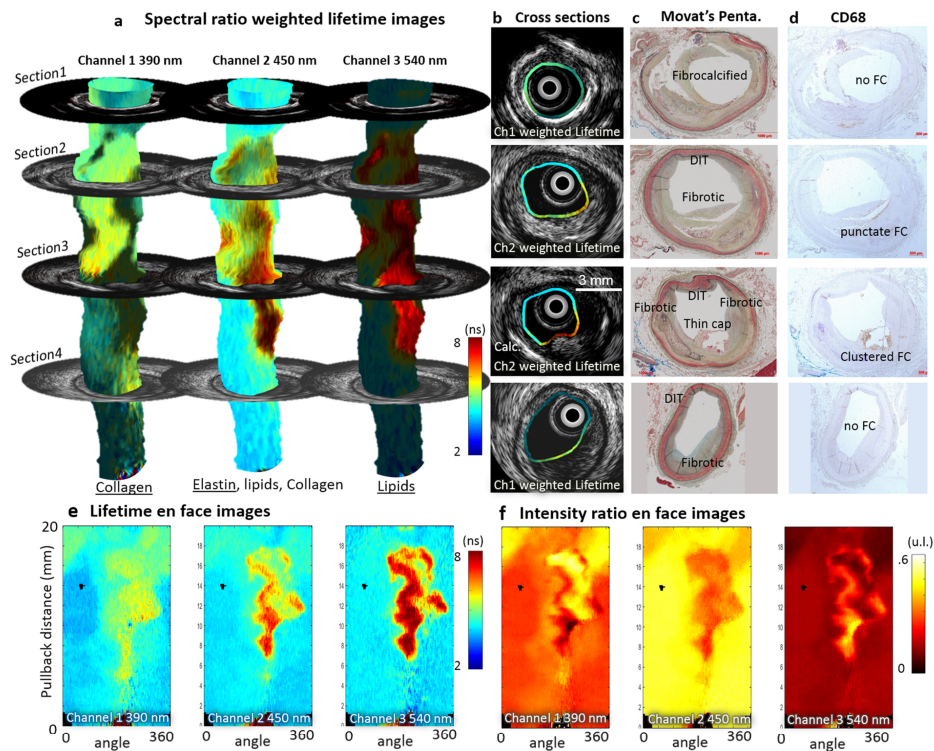
Figure 4. FLIm biochemical information supplements IVUS for the assessment of atherosclerotic lesion pathophysiology. Spectral ratio weighted lifetime images map the measured lifetime (color), as well as relative strength of the signal (brightness) for channels 1 (Collagen), 2 (Elastin, some collagen and lipids) and 3 (lipids, ceroid and lipofuscine) of the instrument. Section 1 presents a fibrocalcified lesion. Areas of superficial calcification (3 to 9 o'clock) present less fluorescence from collagen (channel 1) than the rest of the vessel. Section 2 presents diffuse intimal thickening (DIT, upper quadrant) as well as a fibrotic lesion with a deeper necrotic core (lower quadrant), easily identifiable in the IVUS cross section. The increased presence of collagen in the fibrotic area corresponds to high fluorescence intensity in channel 1. Infiltration of punctate foam cells (FC) in the lower right quadrant (see CD68) corresponds to increased lifetime in channel 2 and some low level fluorescence in channel 3. Section 3 presents a thin cap fibroatheroma (TCFA) in the lower right quadrant. The fluorescence signature of this area is characterized by an absence of channel 1 signal (no collagen) and long lifetime in channels 2 and 3 with a maximum emission in channel 3 (large amounts of lipids/ceroid/ lipofuscine). Other locations in the section present a signature expected from DIT/fibrotic lesions (collagen/ elastin). Calcification from 6–9 o'clock is readily detected by IVUS. Section 4 presents DIT (top, left) and a fibrotic lesion (bottom, right). The fibrotic area can be differentiated from DIT by its higher collagen content (increased channel 1 intensity, longer channel 2 lifetime). The absence of infiltrated FC (see CD68) in this fibrotic area is consistent with the much lower lifetime observed here with respect to the fibrotic region in section 1. Proteoglycans, identified by the alcian blue color in the 6 to 8 o'clock region of the Movat's section may explain the increase in lifetime observed at this location in the channel 1 image. En face images of lifetime (**e**) and intensity ratio (**f**) used to compute ratio weighted lifetime images shown in (**a**).

sections. The use of a dedicated sample holder during imaging enables the accurate co-registration of the imaging data with histology sections. One example is presented in Fig. 4. Results from a second artery are presented in the supplemental materials (Figs s6 and s7).

Ability of FLIm to resolve distinct cap compositions. The FLIm data are represented using spectral ratio-weighted lifetime maps, projected onto the vessel lumen segmented from the IVUS data (Fig. 4a). This representation enables both time-resolved and spectral information to be included in the same graphic representation: the lifetime measured in each of the four channels of the instrument is color-coded (see Fig. 4c), whereas

each pixel's brightness is weighted by the share of the total measured fluorescence intensity originating from this specific channel, or intensity ratio, represented in Fig. 4f (See supplemental methods section for additional details). These maps are independent from variations in excitation/collection efficiency due to distance and geometry and reflect intrinsic fluorescence properties of the superficial layer of the arterial wall (~200–300 µm[16]). These data are then compared with histology sections stained with Movat's pentachrome (Fig. 4c) and CD68 (Fig. 4d) obtained from four different axial locations.

Section 1 presents a fibrocalcified lesion. The upper region (9 to 3 o'clock) presents strong signal from collagen, as expected from a fibrous lesion. Calcified areas at the luminal surface (3 to 9 o'clock), easily identified from IVUS data and confirmed on H&E section (not shown) are characterized by a low fluorescence contribution from collagen (channel 1). Section 2 presents diffuse intimal thickening (DIT) in the upper quadrant as well as a fibrotic lesion with a deeper necrotic core (lower quadrant), easily identifiable in the IVUS cross section. The strong presence of collagen in the fibrotic area matches the high fluorescence intensity in channel 1. Infiltration of punctate foam cells (FC) in the lower right quadrant (See Fig. 4d, CD68) corresponds to increased lifetime in channel 2 (> 5.5 ns) and presence of some fluorescence in channel 3. Section 3 presents a clear instance of thin cap fibroatheroma (TCFA) in the lower right quadrant. The fluorescence signature of this area is characterized by an absence of channel 1 signal (low collagen content) and long lifetime in channels 2 (>6.5 ns) and 3 (>7.5 ns) with a maximum emission in channel 3. This large increase of lifetime may be linked to a change in the lipid composition observed in advanced lesions[17–19]. Other locations in the section present a signature expected from DIT/fibrotic lesions (collagen/elastin). Calcification from 6–9 o'clock is readily detected by IVUS. Section 4 presents DIT (top, left) and a fibrotic lesion (bottom, right). The fibrotic area can be differentiated from DIT by its higher collagen content (increased channel 1 intensity, longer channel 2 lifetime). In this fibrotic location, no infiltrated FC are visible (see Fig. 4d, CD68). This is consistent with the lifetime signature, characteristic of collagen/elastin emission and much lower than values from the fibrotic region in section 2 where foam cell infiltration was observed. The presence of proteoglycans is identified by the alcian blue color in the 6 to 8 o'clock region of the Movat's section. Reported fluorescence properties[20] are consistent with the increase in lifetime and intensity observed at this location in the channel 1 image.

The ability of FLIm to provide contrast based on both spectral and temporal information enables the delineation of various areas based on FLIm signature. While the exact source of molecular contrast is difficult to confirm with certainty (emission spectra of various compounds overlap and may contribute to the overall fluorescence signatures) the areas delineated by FLIm match well with specific plaque compositional features identified from histology.

Ability to resolve morphology. IVUS is well known for its ability to resolve vessel morphology, including lumen shape and plaque burden, due to its large penetration depth. As expected, the overall vessel shape (lumen geometry, intima thickness) observed from the acquired IVUS B-scans is very similar to the vessel geometry identified in histology sections of the corresponding axial locations; this provides a convenient way to independently verify the accuracy of imaging/histology registration. Additionally, the presence of calcification is easily identified in both IVUS and Movat's pentachrome sections (see Fig. 4, 2nd section, lower left quadrant) and also provides a clear landmark that can be used to further assess registration.

Discussion

This study demonstrates for the first time that IVUS and FLIm imaging techniques can be integrated into a single catheter to acquire co-registered structural and biochemical information *in vivo* in swine coronary arteries, without the need for exogenous contrast agents. Integration of both imaging modalities was achieved so that the performance of the clinical IVUS component was not negatively impacted by the addition of FLIm capability. More specifically, the current catheter design could access coronary arteries using standard percutaneous coronary intervention techniques in conditions representative of clinical use. We note that while in its current configuration, the image acquisition speed of the FLIm-IVUS system is limited by the framerate of the clinical IVUS from which it derives, in turn limiting the pullback length for a 5 s bolus flush to 20 mm, the main limitation of the current system The FLIm instrumentation employed enables point measurements frequencies of up to 100 KHz, corresponding to 150 frames per second (fps), compared to 30 fps of the clinical IVUS. This constraint is shared with combined IVUS-OCT and is the object of further investigation[21]. A general trend towards increased framerate for the next generation of clinical IVUS[22] will be leveraged to build a faster FLIm/IVUS system.

Use of Dextran 40 solution to flush blood from the field of view enabled the collection of bi-modality data. Low molecular weight dextran solution has high optical transparency for UV light and is a cost efficient alternative to iodinated contrast[23, 24] for intravascular OCT imaging. The flushing parameters (typically 4–5 cc/s and less than 40 mL per sequence) are compatible with clinical use. We demonstrated that the FLIm signal acquired in these experimental conditions is robust and enables differentiation of fluorescent features based on both emission spectra and lifetime differences, for vessels up to 5 mm in diameter, therefore covering the whole range of vessel lumen size expected in patients. The standard deviation of the recovered lifetime (0.1–0.3 ns range) is much lower than the fluorescence contrast observed between different lesions present in human samples (1–4 ns). We posit that the proposed device should therefore have the ability to discriminate plaque features *in vivo*.

The combination of FLIm with a morphological imaging modality such as IVUS is important, because FLIm alone cannot provide morphometric information about lumen size, geometry or direct measurement of lesion size. When projected onto the vessel lumen boundary identified by IVUS, the dimensions of FLIm features can be precisely assessed.

Data was acquired from a limited number of *ex vivo* diseased human arteries. The fluorescence signature of various lesions is consistent with findings from earlier studies from our group[12, 13]. Based on this information, we showed that FLIm complements the well-documented ability of IVUS to identify lumen size, plaque burden and

calcification. FLIm provides biochemical details about the composition of the vessel wall and allows straightforward identification of fibrotic plaque or ThCFA through the detection of an increase in collagen and a decrease of elastin content in the superficial layer of the intima[25]. TCFA, characterized by a decrease of elastin and collagen content and the presence of lipids and lipoproteins in the superficial layers of the intima could also be identified using changes in fluorescence signature, distinct from both diffuse intimal thickening and fibrotic plaques. The signal detected in channel 3 did not correspond to any of the pure compounds tested independently (supplemental materials, Fig. s4) but suggests the presence of fluorophores such as ceroid[26] and lipofuscin[27], which both have emission spectra consistent with the measured signals and are linked with the activity of inflammatory cells. Additionally, the contribution of proteoglycans to fibrotic plaque autofluorescence may be identifiable. These preliminary findings are very encouraging to support the claim that multispectral FLIm based on UV excitation of tissue autofluorescence is well suited to the intravascular identification of various biochemical species relevant to the study of plaque pathophysiology. In summary, the fluorescence signature observed for different plaque subtypes (across all 20 samples imaged in this study) was in good agreement with fluorescence properties of biochemical/morphological features, as confirmed by histology. Current results support further interrogation of a large number of coronary samples and studies designed to demonstrate statistical differences between distinct subtypes.

Although the proposed method does not provide the depth of the identified biochemical species, the penetration depth of the UV light used for excitation (~200 μm[16]) provides a sectioning effect by limiting the interrogated volume to the superficial layer, known to be of particular relevance to plaque characterization[3].

Vascular imaging can be performed using both invasive (catheter based) and non-invasive techniques. Non-invasive methods provide obvious benefits by preventing the risks associated with PCI and potentially enabling screening of patients. Such modalities now go beyond angiography and include magnetic resonance angiography (MRA), Coronary Computed Tomographic Angiography (CCTA) as well as functional imaging modalities such as positron emission tomography (PET) and single photon emission computed tomography (SPECT) supported by the development of molecular probes targeting inflammation, hypoxia or calcifications[28]. The ability of CCTA and MRA to evaluate calcifications[29] and plaque thickness[30] in coronary arteries has been documented but non-invasive imaging of atherosclerosis in coronary arteries is hampered by radiation exposure for PET/SPECT and CT, limited spatial resolution and image quality as well as motion artifacts[28] and will require significant technological improvements before potentially replacing intravascular imaging methods. In contrast to CCTA or MRA, IVUS has been able for 20 years to provide clinicians with detailed morphological information about coronary plaque but stenosis and plaque burden alone are poor predictors of acute coronary syndrome[31]. In spite of improvement in spatial resolution provided by OCT in comparison to IVUS, it is also unlikely that morphological information alone will enable identification of rupture-prone plaque[32]. Catheter-based near infrared spectroscopy (NIRS)-ultrasound, now available for clinical use, provides clinicians with "chemograms" that display the presence of lipid in the vessel wall. However, the absence of depth resolution, combined with a relatively high penetration depth (multiple millimeters), may lead to ambiguous information with respect to volume or localization of these lipids, thus limiting the clinical value of the information. Molecular imaging methods such as near infrared fluorescence (NIRF), implemented at the research level in NIRF-OCT multimodal approaches aim to identify lipid-rich and inflamed plaque using both exogenous markers[33, 34] and label free approaches[35]. The ability of NIRF-OCT to detect inflammation has promising potential. Nonetheless, these modalities lack the ability to assess the presence and potential degradation of structural proteins such as collagen and elastin. In contrast, the bi-modal FLIm-IVUS system reported here is able to evaluate and characterize plaque based on the presence of structural proteins such as collagen and elastin as well as peroxidized lipid-protein complex (ceroid) and foam cells near the surface of the lumen. Combined with the well documented ability of IVUS to evaluate lumen shape, plaque burden and calcification, this instrument provides an exciting option for the *in vivo* study and detection of various plaque subtypes.

This new approach may benefit both patients and researchers alike. Enabling *in vivo* evaluation of plaque type may improve understanding of plaque physiopathology and mechanisms of disruption. In addition, the effect of therapeutic agents on biochemical and structural composition of plaque could be evaluated, leading to a non-invasive method to monitor efforts aimed at acute coronary syndromes prevention.

Methods

Integrated FLIm/IVUS system.
FLIm is based on a fast pulse sampling technique previously developed by our group[36]. Pulses of UV-light (355 nm, 20 kHz) are sent to the sample and generate fluorescence emission from the arterial wall that results from the autofluorescence of structural proteins (collagen, elastin), as well as lipids and lipoproteins. The UV pulses were delivered to the arterial wall using a fiber optic. The generated autofluorescence signal was collected using the same fiber and spectrally resolved in four distinct wavelength bands: Channel 1 (390 nm), Channel 2 (450 nm), Channel 3 (540 nm) and Channel 4 (630 nm). The correspondence between channels and key fluorophores is presented in Table 1 of the supplemental methods. FLIm imaging capability was integrated into the existing IVUS system by modifying the IVUS MDU to accommodate an optical channel and developing a custom 3.7 Fr monorail bi-modal imaging catheter (Fig. 1). The system is able to display IVUS information in real time using the standard user interface and provides guidance to identify areas of interest, as well as co-registered FLIm/IVUS images as demonstrated in phantom (see supplemental material).

Data were processed to make optimal use of the ability of the system to differentiate biochemical compounds using fluorescence decay characteristics as well as spectral intensities: for each channel, fluorescence lifetime and intensity ratio maps were created. Additional information about data processing is available in the supplemental methods.

***In vivo* coronary imaging in swine.** This study was conducted in accordance with the Guide for the Care and Use of Laboratory Animals[37]. The Institutional Animal Care and Use Committee at the University of California, Davis approved the study for the use of Yorkshire cross swine. Animal care and use was performed by qualified individuals and supervised by veterinarians. All facilities and transportation complied with current legal requirements and guidelines. Anesthesia was used in all surgical interventions. Our animal facilities meet the standards of the American Association for Accreditation of Laboratory Animal Care.

The pigs, in the 60–70 kg range, were subject to general anesthesia and the bi-modal catheter device was introduced into the left circumflex coronary under fluoroscopy guidance through a standard 7 French guiding catheter over a 0.014 inch guidewire. Detail of the protocol can be found in the supplemental materials.

In the first animal, an initial set of bi-modal pull-back scans (n = 10) was acquired in vessel diameters ranging from 1.5 mm to 3.5 mm using non-occlusive flush (4 to 8 cc/s for 10 s) of low molecular weight Dextran solution (10% LMD in 5% Dextrose, Hospira, IL) to remove blood from the field of view. The 2.75 mm stent (Promus, Boston Scientific, MA) with fluorescent markers (Scribbles, Duncan, Fresno, CA) was then placed in the circumflex coronary artery. The stented area, where lifetime and spectral emission contrast between markers and healthy vessel wall is expected, was subsequently imaged with the IVUS/FLIm catheter. In the second animal, a similar procedure was adopted: images were acquired in vessels with diameters ranging from 3 mm to 5 mm using flushing flow rates between 2 cc/s and 8 cc/s to confirm the results from the first animal and evaluate a wider range of vessel sizes.

***Ex vivo* human coronary imaging.** The arteries (n = 21) were provided by the University of Pennsylvania heart transplant program. Whole human hearts were procured from two separate patient groups: non-failing brain dead organ donors with no overt history of heart failure, and end stage heart failure transplant patients. No organs were procured from prisoners. All hearts received *in situ* cold cardioplegia and were placed on wet ice in 4 degree Krebs-Henseleit Buffer. Artery samples were removed and snap frozen in liquid nitrogen and stored at minus 80 °C. Arteries were de-identified prior to shipping from University of Pennsylvania to UC Davis. The study complies with current legal requirements and guidelines and was approved by the University of Pennsylvania Hospital Institutional Review Board as well as UC Davis Biological Use Authorization. Prospective informed consent for research use of heart tissue was obtained from all transplant recipients and next-of-kin in the case of organ donors.

Samples were mounted on a dedicated holder and immersed in 37 °C Phosphate buffered saline (PBS) solution. PBS was circulated inside the vessel during imaging to maintain lumen shape. Following imaging, the samples were fixed under perfusion, and sent to the Texas Heart Institute for further processing, sectioning and staining. Each artery segment was first cut into rings (~2 mm length). Sections were cut at four different locations for each ring, leading to at least 32 histology sections per sample. Visualization of plaque morphology and composition (collagen, elastin, and lipids) was enabled by H&E and Movat's pentachrome, correspondingly. Immunohistostaining with CD68 was also performed to visualize macrophage content in the vessel wall.

References

1. Finegold, J. A., Asaria, P. & Francis, D. P. Mortality from ischaemic heart disease by country, region, and age: Statistics from World Health Organisation and United Nations(). *Int. J. Cardiol.* **168**, 934–945 (2013).
2. Lowe, H. C., Narula, J., Fujimoto, J. G. & Jang, I.-K. Intracoronary Optical DiagnosticsCurrent Status, Limitations, and Potential. *JACC Cardiovasc. Interv.* **4**, 1257–1270 (2011).
3. Burke, A. P. *et al.* Coronary Risk Factors and Plaque Morphology in Men with Coronary Disease Who Died Suddenly. *N. Engl. J. Med.* **336**, 1276–1282 (1997).
4. Tearney, G. J. *et al.* Quantification of Macrophage Content in Atherosclerotic Plaques by Optical Coherence Tomography. *Circulation* **107**, 113 (2003).
5. Wang, J. *et al.* Near-infrared spectroscopic characterization of human advanced atherosclerotic plaques. *J. Am. Coll. Cardiol.* **39**, 1305–1313 (2002).
6. Gardner, C. M. *et al.* Detection of Lipid Core Coronary Plaques in Autopsy Specimens With a Novel Catheter-Based Near-Infrared Spectroscopy System. *JACC Cardiovasc. Imaging* **1**, 638–648 (2008).
7. van de Poll, S. W. E., Römer, T. J., Puppels, G. J. & van der Laarse, A. Raman Spectroscopy of Atherosclerosis. *J. Cardiovasc. Risk* **9**, 255–261 (2002).
8. Maarek, J.-M. I., Marcu, L., Fishbein, M. C. & Grundfest, W. S. Time-resolved fluorescence of human aortic wall: Use for improved identification of atherosclerotic lesions. *Lasers Surg. Med.* **27**, 241–254 (2000).
9. Jaffer, F. A. *et al.* Two-Dimensional Intravascular Near-Infrared Fluorescence Molecular Imaging of Inflammation in Atherosclerosis and Stent-Induced Vascular Injury. *J. Am. Coll. Cardiol.* **57**, 2516–2526 (2011).
10. Bourantas, C. V. *et al.* Hybrid intravascular imaging: recent advances, technical considerations, and current applications in the study of plaque pathophysiology. *Eur. Heart J.*, doi:10.1093/eurheartj/ehw097 (2016).
11. Ma, T., Zhou, B., Hsiai, T. K. & Shung, K. K. A Review of Intravascular Ultrasound–Based Multimodal Intravascular Imaging: The Synergistic Approach to Characterizing Vulnerable Plaques. *Ultrason. Imaging*. doi:10.1177/0161734615604829 (2015).
12. Marcu, L. *et al.* Detection of rupture-prone atherosclerotic plaques by time-resolved laser-induced fluorescence spectroscopy. *Atherosclerosis* **204**, 156–164 (2009).
13. Fatakdawala, H. *et al.* Fluorescence Lifetime Imaging Combined with Conventional Intravascular Ultrasound for Enhanced Assessment of Atherosclerotic Plaques: an *Ex Vivo* Study in Human Coronary Arteries. *J. Cardiovasc. Transl. Res.* doi:10.1007/s12265-015-9627-3 (2015).
14. Ma, D. *et al.* Rotational multispectral fluorescence lifetime imaging and intravascular ultrasound: bimodal system for intravascular applications. *J. Biomed. Opt.* **19**, 066004–066004 (2014).
15. Ma, D., Bec, J., Gorpas, D., Yankelevich, D. & Marcu, L. Technique for real-time tissue characterization based on scanning multispectral fluorescence lifetime spectroscopy (ms-TRFS). *Biomed. Opt. Express* **6**, 987–1002 (2015).
16. Marcu, L., Fishbein, M. C., Maarek, J.-M. I. & Grundfest, W. S. Discrimination of Human Coronary Artery Atherosclerotic Lipid-Rich Lesions by Time-Resolved Laser-Induced Fluorescence Spectroscopy. *Arterioscler. Thromb. Vasc. Biol.* **21**, 1244–1250 (2001).
17. Stary, H. C. *et al.* A definition of initial, fatty streak, and intermediate lesions of atherosclerosis. A report from the Committee on Vascular Lesions of the Council on Arteriosclerosis, American Heart Association. *Circulation* **89**, 2462–2478 (1994).

18. Upston, J. M. *et al*. Disease Stage-Dependent Accumulation of Lipid and Protein Oxidation Products in Human Atherosclerosis. *Am. J. Pathol.* **160**, 701–710 (2002).
19. Spite, M. & Serhan, C. N. Lipid Signatures of Unstable Atheromas: Fossils or a Step Toward Personalized Lipidomics-Metabolomics? *Circ. Cardiovasc. Genet.* **4**, 215–217 (2011).
20. Angheloiu, G. O. *et al*. Detection of Coronary Atherosclerotic Plaques with Superficial Proteoglycans and Foam Cells using Real-Time Intrinsic Fluorescence Spectroscopy. *Atherosclerosis* **215**, 96–102 (2011).
21. Li, J. *et al*. Ultrafast optical-ultrasonic system and miniaturized catheter for imaging and characterizing atherosclerotic plaques *in vivo*. *Sci. Rep.* **5**, 18406 (2015).
22. Syed, M. A. & Hodgson, J. M. Enhanced IVUS: Advances Allowing Higher Resolution and Integrated Devices. *Curr. Cardiovasc. Imaging Rep.* **9**, 23 (2016).
23. Ozaki, Y. *et al*. Comparison of Contrast Media and Low-Molecular-Weight Dextran for Frequency-Domain Optical Coherence Tomography. *Circ. J.* **76**, 922–927 (2012).
24. Frick, K. *et al*. Low molecular weight dextran provides similar optical coherence tomography coronary imaging compared to radiographic contrast media. *Catheter. Cardiovasc. Interv.* **84**, 727–731 (2014).
25. Bentzon, J. F., Otsuka, F., Virmani, R. & Falk, E. Mechanisms of Plaque Formation and Rupture. *Circ. Res.* **114**, 1852 (2014).
26. Haka, A. S., Kramer, J. R., Dasari, R. R. & Fitzmaurice, M. Mechanism of ceroid formation in atherosclerotic plaque: *in situ* studies using a combination of Raman and fluorescence spectroscopy. *J. Biomed. Opt.* **16**, 011011-011011–7 (2011).
27. Croce, A. C. & Bottiroli, G. Autofluorescence spectroscopy and imaging: a tool for biomedical research and diagnosis. *Eur. J. Histochem. EJH* **58**, 2461 (2014).
28. Tarkin, J. M. *et al*. Imaging Atherosclerosis. *Circ. Res.* **118**, 750 (2016).
29. Motoyama, S. *et al*. Computed tomographic angiography characteristics of atherosclerotic plaques subsequently resulting in acute coronary syndrome. *J. Am. Coll. Cardiol.* **54**, 49–57 (2009).
30. Fayad, Z. A. *et al*. Safety and efficacy of dalcetrapib on atherosclerotic disease using novel non-invasive multimodality imaging (dal-PLAQUE): a randomised clinical trial. *The Lancet* **378**, 1547–1559 (2011).
31. Garcia-Garcia, H. M. *et al*. Imaging plaques to predict and better manage patients with acute coronary events. *Circ. Res.* **114**, 1904–1917 (2014).
32. Phipps, J. E. *et al*. Diagnosis of Thin-Capped Fibroatheromas in Intravascular Optical Coherence Tomography Images: Effects of Light Scattering. *Circ. Cardiovasc. Interv.* **9**, (2016).
33. Lee, S. *et al*. Fully Integrated High-Speed Intravascular Optical Coherence Tomography/Near-Infrared Fluorescence Structural/Molecular Imaging *In Vivo* Using a Clinically Available Near-Infrared Fluorescence–Emitting Indocyanine Green to Detect Inflamed Lipid-Rich Atheromata in Coronary-Sized Vessels. *Circ. Cardiovasc. Interv.* **7**, 560–569 (2014).
34. Yoo, H. *et al*. Intra-arterial catheter for simultaneous microstructural and molecular imaging *in vivo*. *Nat Med* **17**, 1680–1684 (2011).
35. Wang, H. *et al*. Ex vivo catheter-based imaging of coronary atherosclerosis using multimodality OCT and NIRAF excited at 633 nm. *Biomed. Opt. Express* **6**, 1363–1375 (2015).
36. Yankelevich, D. R. *et al*. Design and evaluation of a device for fast multispectral time-resolved fluorescence spectroscopy and imaging. *Rev. Sci. Instrum.* **85**, (2014).
37. Council, N. R. Guide for the Care and Use of Laboratory Animals: Eighth Edition. (The National Academies Press, 2011).

Acknowledgements

Author Contributions

J.B. designed and developed the multimodal catheter system. D.M. designed and developed the code used for system control and data acquisition. J.B. and D.G. developed the data processing code. J.B., L.M. and J.S. designed the studies. L.M. supervised system design and integration. K.B.M. provided *ex vivo* samples J.B., D.M., H.F. and J.S. conducted the study. J.B., D.G. and J.P. processed the data. J.B. and L.M. wrote the manuscript, and all authors contributed to critical revision of the article as well as final approval of the version to be published.

Additional Information

Supplementary information accompanies this paper at doi:10.1038/s41598-017-08056-0

Competing Interests: The authors declare that they have no competing interests.

Publisher's note: Springer Nature remains neutral with regard to jurisdictional claims in published maps and institutional affiliations.

[P2] Broadband, freeform focusing micro-optics for side-viewing imaging catheter (2019)

Reprinted with permission from [Julien Bec, Cai Li, and Laura Marcu, "Broadband, freeform focusing micro-optics for a side-viewing imaging catheter," Opt. Lett. 44, 4961-4964 (2019)] © The Optical Society

Erklärungen zu den Eigenanteilen des Promovenden sowie der weiteren Doktoranden/Doktorandinnen als Koautoren an der Publikation.

[1]J. Bec, [2]C. Li, and [3]L. Marcu, "In vivo label-free structural and biochemical imaging of coronary arteries using an integrated ultrasound and multispectral fluorescence lifetime catheter system," Scientific Reports 7, 8960 (2017).			
Beteiligt an (Zutreffendes ankreuzen)			
	1	2	3
Konzeption des Forschungsansatzes	X		X
Planung der Untersuchungen	X		
Datenerhebung	X	X	
Datenanalyse und Interpretation	X	X	
Schreiben des Manuskripts	X		X
Vorschlag Anrechnung Publikationsäquivalent	1.0		

Broad-band, freeform focusing micro-optics for side-viewing imaging catheter

JULIEN BEC[1,2,3,4] ,CAI LI[1] ,LAURA MARCU[1*]

[1]Department of Biomedical Engineering, University of California, Davis, California 95616, USA
[2]Institute of Physical Chemistry and Abbe Center of Photonics (IPC), Friedrich-Schiller-University, D-07743 Jena, Germany
[3]Leibniz Institute of Photonic Technology, D-07745 Jena, Germany
[4]email: jbec@ucdavis.edu
*Corresponding author: lmarcu@ucdavis.edu

Successful implementation of catheter-based imaging system relies on the integration of high performance miniaturized distal end optics. Typically, compensation of chromatic dispersion, as well as astigmatism introduced by the device's sheath could only be addressed by combining multiple optical elements, adversely impacting size and manufacturability. Here, we present a 300 x 300 x 800 μm^3 monolithic optic that provides high optical performances over an extended wavelength range (near UV-visible-IR) with minimal chromatic aberrations. The design of the optic, fully optimized using standard optical simulation tools, provides the ability to freely determine aperture and working distance. Manufacturing is cost effective and suited for prototyping and production alike. The experimental characterization of the optics demonstrates a good match with simulation results and performances well suited to both optical coherence tomography and fluorescence imaging, thus paving the way for high-performance multimodal endoscopy systems. © 2019 Optical Society of America

http://dx.doi.org/10.1364/OL.99.099999

Fiber optic endoscopic probes have enabled breakthroughs in medical imaging because of their unique ability to reach deep into the human body. The combination of a low profile side-viewing probe with a helical scanning pattern enables the rapid acquisition of images from luminal structures. Several techniques, such as optical coherence tomography [1], spectroscopy [2], and fluorescence [3,4] have been successfully implemented following this principle, with applications for the detection of diseases in coronary arteries [1,5], gastrointestinal tract [1] as well as airways [6]. A key component for the successful implementation of fiber-based imaging techniques is the distal optical elements, used to direct and focus the optical beam, which should provide high optical performances in a small form factor. More specifically, the optic should provide the working distance, and numerical aperture suitable for the application, with the introduction of minimal aberrations (spherical, chromatic). For typical optical systems, these design goals are addressed by combining multiple optical elements but the scaling of such solutions to sub-millimeter dimensions presents significant challenges. Additionally, certain elements specific to an endoscope, such as the transparent sheath typically used to separate the rotating imaging core from the surrounding environment introduce astigmatism that should ideally be corrected [5]. In the last years, the combination of imaging modalities operating at different wavelengths has become more widespread [7–9], further highlighting the need for a distal end optic solution able to work over an extended wavelength range. The typical solutions for compact distal end optics, namely gradient index (GRIN) and ball lens optics have been successfully implemented for the construction of low-profile side viewing endoscopes, but both present limitations.

Angle-polished fused ball lenses are fabricated by splicing a short section of no-core fiber with the main fiber, fused into a spheroid, and polished to provide an angled facet that deflects the beam via total internal reflection [10]. Different radii can be obtained in the axial and trans-axial directions to correct for astigmatism introduced by the device sheath. A suitable geometry of the spheroid is achieved empirically by optimizing the fusion process. Ball lens termination of large core multimode fibers (>100 μm) presents additional challenges as the optical beam expansion is limited by the diameter of the no core fiber. This limitation has been reported when using the inner cladding of a double clad fiber to deliver a Fluorescence Lifetime Imaging (FLIm) excitation beam for a FLIm/OCT application [11]. Additionally, the use of the probe in liquids requires the addition of a cap as both total internal reflection from the facet and focusing from the surface of the spheroid relies on a glass/ air interface. This cap increases astigmatism, bulk and complexity [12].

GRIN lenses are used in the visible and near-infrared range but common dopants such as sliver ions present strong absorption and autofluorescence at 355 nm. Lithium is a UV compatible dopant but limits in the refractive index variations lead to a low numerical aperture (NA) of 0.2 [13]. This leads to long (>3mm) elements not suitable for vascular use. Other limitations are strong chromatic aberrations and an optical index profile that presents a circular symmetry thus does not enable the correction of astigmatism introduced by the device sheath [14,15]. The introduction of an additional cylindrical surface addresses this issue at the cost of increased complexity [14].

A 3D printed side viewing optic for OCT application that relies on the reflection off a curved paraboloid surface was reported recently [16]. Although it shares many of the advantages of the solution proposed here, manufacturing is slow (>14 h per element). The design, based on total internal reflection, required a cap that increases the overall bulk of the element. Additionally, the UV-curable photoresist material presents lower mechanical properties (E= 4.5 GPa), high absorption in the UV range and overall lower optical performances than fused silica.

A different concept, using diffractive optical elements (DOE) as an alternative to GRIN and ball lenses has been addressing some of the issues of conventional optics for OCT [15]. DOEs are well suited to monochromatic, spatially coherent light, but the application of this technology to extended sources (such as multimode fibers) over a large wavelength range presents significant challenges [17].

Here, we present the design, fabrication, and characterization of a novel monolithic distal-end optics concept able to address these issues: This design enables full control of the working distance, NA, correction of spherical aberration, as well as astigmatism introduced by the device's sheath and is inherently broadband, thus supporting the implementation of imaging modalities spanning the UV-IR range, such as OCT and FLIm in a single device.

The micro-optic described here consists of a fused silica element terminated by a reflective curved back surface that performs beam focusing and reflection. In an ideal configuration, with light emitted from a point source (fiber core), the back surface could consist of an ellipsoid section where the first focus F1 is collocated with the source, such that all rays emitted from the source would converge to the second focus F2 (Fig 1a). In practical applications, the need to correct for sheath astigmatism and additional refraction of the light at the exit face (glass to water or air), led to the optimization of the back-surface geometry using optical simulation.

In this study, the geometry of the reflective surface was computed using Zemax (Radiant, Redmont, WA). The simulated model consisted of a fully filled 0.22 NA, 100 μm core multimode fiber and a UV-fused silica optical element of 300x300μm² cross-section, immersed in water and surrounded by a 0.96/1.25 mm inner/outer diameter TPX sheath (MX004, Mitsui Chemicals, Japan). The freeform reflective surface sag was defined as a conic asphere with an additional polynomial aspheric terms, where x and y are the transaxial and axial coordinates (Fig 1d), and k, r and a are the conic constant, normalization radius and aspheric coefficient, respectively. (Eq. 1):

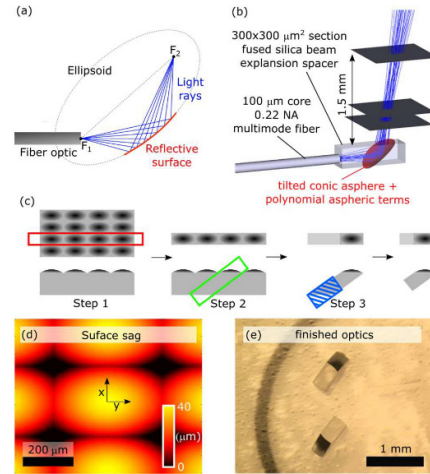$$z = \frac{(x^2 + y^2)}{r\left(1 + \sqrt{1 - (1+k)\frac{(x^2+y^2)}{r^2}}\right)} + ax^2 \qquad (Eq.1)$$

Fig. 1. **Design and manufacturing of freeform optics.** (a) Simplified representation: a section of ellipsoid reflects and focuses light rays exiting the fiber core. (b) Zemax simulation model used to perform optimization of the reflective surface. (c) Manufacturing process: the coated array is first cut into individual rows (step 1), individual elements are cut from each row (step 2), and polished to the designed length (step 3). (d) The surface sag representation of the curved reflective surface highlights that axial and transaxial directions have different curvature radii, thus enabling astigmatism correction. (e) Individual optics after manufacturing completion.

Numerical optimization of the surface parameters (r=1.323 mm, k=-48, a=.414 mm⁻²) and tilt (49.6 deg) was performed to provide 10 degrees forward beam tilt and minimize the beam root mean square (RMS) radius at 1.5 mm distance (Fig 1b).

The fabrication of the elements consisted of manufacturing a microlens-like array of the micro-optic back surface out of a fused silica wafer using direct-write laser machining (PowerPhotonics, Fife, UK) [18]. After machining, a UV enhanced aluminum coating was applied to provide broadband reflectivity in the UV-Visible range (Laseroptik, Garbsen, Germany) (Fig 1c). Individual micro-optics were separated by a 2-step dicing operation: the array was first cut into rows (Fig 1c step 1), then individual elements (Fig 1c step 2), and polished to length using diamond lapping sheets (LFXD, Thorlabs, Newton, NJ, USA) (Fig 1c step 3).

The freeform optics were assembled with a 1m length of 100 μm core multimode fiber optic (FVP100110125, Polymicro, Phoenix, AZ, USA) using acrylate optical adhesive (OG603, Epotek, Billerica, MA, USA). This assembly was connected to the FLIm system reported earlier by our group [19] to perform the experimental characterization. The beam profile of the UV excitation beam was measured at different distances (0 to 4 mm) using a 20X microscope objective and a 2,048x1,536 CMOS camera (MD310B-BS, AMScope), leading to a pixel size of .716 μm. Multimode beams do not necessarily present a Gaussian profile, therefore the axial and transaxial beam profiles were fitted with different orders of supergaussian (n=2 to 10) according to Eq. 2.
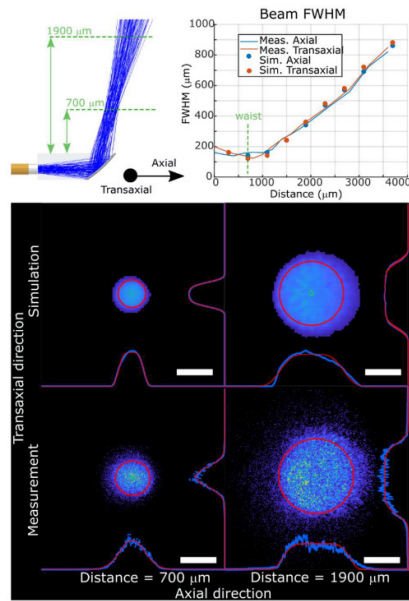
Fig. 2. The experimentally characterized multimode beam is in good agreement with the beam shape derived from simulations. For each distance, the beam dimensions in the axial and transaxial directions are defined as the full-width half-maximum of the super-Gaussian fit that best approximates the beam profile. For all distances, minimal differences in beam size across the two directions are observed. Red circle: 80% encircled energy. Scale bar: 200 μm

$$I(r) = I_0 exp \left[-2 \left(\frac{r}{w} \right)^n \right] \qquad (Eq.2)$$

For each distance, the supergaussian order that resulted in the least residual was used. The beam size was then computed as the full-width half-maximum (FWHM) of the fitted profile and compared with the beam profile computed from Zemax simulation performed in similar conditions (in air, no sheath) (Fig. 2).

The ability of the micro-optic design to improve fluorescence collection and lateral resolution was evaluated by coupling the probe with the system described in [4], and measuring fluorescence from a 200 μm polystyrene film for distances in a 0-4 mm range, as well as a 3 mm stent inserted in a fluorescent acrylic phantom. The results were compared to reference probes terminated with flat reflective prisms (Fig. 3).

The suitability of the micro-optic for intravascular OCT was evaluated by coupling the micro-optic *with* a 1m length of double-clad fiber (DCF 9/105/125, Nufern, USA). After connection to a 1310±55 nm swept source OCT engine from Axsun Technologies, we measured the beam profile for distances of 0 to 3 mm from the optic's top surface. *T*he axial and transaxial beam profiles were fitted with Gaussian functions to extract the beam's FWHM (Fig. 4).
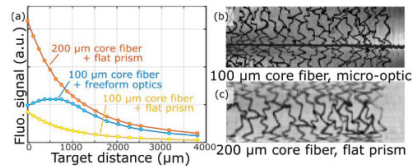
Fig. 3. Experimental validation of improved collection efficiency and lateral resolution: variation of fluorescence signal in function of distance, for freeform optic and flat prism (a). Fluorescence image of stent illustrating improvements in spatial resolution obtained using the proposed optic (b) with respect to an earlier version of the device (c)
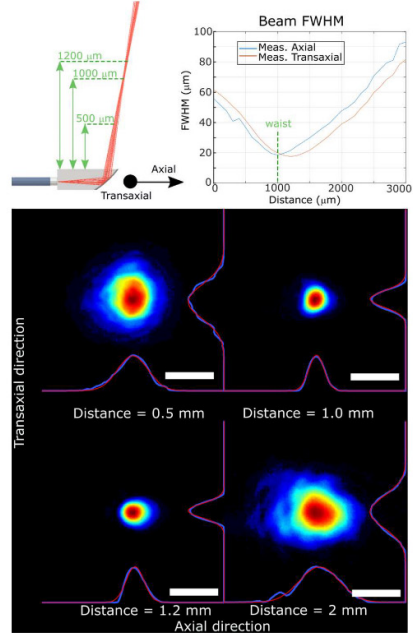
Fig. 4. Ex**perimentally characterization of optical performances for a single mode beam.** The beam profile in the axial and transaxial directions presents low aberrations and a FWHM of less than 20 μm at the waist. For all distances, only minimal differences in beam size across the two directions are observed. Scale bar: 50 μm

The optimization of the element's back surface geometry based on project-specific constraints (aperture, working distance, beam tilt, presence of a sheath) was straightforward. Manufacturing this geometry using direct laser machining did not present specific *challenges,* as the surfaces are smooth and present a low slope and a sag of less than 50 μm. No characterization of the machining accuracy was performed, but based on manufacturing guidelines

provided by the manufacturer for low slope designs (<8 degrees), a typical peak-to-valley form error of 0.5 µm is expected [20].

Due to the small dimensions of each optical element, a high number of elements (>900) could be included within the 15x15 mm² area available for machining. Application of the broadband reflective coating of the back surface on hundreds of optics at once was easy and cost-effective. The following dicing and polishing operations were performed using a standard dicing saw and polishing equipment, readily available in a research environment.

Experimental characterization demonstrates that the micro-optics performances are in good agreement with the fluorescence excitation beam simulations performed to generate the design. Beam profiles at various distances, in the axial and transaxial directions, closely match simulated beam profiles and show negligible astigmatism with similar beam waist distance and beam divergence in the axial and transaxial directions.

These optics are well suited for FLIm, due to high UV transparency and low autofluorescence, and ability to work with large core multimode fibers. Here, we demonstrate that the micro-optic, combined with a 100 µm core fiber, presents a collection efficiency vastly superior to the same fiber terminated with a flat prism. It almost matches the collection efficiency obtained by an earlier versions of the FLIm catheter combining a flat prism with a 200 µm core fiber that presents 4 fold larger cross section [4], while simultaneously enabling improvements in lateral resolution) .

The same design demonstrates high performances for a 1310 nm OCT application: the waist position in the axial and transaxial directions is within 200 µm and the beam presents similar divergence in both directions. Additionally, the beam FWHM of less than 20 µm in the focal plane.

The design presented here delivers superior optical performances over an extended wavelength range: optical rays travel in a straight line within the beam expansion region, and focusing is achieved via specular reflection off the back surface. The introduction of chromatic dispersion is limited to the refraction off the exit surface of the element. It is minimal as the surface is flat and the beam presents a low divergence and angle of incidence. Therefore, this design compares favorably to refractive optics that are subject to significant chromatic aberrations, potentially corrected by the addition of multiple optical elements to compensate for wavelength dispersion. Finally, this design is suitable for use in air as well as water and is impervious to contaminations of the reflective surface. This proves valuable for integration into devices (Fig. 5)

In summary, compact, monolithic micro-optic elements that present an achromatic behavior over a large wavelength range, astigmatism correction and straightforward optimization of aperture and working distances are easily manufactured. This combination of features could only be obtained previously using a combination of optical elements. The direct-write laser machining of the freeform back surface does not require the upfront investment necessary for alternative techniques such as grayscale lithography or molding and can be easily outsourced. Several hundred optics can be manufactured from the same wafer and can include a large variety of alternative designs, making it suitable for R&D and production alike, thus enabling improvements in intraluminal imaging devices in both research and clinical environments.
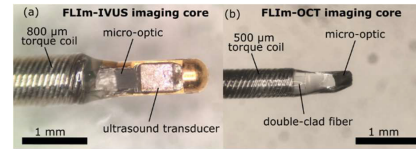

Fig. 5. Integration of the freeform optics into intravascular imaging devices. FLIm-IVUS intravascular catheter (a). Low profile FLIm-OCT intravascular catheter core (b).

References
1. S. H. Yun, G. J. Tearney, B. J. Vakoc, M. Shishkov, W. Y. Oh, A. E. Desjardins, M. J. Suter, R. C. Chan, J. A. Evans, I.-K. Jang, N. S. Nishioka, J. F. de Boer, and B. E. Bouma, Nat. Med. **12**, (2006).
2. C. M. Gardner, H. Tan, E. L. Hull, J. B. Lisauskas, S. T. Sum, T. M. Meese, C. Jiang, S. P. Madden, J. D. Caplan, A. P. Burke, R. Virmani, J. Goldstein, and J. E. Muller, JACC Cardiovasc. Imaging **1**, (2008).
3. R. N. Razansky, A. Rosenthal, G. Mallas, D. Razansky, F. A. Jaffer, and V. Ntziachristos, Opt. Express **18**, (2010).
4. J. Bec, J. E. Phipps, D. Gorpas, D. Ma, H. Fatakdawala, K. B. Margulies, J. A. Southard, and L. Marcu, Sci. Rep. **7**, (2017).
5. B. E. Bouma, M. Villiger, K. Otsuka, and W.-Y. Oh, Biomed. Opt. Express **8**, (2017).
6. M. Tsuboi, A. Hayashi, N. Ikeda, H. Honda, Y. Kato, S. Ichinose, and H. Kato, Lung Cancer **49**, (2005).
7. S. Lee, M. W. Lee, H. S. Cho, J. W. Song, H. S. Nam, D. J. Oh, K. Park, W.-Y. Oh, H. Yoo, and J. W. Kim, Circ. Cardiovasc. Interv. **7**, (2014).
8. H. Pahlevaninezhad, A. M. D. Lee, A. Ritchie, T. Shaipanich, W. Zhang, D. N. Ionescu, G. Hohert, C. MacAulay, S. Lam, and P. Lane, Biomed. Opt. Express **6**, (2015).
9. B. E. Sherlock, J. E. Phipps, J. Bec, and L. Marcu, Opt. Lett. **42**, (2017).
10. V. X. D. Yang, Y. X. Mao, N. Munce, B. Standish, W. Kucharczyk, N. E. Marcon, B. C. Wilson, and I. A. Vitkin, Opt. Lett. **30**, (2005).
11. M. W. Lee, J. W. Song, W. J. Kang, H. S. Nam, T. S. Kim, S. Kim, W.-Y. Oh, J. W. Kim, and H. Yoo, Sci. Rep. **8**, (2018).
12. J. Li, T. Ma, J. Jing, J. Zhang, P. M. Patel, K. Kirk Shung, Q. Zhou, and Z. Chen, J. Biomed. Opt. **18**, (2013).
13. "GRINTECH GmbH Gradient Index Optics," https://www.grintech.de/en/gradient-index-optics/.
14. J. Xi, L. Huo, Y. Wu, M. J. Cobb, J. H. Hwang, and X. Li, Opt. Lett. **34**, (2009).
15. H. Pahlevaninezhad, M. Khorasaninejad, Y.-W. Huang, Z. Shi, L. P. Hariri, D. C. Adams, V. Ding, A. Zhu, C.-W. Qiu, F. Capasso, and M. J. Suter, Nat. Photonics **12**, (2018).
16. J. Li, P. Fejes, D. Lorenser, B. C. Quirk, P. B. Noble, R. W. Kirk, A. Orth, F. M. Wood, B. C. Gibson, D. D. Sampson, and R. A. McLaughlin, Sci. Rep. **8**, (2018).
17. G. Kim, J. A. Domínguez-Caballero, and R. Menon, Opt. Express **20**, (2012).
18. Matthew Currie and Roy McBride, (2014), Vol. 8970.
19. D. Ma, J. Bec, D. R. Yankelevich, D. Gorpas, H. Fatakdawala, and L. Marcu, J. Biomed. Opt. **19**, (2014).
20. "LightForge Technical Data," http://www.powerphotonic.com/rapid-prototyping/technical-data.

[P3] Investigating origins of FLIm contrast in atherosclerotic lesions using combined FLIm-Raman Spectroscopy (2019)

Submitted to Frontiers in Cardiovascular Medicine [Julien Bec, Tanveer Ahmed Shaik, Christoph Krafft, Thomas W. Bocklitz, Alba Alfonso-Garcia, Kenneth B. Margulies, Jürgen Popp, Laura Marcu, "Investigating origins of FLIm contrast in atherosclerotic lesions using combined FLIm-Raman Spectroscopy,"]

Erklärungen zu den Eigenanteilen des Promovenden sowie der weiteren Doktoranden/Doktorandinnen als Koautoren an der Publikation.

[1]J. Bec, [2]T. A. Shaik, [3]C. Krafft, [4]T. W. Bocklitz, [5]A. Alfonso-Garcia, [6] J. Popp, [7]Kenneth B. Margulies, and [8]L. Marcu, " Investigating origins of FLIm contrast in atherosclerotic lesions using combined FLIm-Raman Spectroscopy,"								
	Beteiligt an (Zutreffendes ankreuzen)							
	1	2	3	4	5	6	7	8
Konzeption des Forschungsansatzes	X					X		X
Planung der Untersuchungen	X							
Datenerhebung	X	X					X	
Datenanalyse und Interpretation	X	X	X	X	X			
Schreiben des Manuskripts	X	X		X	X	X	X	X
Vorschlag Anrechnung Publikationsäquivalent	1.0							

1 **Investigating origins of FLIm contrast in atherosclerotic lesions using**
2 **combined FLIm-Raman Spectroscopy**

3 **Julien Bec[1,2,3*], Tanveer Ahmed Shaik[3], Christoph Krafft[3], Thomas W. Bocklitz[2,3], Alba**
4 **Alfonso-Garcia[1], Kenneth B. Margulies[4], Jürgen Popp[2,3], Laura Marcu[1]**

5 [1]Department of Biomedical Engineering, University of California, Davis, California, USA

6 [2]Institute of Physical Chemistry and Abbe Center of Photonics (IPC), Friedrich-Schiller-University,
7 Jena, Germany

8 [3]Leibniz Institute of Photonic Technology, D-07745 Jena, Germany

9 [4]Cardiovascular Institute, Perelman School of Medicine, University of Pennsylvania,

10 Philadelphia, PA, USA

11 *** Correspondence:**
12 Corresponding Author
13 jbec@ucdavis.edu

14 **Keywords: Imaging, Spectroscopy, Atherosclerosis, Raman spectroscopy, FLIm, Time resolved**
15 **fluorescence.**

16 **Abstract**

17 **Background:** Fluorescence lifetime imaging (FLIm) is a spectroscopic imaging technique that
18 provides compositional information of the superficial layers of tissue (~100-150 µm). Ex vivo
19 imaging studies of human coronary artery samples performed with a FLIm intravascular imaging
20 catheter demonstrated that different lesions present strong fluorescence contrast. Histology studies
21 have provided indications about the sources of this contrast, but some questions remain unanswered.
22 Raman spectroscopy, a powerful spectroscopic technique able to provide detailed information about
23 the chemical content of biological samples may provide additional insight into the origin of FLIm
24 contrast.

25 **Methods:** Human coronary artery samples were imaged using a combined FLIm-Raman
26 spectroscopy probe. Contrast distribution in FLIm images was analyzed in relationship with
27 histological findings. Raman spectroscopic data was investigated using an endmember identification
28 technique and compared with histological findings. A new workflow based on multivariate
29 regression identified Raman bands related with changes in FLIm contrast in different spectral
30 channels.

31 **Results**: The link between increase of fluorescence lifetime at longer wavelength (546 nm center
32 wavelength) and presence of superficial macrophage foam cells (mFC) was confirmed. The lifetime
33 increase at shorter wavelength (387 nm center wavelength) is only observed in combination with
34 increase of intimal thickness, but is not systematic, thus the exact source of contrast is elusive. Using
35 an endmember decomposition technique, different contributions to the Raman signature of diseased
36 vessels such as hydroxyapatite, collagenous proteins, carotene, and lipids were identified.
37 Comparative FLIm and Raman imaging indicates that the presence of mFC, assessed by FLIm, is not

FLIm-Raman imaging of Atherosclerosis

38 linked with strong changes in Raman spectral features, but lifetime increase at shorter wavelength
39 (387 nm band) was associated with increased presence of cholesterol and carotenes, a finding
40 consistent with LDL accumulation in atherosclerotic lesions.

41 **Conclusions**: Spectroscopic imaging techniques are often used as a complement to morphological
42 imaging. Here, we illustrate how comparative imaging using two spectroscopic imaging techniques
43 provides information that complements histological findings to better understand the origin of FLIm
44 contrast observed in atherosclerotic lesions.

45

46 **INTRODUCTION**

47 Cardiovascular diseases, and in particular atherosclerosis, are a major cause of mortality (1). Despite
48 decades of studies, mechanisms of lesion formation and triggering of acute coronary events are not
49 fully understood. Intravascular imaging techniques, such as intravascular ultrasound or optical
50 coherence tomography (iv-OCT) have provided clinicians and researchers with the ability to assess
51 atherosclerotic lesions in vivo, and efforts are ongoing to further develop imaging techniques to
52 enhance the ability to detect compositional changes relevant to atheroma progression (2). Among
53 these are intravascular declinations of near infrared spectroscopy (3), photoacoustic (4), polarization
54 sensitive OCT (5), endogenous fluorescence (6) or Raman spectroscopy (7). Assessment of lesion
55 composition using fluorescence signature from endogenous fluorescence shows potential for the
56 identification of compositional changes associated with lesion development (8) and was recently
57 implemented into an imaging catheter suitable for the interrogation of coronary arteries (6). Raman
58 spectroscopy is well known for its ability to provide highly specific information about the
59 composition of biological samples, and proof of concept experiments have been investigating its
60 potential as an intravascular imaging technique. Validation of intravascular imaging techniques is
61 typically performed on ex vivo human samples in combination with histological analysis.
62 Nevertheless, this approach presents limitations for spectroscopy techniques that may be sensitive to
63 a variety of molecular species coexisting in lesions. This is particularly critical for fluorescence
64 lifetime, as lifetime characteristics of molecular species are heavily influenced by their
65 microenvironment (9), and therefore measurements of pure compounds in solution may differ
66 significantly from their fluorescence decay properties when present within lesions. In this work, we
67 present a comparative imaging approach that relies on a combined FLIm and Raman imaging probe.
68 Co-registered FLIm and Raman data obtained from ex vivo human coronary samples are used to
69 investigate sources of FLIm contrast, a critical step to support the adoption of FLIm as a tool for the
70 characterization of atherosclerotic lesions.

71

72 **METHODS**

73 **FLIm-Raman instrumentation**

74 The bimodal FLIm-Raman probe used to image the specimens was derived from a previously
75 reported probe and presents a different fiber arrangement and distal end optics (10,11). Briefly, the
76 probe consists of one central fiber surrounded by nine peripheral fibers, all 300 μm-core UV low-OH
77 fluorine doped fused silica. The central fiber does not present a filter and is used for FLIm excitation
78 and collection. One of the peripheral fibers is used for Raman excitation (785 nm) and is combined
79 with a low-pass filter to suppress background fiber signal. Another unfiltered peripheral fiber is

2

80 available for FLIm for separate excitation/collection paths (unused). The seven other fibers,
81 combined with a high-pass filter that rejects the 785 nm excitation light, are collecting the Raman
82 signals. The distal end optic consists of a 2 mm diameter 0.2 NA lithium doped GRIN lens, suitable
83 for use in combination with 355 nm FLIm excitation. The working distance of the probe was
84 determined experimentally at 1- 1.5 mm for Raman and FLIm.

85 The Raman light source consists of a 785 nm multimode laser (0811A100-B model/ Ocean optics
86 (Innovative Photonic solutions)); the output power at the end of the probe was set at 93 mW. The
87 collection fibers, aligned in an SMA connector, were connected to a Raman spectrometer (LS785,
88 Princeton Instruments) with a reflective grating (830 grooves/mm, Princeton Instruments) and
89 equipped with front illuminated CCD open electrode camera (PIXIS -256B Princeton Instruments).
90 Detection was performed using a thermoelectrically cooled detector at -70°C, with 1 sec exposure
91 time and 10 accumulations per measurement point. The spectral range was $200 - 3500$ cm^{-1} with a
92 spectral resolution of 6 cm^{-1}.

93 FLIm was performed using a pulse sampling setup developed by our group (12). This instrument
94 enables the collection of entire fluorescence decay measurements over four different wavelength
95 bands from a single excitation pulse. The excitation was generated using a Nd:YAG microchip Q-
96 switched laser frequency tripled to 355 nm (Teem Photonics, France) with an externally controlled
97 repetition rate of 4 kHz and a pulse energy of ~1.23 µJ . The central wavelength and spectral widths
98 of the instrument bands are determined by a series of dichroic mirrors and bandpass filters and are
99 defined as follows: 387/35 nm, 443/29 nm, 536/38 nm and 628/53 nm and are comparable to spectral
100 bands used for previous studies (13,11,6). A temporal multiplexing scheme using different lengths of
101 delay fibers (1/13/25/37 m) is used so that the contributions from each wavelength bands are delayed
102 in time (60 ns increment), thus enabling the use of a single photodetector (Microchannel plate
103 photomultiplier tube, R3809U-50, Hamamatsu, JP), amplifier (AM-1607-3000, Miteq Inc., USA) and
104 high-speed digitizer (12.5 GS/s, 3 GHz, PXIe-5185, National Instruments, TX). To improve signal to
105 noise ratio, and because acquisition speed is not critical here, 64 waveforms were acquired and
106 averaged for each sample location.

107 **Data acquisition**

108 The bimodal fiber probe has the ability to acquire FLIm and Raman data simultaneously, but the
109 acquisition speeds of both modalities are very different (16 ms/point for FLIm, 10 s/point for
110 Raman). Therefore, the imaging sequence was defined as follows. The combined FLIm – Raman
111 probe was mounted on a 3D X-Y-Z translational stage (PROmech LP28, Parker, Charlotte, NC) used
112 to scan the sample in a grid pattern with a step size of 250 µm x 250 µm. A raster scan of the whole
113 sample was performed with FLIm (typical duration: 1-2 minutes). Based on reconstructed 2D FLIm
114 images, "healthy" locations, characterized by low lifetime in all channels of the instrument, as well as
115 advanced lesions, characterized by lifetime increases in the first/second/third wavebands of the
116 instrument, were identified. Regions of interest (ROI) for Raman data acquisition were defined to
117 include a variety of different expected lesion types. Raman data acquisition was performed using the
118 same 250 µm x 250 µm spatial sampling.

119 **Sample Preparation, imaging, histology**

120 Six human coronary artery samples were obtained from the University of Pennsylvania heart
121 transplant in compliance with current legal requirements and guidelines and was under approval by
122 the University of Pennsylvania Hospital Institutional Review Board as well as UC Davis Biological

FLIm-Raman imaging of Atherosclerosis

123   Use Authorization. Prospective informed consent for research use of heart tissue was obtained from
124   all transplant recipients and next-of-kin in the case of organ donors. Coronary artery samples were
125   harvested from hearts, chilled in isopentane, frozen in liquid nitrogen and stored at -80°C. Before
126   imaging, each sample was thawed, and dissected longitudinally to expose the lumen. The samples
127   were then sutured on a calcium fluoride slide to flatten the lumen surface and prevent tissue motion.
128   Imaging was performed at room temperature and samples were kept hydrated using phosphate buffer
129   saline solution. The entire surface of samples was imaged using FLIm, and Raman spectra were
130   collected from 7291 locations belonging to 19 ROIs.

131   After imaging, the specimens still mounted on the holders were fixed in 10% buffered formalin.
132   Histology processing was performed at the Texas Heart Institute (Houston, TX). Samples were first
133   imaged using high resolution planar X-ray (Faxitron MX-20, Lincolnshire, IL). Samples were then
134   decalcified, sliced in locations corresponding to FLIm-Raman scans, paraffin embedded, and
135   sectioned. Staining using hematoxylin and eosin (H&E) and Movat's pentachrome were performed to
136   visualize plaque morphology. Immunohistochemical staining with CD68 was performed to visualize
137   the presence of macrophage foam cells (mFC).

138   **Data analysis**

139   FLIm data were processed using a constrained least square expansion technique using a set of
140   Laguerre basis functions. This method, described previously by our group, enables fast and robust
141   estimation of fluorescence decay parameters (14). Briefly, fiber probe background was subtracted
142   from the acquired waveform, and the contribution from each channel was separated and processed
143   independently to extract the average lifetime for each point measurement. Fluorescence emission
144   intensity ratio were also computed from the intensity of each individual channel to remove the
145   influence of probe-tissue distance. The processed FLIm dataset therefore consisted of eight FLIm
146   derived parameters (4 average lifetime values, 4 intensity ratio values). En face FLIm images were
147   reconstructed based on raster scanning stage parameters. The 628 nm channel was characterized by a
148   low signal to noise ratio (mean SNR = 20.6 dB) and was therefore not included in the analysis.

149   Histology registration with imaging data was performed based on gross sectioning location. In
150   several sections, calcification visible in histological sections (L2/L4/L5/L9), also visible in planar X-
151   rays of the samples, enabled further confirmation of the histology sections location with respect to
152   spectroscopic imaging data.

153   Raman signal recorded from the samples presented an autofluorescence background as well as
154   etaloning artifacts from the CCD. Raman data were processed as follows. A wavenumber calibration
155   was performed based on spectra from a reference sample (paracetamol) (15). A baseline correction to
156   remove the autofluorescence contribution was performed using a sensitive nonlinear iterative peak
157   algorithm (SNIP) (16). Spectra were truncated to the $650 - 1800$ cm^{-1} wavenumber range and a
158   vector normalization was applied. Etaloning artifacts were removed by reconstructing the spectra
159   from the subset of first 10 artifact-free principal components. Finally, an endmember decomposition
160   was performed with various numbers of endmembers (n = 3 to 10) using the unmixR package in R
161   (17). The residual error sum of square (RESS) was computed, for an increasing number of
162   endmembers, by reconstructing all acquired spectra as a linear combination of the endmembers and
163   comparing the reconstructed spectra with the original data. Increasing the number of endmembers up
164   to seven leads to a large reduction in the RESS, whereas additional endmembers beyond seven do not
165   provide a noticeable reduction in RESS, therefore a number of 7 endmembers was retained for the
166   rest of the study.

167
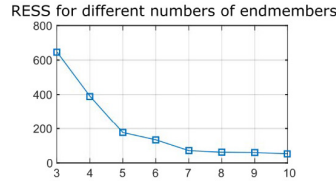
Figure 1: Residual error sum of squares (RESS) for Raman data reconstructed with increasing number of endmembers (n = 3 to 10). Using seven endmembers enables accurate reconstruction of the data.

For each measurement point of the Raman ROIs, a high number of parameters were available (intensity ratio and lifetime parameters for each FLIm spectral band, intensity for each Raman wavenumber). The relationship between variations of fluorescence lifetime values for each spectral channel and variations of Raman spectral features was investigated using linear regression analysis (18). It is expected that Raman spectroscopy provides more information about the samples, and in order to investigate which species are likely to generate FLIm contrast, a regression model predicting Raman intensity based on FLIm information was computed.

As a first step, multicollinearity of FLIm lifetimes across the different wavebands was evaluated by computing the coefficient of multiple determination obtained by regressing the lifetime of each FLIm spectral band on the lifetimes of the other two bands. The highest value was obtained for the 443 nm channel ($R^2 = 0.89$), so this band was excluded from the analysis. The coefficient of multiple determination computed between the LT_{387nm} (lifetime of 387 nm channel) and LT_{546nm} (lifetime of 546 nm channel) was low ($R^2 = 0.16$) so collinearity between lifetime parameters derived from these two spectral bands was not an issue and interpretation of the regression vectors was meaningful (19).

185
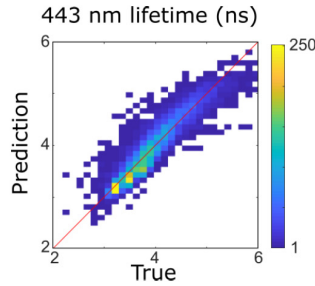
Figure 2: 443 nm lifetime was accurately predicted ($R^2 = 0.89$) from 387 nm and 546 nm lifetimes using a multivariable linear model. It was therefore not considered for the rest of the analysis.

The relationship between the FLIm and Raman datasets was investigated by applying a multivariate multiple linear regression model (18), using LT_{387nm} and LT_{546nm} as independent variables, and the Raman intensities for each wavenumber y as dependent variable, per eq. 1:

$$y_{ik} = b_{0k} + b_{1k}LT_{387nm}(i) + b_{2k}LT_{546nm}(i) + \varepsilon_{ik} \tag{1}$$

5

FLIm-Raman imaging of Atherosclerosis

192 Where i is one of the 7291 measurements, k is one of the 428 wavenumbers of the Raman spectra in
193 the fingerprint region, and ε is an error term.

194 The regression model can be expressed in matrix form:

$$Y = X\beta + \varepsilon \tag{2}$$

195 Y is the 7291x 428 response matrix and consists of the Raman intensity for each measured location
196 and wavenumber. X is the design matrix and consists of a column of ones and the LT_{387nm} and LT_{546nm}
197 for each measured location. β is the 3 x 428 matrix of coefficients where the first row is the y-
198 intercept and the 2nd and 3rd rows correspond to the expected changes in Raman spectra per unit of
199 change in LT_{387nm} and LT_{546nm} respectively. For simplification, the regression was performed on the
200 centered FLIm variables. In that case, the y-intercept (offset) is the mean of the data. A cross
201 validation scheme where each ROI was left out of the analysis was used. The matrix of coefficients $\hat{\beta}$
202 was estimated using an ordinary multivariate normal maximum likelihood estimation using Matlab
203 (2019a, Mathworks, Natick, MA) excluding, in turn, data from a single ROI. The regression model
204 was then used to predict Raman intensities from that ROI (Fig. 6). Mean and standard deviations of
205 the regression vectors computed for each cross validation were computed (Fig. 6)

206 The Raman bands that correlate most with lifetime parameters were determined by computing the
207 fitted Raman spectra:

$$\hat{Y} = X\hat{\beta} \tag{3}$$

208 Where $\hat{Y} = (\hat{y}_{i\,1}, \ldots \hat{y}_{ik}, \ldots, \hat{y}_{i\,428})$ correspond to the predicted Raman intensities for each point
209 measurement.

210 The coefficient of multiple determination $R_k{}^2$, which corresponds to the ratios of regression sum of
211 square divided by the total sum of squares, is computed for each wavenumber k according to equation
212 4:

$$R_k{}^2 = \frac{\sum_{i=1}^{n}(\widehat{y_{ik}} - \overline{y_k})^2}{\sum_{i=1}^{n}(y_{ik} - \overline{y_k})^2} \tag{4}$$

213 Where n is the number of point measurements, and $\overline{y_k}$ is the average of the measured Raman
214 intensities for the kth wavenumber.

215 The coefficient of multiple determination, represented as a function of wavenumber, allowed the
216 identification of regions of the spectra that demonstrated the highest correlations with variations in
217 fluorescence lifetime (Fig. 6).

218 To better identify which Raman spectral band correlated the most with LT_{387nm}, a new, fitted Raman
219 spectra was estimated by replacing the observed LT_{546nm} values in the design matrix by their average
220 value and computing the corresponding fitted Raman spectra and coefficient of determinations using
221 equations 3 and 4. Conversely, the contributions from the LT_{546nm} variations were evaluated by
222 computing the coefficient of determination when replacing the LT_{387nm} values in the design matrix by
223 an average value (Fig. 6).

224 Finally, the measurement points were partitioned in four subsets based on LT_{387nm} and LT_{546nm} values
225 (above or below 4 ns), and the average Raman spectra of each subset were plotted to confirm the
226 differences identified using the method described above (Fig. 7).

227

228 **RESULTS**

229 **1.1 FLIm**

230 FLIm 2D maps of LT_{387nm} and LT_{546nm}, reported for 2 samples (Fig. 3), illustrate the strong contrast
231 observed from different regions of diseased vessel. Comparison with Movat's pentachrome stained
232 sections highlight that LT_{387nm} was only increasing in presence of intimal thickening. It can be noted
233 that some locations characterized by a thickened intima lacked a corresponding increase in lifetime,
234 as illustrated by the fibrocalcific lesions on the left side of ROI2, in correspondence with sections L4
235 and L5. Identification of the main contributor to the observed increase in LT_{387nm} was difficult as
236 many molecular species (various lipids, collagen, elastin) present emission in the near-UV/blue
237 regions. The link between increased LT_{546nm}, and presence of mFCs was confirmed by the
238 localization of superficial mFCs identified from CD68 stained sections. Furthermore, the amount of
239 LT_{546nm} increase was linked with the abundance of mFCs. Another contributor of increased LT_{546nm}
240 was perivascular adipose tissue. Penetration depth of FLIm excitation is low and therefore
241 perivascular adipocytes cannot be excited through the intima, but their signature can be readily
242 identified at the edges of the samples. Analysis of the FLIm signature of perivascular adipose tissue
243 was beyond the scope of this work but inflammation has been documented, and could explain the
244 high lifetime values observed here (20,21).

245

246

7
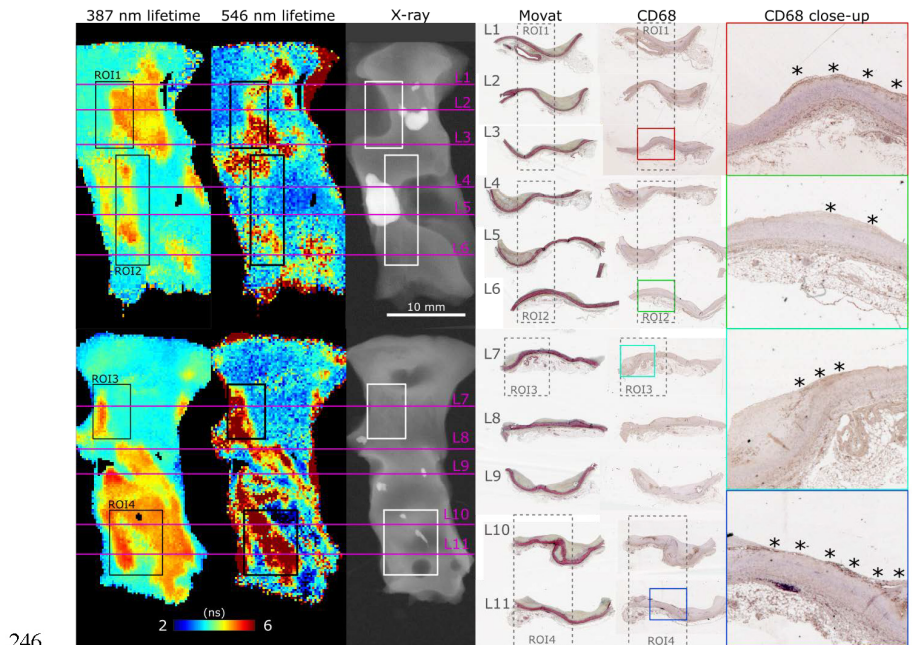
FLIm-Raman imaging of Atherosclerosis

247   **Figure 3: En face FLIm maps of LT$_{387nm}$ and LT$_{546nm}$ for two of the samples illustrate strong**
248   **lifetime contrast in both channels. ROI 1-4 correspond to locations where both FLIm and**
249   **Raman data were acquired. Planar X-ray highlights calcification location. Histology sections**
250   **(L1 to L11) were positioned based on gross sectioning location and presence of calcification.**
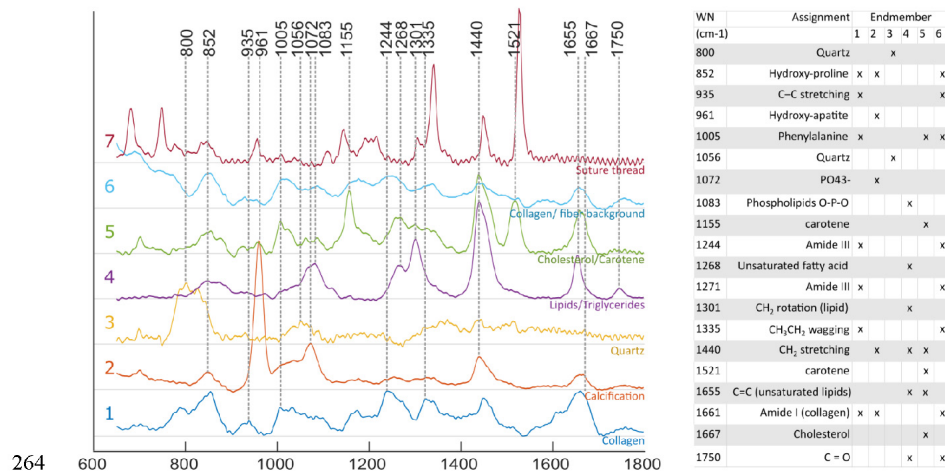251   **Increase of LT$_{387nm}$ was always observed in combination with increase of plaque thickness, but**
252   **some locations presented thick plaque were not linked to an increase in lifetime (L4, L5, left**
253   **side of ROI2). The source of LT$_{387nm}$ was investigated in this study. LT$_{546nm}$ corresponded to**
254   **presence of superficial mFC, visible from the CD68 stained sections (marked with *).**

255   **1.2   Raman**

256   Raman spectra obtained for individual locations were affected by noise despite the extended exposure
257   time, limiting the ability to identify spectral features from single spectral measurements. Using the
258   endmember technique reported here, it was possible to mitigate this limitation by expressing each
259   measurement as a linear combination of the endmembers, and therefore extract robust compositional
260   information at each location. Identification of species contributing to each endmember was
261   performed based on known emission bands (22–24) of species expected in atherosclerotic lesions,
262   combined with spatial information. Four endmembers relate to the actual lesion: collagen,
263   calcification, triglycerides and LDL/carotene (Fig. 4).

WN (cm-1)	Assignment	1	2	3	4	5	6
800	Quartz			x			
852	Hydroxy-proline	x	x				x
935	C–C stretching	x					x
961	Hydroxy-apatite		x				
1005	Phenylalanine	x				x	x
1056	Quartz			x			
1072	PO43-		x				
1083	Phospholipids O-P-O				x		
1155	carotene					x	
1244	Amide III	x					x
1268	Unsaturated fatty acid				x		
1271	Amide III	x					x
1301	CH$_2$ rotation (lipid)				x		
1335	CH$_3$CH$_2$ wagging	x					x
1440	CH$_2$ stretching	x			x	x	
1521	carotene					x	
1655	C=C (unsaturated lipids)				x	x	
1661	Amide I (collagen)	x	x				x
1667	Cholesterol				x		
1750	C = O				x		x

264

265   **Figure 4: Raman spectra of endmembers. Endmember decomposition was consistent with**
266   **species expected from atherosclerotic lesions, and other elements present in the field of view (1:**
267   **collagen, 2: calcification, 3: quartz, 4: lipid rich (nonsaturated triglycerides), 5: Cholesterol/**
268   **Carotene rich, 6: collagen/ fiber background, 7: suture thread).**

269   The advantage of the endmember identification technique is illustrated by the comparison of direct
270   mapping of the 960 cm^{-1} hydroxyapatite peak intensity compared with mapping of the "calcification"
271   endmember abundance (Fig. 5) for a region that presents two small calcification areas. The
272   endmember map demonstrated better quantification with negligible contribution of calcification over
273   the rest of the field of view, whereas the band intensity image presented an elevated background.

274   Mapping of the locations of triglycerides and Cholesterol/Carotene endmembers highlights the
275   differences in their spatial distribution (Fig. 5)
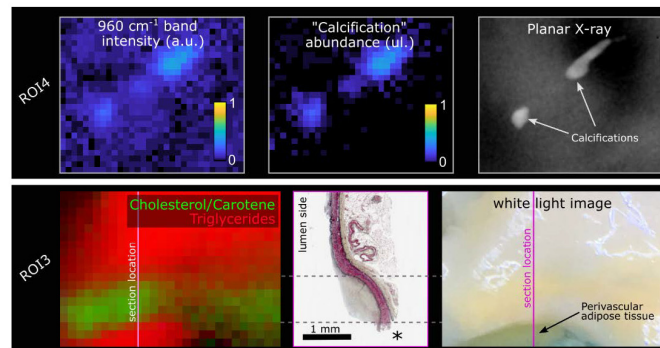
276

277   **Figure 5: Raman hydroxyapatite band intensity map (960 cm⁻¹) compared with "Calcification"**
278   **Endmember abundance map for ROI4 and ground truth location of calcifications obtained**
279   **from planar X-ray. The two small calcifications are easily visible with both methods. The**
280   **endmember image correctly shows no signature from calcifications over the rest of the sample,**
281   **whereas the intensity image shows elevated background (upper panel). In ROI3, the color**
282   **image represents the abundance of endmembers 4 ("triglycerides", red) and 5**
283   **("Cholesterol/carotene", green). Two distinct locations present an abundance of the**
284   **"triglycerides" " endmember. The lower spot corresponds to perivascular adipose tissue, rich**
285   **in triglycerides, exposed at the edge of the sample, easily identified in the white light image, and**
286   **lost during histology processing (location marked as *). The upper area corresponds to a**
287   **diffuse intimal thickening region where perivascular adipose tissue contribute to the Raman**
288   **signature due to the reduced wall thickness. In between, the region of predominant**
289   **Cholesterol/Carotene signature corresponds to the atherosclerotic lesion location (lower panel).**

290

1.3   Combined FLIm-Raman

292   Figure 6 summarizes the findings from the multiple regression analysis. The regression
293   coefficient vectors represented expected variations of Raman spectra with respect to the average
294   spectrum, for respective unitary increases of LT_{387nm} and LT_{546nm}. Low values for a given
295   wavenumber could mean either that the variance of the Raman data for this wavenumber was
296   low, or that the FLIm values did not explain variations in Raman intensity. Conversely, high
297   values of regression coefficients could be linked to high variance in the Raman data. The amount
298   of Raman intensity variance that could be explained by variations in fluorescence lifetime was
299   represented by the coefficient of determination vector. Some of the wavenumbers that stood out
300   in the R^2 plot corresponded to higher values in the regression vectors as well, such as bands
301   "b/c/d/e". Conversely, the 960 cm⁻¹ band, linked with hydroxyapatite, presented high regression
302   coefficient values but an R^2 close to zero, highlighting that observation of the regression
303   coefficients was not sufficient to evaluate the strength of the relationships between datasets. On
304   the contrary, band "a" had the highest R^2, and low regression coefficient values, explained by the
305   low Raman intensity observed in this band.

FLIm-Raman imaging of Atherosclerosis

306 The link between Raman spectral variations and FLIm contrast in specific bands was assessed by
307 computing the predicted Raman intensities varying only one of the lifetime values and replacing
308 the other lifetime by its average value over the entire dataset. Thus, it became clear that LT_{387nm}
309 primarily explained Raman intensity changes, with the exception of band "d" (carotene). This
310 was not unexpected, as LT_{546nm} increases derive mostly from the bright autofluorescence
311 observed from ceroids (25,26), associated with mFCs, which are unlikely to present such a high
312 Raman cross section. It can be noted that the single fluorescence channel prediction described
313 here is not equivalent to performing a linear regression using lifetimes in each spectral band as a
314 single independent variable that would be affected by the correlation between fluorescence
315 lifetimes in different channels due to colocalization of different species in atherosclerotic lesions.

316 Plots of measured vs. predicted Raman intensities (Fig. 6, right pane) demonstrate the predictive
317 value of the regression model. Raman intensities in specific bands were impacted by variations in
318 baseline subtraction between different measurements as well as the vector normalization scheme
319 applied here, where increased emission in one band led to a relative reduction of the other bands.
320 Because none of these effects were modeled by FLIm, the residual variance was expected to
321 remain high even if the underlying relationships between Raman and FLIm signature were
322 properly identified.
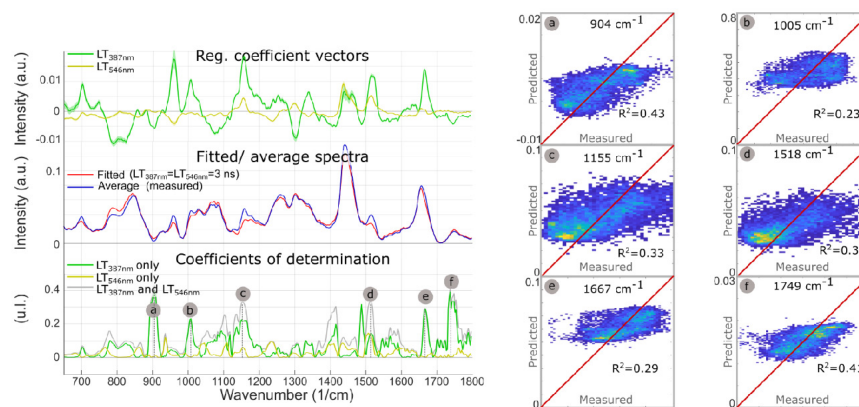
323

324 **Figure 6: LT_{387nm} and LT_{546nm} regression coefficient vectors are expected variations of Raman**
325 **spectra for a respective unit increases of LT_{387nm} and LT_{546nm}. The standard deviation of the**
326 **regression vectors for each cross-validation subset is represented by the shaded area behind**
327 **each curve. The offset vector of the regression is equal to the average Raman spectrum.**
328 **Averaged measured Raman spectrum and modeled spectrum for diffuse intimal thickening**
329 **regions (LT_{387nm} = 3 ns, LT_{546nm} = 3 ns), present few differences. Plot of coefficients of**
330 **determination between measured Raman intensities and Raman intensities predicted from**
331 **LT_{387nm} and LT_{546nm} (gray) demonstrates that the amount of variance that can be explained by**
332 **lifetime variations varies for the different regions of the spectra: as expected, not all Raman**
333 **bands can be predicted from FLIm values. Some locations show a correlation coefficient >0.3**
334 **(a: Protein/ Collagen, b: Phenylalanine/ Carotene, c/d: Carotene, e: Cholesterol, f: Ester bond).**
335 **Prediction using lifetime from only one channel of the instrument (and replacing the other**

336   **lifetime information by the average for the whole dataset) highlights whether one lifetime**
337   **channel contributes most to the prediction (LT$_{387nm}$: a/b/e/f). The predicted vs. measured**
338   **intensities are represented for bands a/b/c/d/e/f (right panel).**

339   Identification of the Raman bands intensity variations highly correlated with fluorescence emission
340   properties, using the regression method described above, were confirmed by subdividing the imaging
341   dataset based on LT$_{387nm}$ and LT$_{546nm}$ values (threshold: 4 ns for both bands). The findings, presented
342   in figure 7, confirmed the validity of the approach. Average Raman spectra for each subset presented
343   differences in correspondence to bands a-f identified from the regression analysis.

344
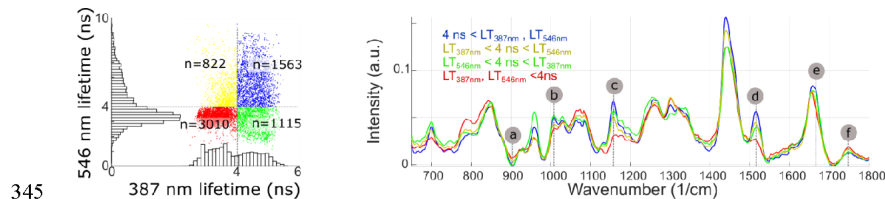
345

346   **Figure 7: Measurement points are partitioned based on LT$_{387nm}$ and LT$_{546nm}$ values (above or**
347   **below 4 ns). The average Raman spectra of each subset present noticeable differences in bands**
348   **identified from the regression analysis (a: Protein/ Collagen, b: Phenylalanine/ Carotene, c/d:**
349   **Carotene, e: Cholesterol, f: Ester bond). Some of the regions where average spectra present**
350   **noticeable differences (785 cm^{-1}, 960 cm^{-1}, 1440cm^{-1}), conversely, only present very weak**
351   **correlation with fluorescence lifetime.**

352

353   **DISCUSSION**

354   Based on the available histology sections alone, the regions presenting the most triglyceride
355   contributions are areas where perivascular adipose tissue is exposed at the edge of the sample, but
356   also regions of minimal intimal thickening. In that last case, the total wall thickness of ~200 μm and
357   the large Raman cross section of lipids compared to proteins explain why the Raman signature is
358   dominated by contributions from tissue located outside of the vessel. The detection of triglycerides in
359   the perivascular adipose tissue is consistent with existing literature (24,28). The second endmember
360   related to lipids, Cholesterol/carotene is expressed in areas of increased intimal thickness as expected
361   from earlier studies (24). Carotene presents a strong Raman cross section due to pre-resonance
362   enhancement and is readily embedded in LDL, and is therefore associated with cholesterol. Cell
363   studies on the tracking of LDL uptake into macrophages have taken advantage of this cholesterol/β-
364   carotene association (29). Applied in the context of biological human samples, the same cholesterol
365   /β-carotene association is useful to track LDL accumulation into the arterial wall.

366   The comparative imaging approach that combined Raman and time resolved fluorescence
367   spectroscopy highlighted relationships between variations in lifetime and variations in select Raman
368   bands. Some characteristics of the Raman data and related processing, namely variations in baseline
369   correction, influence of vector normalization, and detection noise may explain the limited
370   coefficients of multiple determination observed here (<0.4), independently from the validity of the
371   underlying hypothesis. Increase in autofluorescence lifetime at shorter wavelength (LT$_{387nm}$) could be

FLIm-Raman imaging of Atherosclerosis

372   readily associated with increases in carotene and cholesterol content assessed with Raman
373   spectroscopy. This lifetime increase, observed in previous FLIm studies in correspondence with
374   atherosclerotic lesions, was at the time predominantly attributed to increase in structural proteins
375   (13,30). This may stem from the difficulties in properly characterizing lipids contribution in
376   histology studies. Raman spectroscopy, known for its superior ability to perform direct, quantitative,
377   lipid profiling is well suited to address this limitation.

378   An additional benefit of FLIm imaging validation via comparative imaging with Raman spectroscopy
379   rather than histology is that human intervention is reduced. Indeed, sample preparation is minimal
380   and the collected data can be processed via automated data analysis techniques. This aspect compares
381   favourably with histology-based FLIm validation that relies on manual registration and extraction of
382   meaningful histological features. Comparative imaging presents its own set of challenges, as different
383   imaging modalities present different properties, such as penetration depth. Here, 355 nm FLIm
384   excitation is characterized by a low penetration depth in tissue, whereas 785 nm Raman excitation
385   readily propagates in tissue up to 400 – 600 µm. The impact of differences in the interrogated
386   volumes is apparent for the assessment of triglyceride content. The large triglyceride signature in
387   Raman data in healthy regions is related to the proximity of perivascular adipose tissue. In these
388   locations, the shallower penetration of FLIm means that signal from lipids is absent. This
389   confounding factor prevents the accurate quantification of triglyceride content within the FLIm
390   penetration depth.

391   Integration of both modalities in a single optical fiber imaging probe, as reported in this work,
392   presents clear advantages for accurate registration of imaging datasets, but leads to compromises in
393   the optical design for each modality. Additionally, the compact fiber optic probe design is ideally
394   suited to contact measurements on a variety of samples but use of such design for the imaging of
395   irregularly shaped samples leads to variations in the probe to tissue distance across the field of view
396   and thus variations in the noise properties of the data. Improvements in Raman data quality could be
397   achieved by performing an imaging scan where the imaging probe follows a 3D trajectory and
398   maintains a consistent distance with tissue. An alternative approach is an inverted setup, where
399   imaging is performed through a transparent window and thus the sample to probe distance can be
400   accurately maintained (31). Ultimately, a setup able to perform FLIm/Raman imaging on thin (<100
401   µm) tissue sections would also present the benefit of reducing the effect of differences in penetration
402   depths between modalities and therefore represent an ideal tool for future FLIm/Raman comparative
403   imaging, at the expense of additional sample preparation.

404   The current study presents some limitations due to the low number of samples used for this pilot
405   study, and the reported findings may benefit from a follow up study including more samples. The
406   comparative imaging approached presented here requires little human input for data analysis and
407   interpretation beyond the initial definition of the methods, so expansion to a much higher sample
408   number can be achieved more readily than histopathology validation studies where human operations
409   in sample processing, registration and feature extraction present a bottleneck.

410   **CONCLUSION**

411   Comparative imaging of atherosclerotic lesions from ex vivo human samples with FLIm and Raman
412   imaging provides information about the sources of FLIm contrast. More specifically, lifetime
413   increase at shorter wavelength (<400 nm) thought to be linked with increase in structural proteins
414   content could be associated with LDL accumulation in developing lesions. This finding illustrates
415   that histology-based validation of imaging techniques may be complemented by a comparative

416 imaging approach where a high specificity spectroscopic imaging method (Raman) is used to shed
417 light on a high speed/lower specificity modality (FLIm). A key benefit, in addition to the ability to
418 detect molecular species not typically seen in formalin fixed/paraffin embedded histological sections,
419 is that the combination of two co-registered imaging techniques enables the use of data analysis
420 methods that require limited user input beyond data acquisition. It becomes therefore much more
421 practical to increase the sample number than histology-based validation that relies heavily on human
422 operations for sample preparation and feature extraction. In its current implementation, the FLIm-
423 Raman combination presents some limitations that could be addressed with improved sample
424 scanning schemes to facilitate future studies.

425 **DATA AVAILABILITY**

426 The datasets [GENERATED/ANALYZED] for this study can be found in the [NAME OF
427 REPOSITORY] [LINK]. Please see the Data Availability section of the Author guidelines for more
428 details.

429 **AUTHOR CONTRIBUTION**

430 JB proposed the methodology, performed analysis, and wrote the manuscript. TS developed the
431 Raman data acquisition code and supported data analysis. KBM provided tissues for the analysis, JB
432 and TS acquired the multimodal imaging data. TWB performed Raman data pre-processing and
433 provided guidance for comparative data analysis. CK assisted in determining chemical species based
434 on Raman information. TWB, AAG, CK provided input regarding data analysis methods and study
435 findings. TS, TWB, AAG, CK, KBM, JP and LM provided inputs on the revision of the manuscripts

436 **FUNDING**

438

439 **REFERENCES**

440 1. CDC, NCHS. Underlying Cause of Death 1999-2013 on CDC WONDER Online Database,
441 released 2015. (2015)

442 2. Mathur A, Michail M, Stettler R, Crake T, Bourantas CV, Serruys PW, Tenekecioglu E, Zeng Y,
443 Onuma Y, Torii R. Intravascular multimodality imaging: feasibility and role in the evaluation of
444 coronary plaque pathology. *European Heart Journal - Cardiovascular Imaging* (2017) **18**:613–
445 620. doi:10.1093/ehjci/jew330

446 3. Madder RD, Husaini M, Davis AT, Van Oosterhout S, Harnek J, Götberg M, Erlinge D.
447 Detection by near-infrared spectroscopy of large lipid cores at culprit sites in patients with non-
448 st-segment elevation myocardial infarction and unstable angina. *Catheterization and
449 Cardiovascular Interventions* (2015) **86**:1014–1021. doi:10.1002/ccd.25754

450 4. Wang P, Ma T, Slipchenko MN, Liang S, Hui J, Shung KK, Roy S, Sturek M, Zhou Q, Chen Z,
451 et al. High-speed Intravascular Photoacoustic Imaging of Lipid-laden Atherosclerotic Plaque
452 Enabled by a 2-kHz Barium Nitrite Raman Laser. *Sci Rep* (2014) **4**: Available at:
453 http://dx.doi.org/10.1038/srep06889

FLIm-Raman imaging of Atherosclerosis

454   5.   Villiger M, Otsuka K, Karanasos A, Doradla P, Ren J, Lippok N, Shishkov M, Daemen J, Diletti
455   R, van Geuns R-J, et al. Coronary Plaque Microstructure and Composition Modify Optical
456   Polarization. *JACC: Cardiovascular Imaging* (2017) doi:10.1016/j.jcmg.2017.09.023

457   6.   Bec J, Phipps JE, Gorpas D, Ma D, Fatakdawala H, Margulies KB, Southard JA, Marcu L. In
458   vivo label-free structural and biochemical imaging of coronary arteries using an integrated
459   ultrasound and multispectral fluorescence lifetime catheter system. *Scientific Reports* (2017)
460   7:8960. doi:10.1038/s41598-017-08056-0

461   7.   Matthaeus C, Dochow S, Bergner G, Lattermann A, Romeike BFM, Marple ET, Krafft C,
462   Dietzek B, Brehm BR, Popp J. In Vivo Characterization of Atherosclerotic Plaque Depositions
463   by Raman-Probe Spectroscopy and in Vitro Coherent Anti-Stokes Raman Scattering Microscopic
464   Imaging on a Rabbit Model. *Anal Chem* (2012) **84**:7845–7851. doi:10.1021/ac301522d

465   8.   Marcu L. Fluorescence lifetime in cardiovascular diagnostics. *Journal of Biomedical Optics*
466   (2010) **15**:011106–011106. doi:10.1117/1.3327279

467   9.   Draxler S, Lippitsch ME. Lifetime-Based Sensing: Influence of the Microenvironment. *Anal*
468   *Chem* (1996) **68**:753–757. doi:10.1021/ac9507092

469   10. Dochow S, Ma D, Latka I, Bocklitz T, Hartl B, Bec J, Fatakdawala H, Marple E, Urmey K,
470   Wachsmann-Hogiu S, et al. Combined fiber probe for fluorescence lifetime and Raman
471   spectroscopy. *Analytical and bioanalytical chemistry* (2015) **407**:8291–8301.
472   doi:10.1007/s00216-015-8800-5

473   11. Dochow S, Fatakdawala H, Phipps JE, Ma D, Bocklitz T, Schmitt M, Bishop JW, Margulies KB,
474   Marcu L, Popp J. Comparing Raman and fluorescence lifetime spectroscopy from human
475   atherosclerotic lesions using a bimodal probe. *Journal of Biophotonics* (2016) **9**:958–966.
476   doi:10.1002/jbio.201500341

477   12. Yankelevich DR, Ma D, Liu J, Sun Y, Sun Y, Bec J, Elson DS, Marcu L. Design and evaluation
478   of a device for fast multispectral time-resolved fluorescence spectroscopy and imaging. *Review of*
479   *Scientific Instruments* (2014) **85**:

480   13. Fatakdawala H, Gorpas D, Bishop JW, Bec J, Ma D, Southard JA, Margulies KB, Marcu L.
481   Fluorescence Lifetime Imaging Combined with Conventional Intravascular Ultrasound for
482   Enhanced Assessment of Atherosclerotic Plaques: an Ex Vivo Study in Human Coronary
483   Arteries. *Journal of Cardiovascular Translational Research* (2015) doi:10.1007/s12265-015-
484   9627-3

485   14. Liu J, Sun Y, Qi J, Marcu L. A novel method for fast and robust estimation of fluorescence decay
486   dynamics using constrained least-squares deconvolution with Laguerre expansion. *Physics in*
487   *Medicine and Biology* (2012) **57**:843.

488   15. Dörfer Thomas, Bocklitz Thomas, Tarcea Nicolae, Schmitt Michael, Popp Jürgen. Checking and
489   Improving Calibration of Raman Spectra using Chemometric Approaches. *zpch* (2011) **225**:753.
490   doi:10.1524/zpch.2011.0077

491   16. Ryan CG, Clayton E, Griffin WL, Sie SH, Cousens DR. SNIP, a statistics-sensitive background
492   treatment for the quantitative analysis of PIXE spectra in geoscience applications. *Nuclear*

493   *Instruments and Methods in Physics Research Section B: Beam Interactions with Materials and*
494   *Atoms* (1988) **34**:396–402. doi:10.1016/0168-583X(88)90063-8

495   17. McManus C, Fuller S, Beleites C, Hanson BA. unmixR: Hyperspectral Unmixing in R. in

496   18. Rencher AC, Christensen WF. *Methods of Multivariate Analysis.* Hoboken, New Jersey: Wiley
497   (2012).

498   19. Yoo W, Mayberry R, Bae S, Singh K, Peter He Q, Lillard JW Jr. A Study of Effects of
499   MultiCollinearity in the Multivariable Analysis. *Int J Appl Sci Technol* (2014) **4**:9–19.

500   20. Weisberg SP, McCann D, Desai M, Rosenbaum M, Leibel RL, Ferrante AW Jr. Obesity is
501   associated with macrophage accumulation in adipose tissue. *J Clin Invest* (2003) **112**:1796–1808.
502   doi:10.1172/JCI19246

503   21. Britton KA, Fox CS. Perivascular adipose tissue and vascular disease. *Clin Lipidol* (2011) **6**:79–
504   91. doi:10.2217/clp.10.89

505   22. Krafft C, Neudert L, Simat T, Salzer R. Near infrared Raman spectra of human brain lipids.
506   *Spectrochimica Acta Part A: Molecular and Biomolecular Spectroscopy* (2005) **61**:1529–1535.
507   doi:10.1016/j.saa.2004.11.017

508   23. Rehman I ur., Movasaghi Zanyar, Rehman Shazza. Vibrational spectroscopy for tissue analysis.
509   (2013) Available at: http://www.crcnetbase.com/isbn/9781439836088

510   24. Lattermann A, Matthäus C, Bergner N, Beleites C, Romeike BF, Krafft C, Brehm BR, Popp J.
511   Characterization of atherosclerotic plaque depositions by Raman and FTIR imaging. *Journal of*
512   *Biophotonics* (2013) **6**:110–121. doi:10.1002/jbio.201200146

513   25. Verbunt RJAM, Fitzmaurice MA, Kramer JR, Ratliff NB, Kittrell C, Taroni P, Cothren RM,
514   Baraga J, Feld M. Characterization of ultraviolet laser-induced autofluorescence of ceroid
515   deposits and other structures in atherosclerotic plaques as a potential diagnostic for laser
516   angiosurgery. *American Heart Journal* (1992) **123**:208–216. doi:10.1016/0002-8703(92)90767-P

517   26. Haka AS, Kramer JR, Dasari RR, Fitzmaurice M. Mechanism of ceroid formation in
518   atherosclerotic plaque: in situ studies using a combination of Raman and fluorescence
519   spectroscopy. *Journal of Biomedical Optics* (2011) **16**:011011-011011–7. doi:10.1117/1.3524304

520   27. Brown NK, Zhou Z, Zhang J, Zeng R, Wu J, Eitzman DT, Chen YE, Chang L. Perivascular
521   adipose tissue in vascular function and disease: a review of current research and animal models.
522   *Arterioscler Thromb Vasc Biol* (2014) **34**:1621–1630. doi:10.1161/ATVBAHA.114.303029

523   28. Buschman HP, Deinum G, Motz JT, Fitzmaurice M, Kramer JR, van der Laarse A, Bruschke
524   AV, Feld MS. Raman microspectroscopy of human coronary atherosclerosis: Biochemical
525   assessment of cellular and extracellular morphologic structures in situ. *Cardiovascular Pathology*
526   (2001) **10**:69–82. doi:10.1016/S1054-8807(01)00064-3

527   29. Stiebing C, Schmölz L, Wallert M, Matthäus C, Lorkowski S, Popp J. Raman imaging of
528   macrophages incubated with triglyceride-enriched oxLDL visualizes translocation of lipids

529   between endocytic vesicles and lipid droplets. *J Lipid Res* (2017) **58**:876–883.
530   doi:10.1194/jlr.M071688

531   30. Park J, Pande P, Shrestha S, Clubb F, Applegate BE, Jo JA. Biochemical characterization of
532   atherosclerotic plaques by endogenous multispectral fluorescence lifetime imaging microscopy.
533   *Atherosclerosis* (2012) **220**:394–401. doi:10.1016/j.atherosclerosis.2011.10.034

534   31. Shipp DW, Rakha EA, Koloydenko AA, Macmillan RD, Ellis IO, Notingher I. Intra-operative
535   spectroscopic assessment of surgical margins during breast conserving surgery. *Breast Cancer*
536   *Research* (2018) **20**:69. doi:10.1186/s13058-018-1002-2

537

List of publications and conference contributions

Peer-reviewed publications

1.
J. Bec, H. Xie, D. R. Yankelevich, F. Zhou, Y. Sun, N. Ghata, R. Aldredge, and L. Marcu, "Design, construction, and validation of a rotary multifunctional intravascular diagnostic catheter combining multispectral fluorescence lifetime imaging and intravascular ultrasound," Journal of Biomedical Optics **17**, 106012–1 (2012).

2.
Y. Sun, H. Xie, J. Liu, M. Lam, A. J. Chaudhari, F. Zhou, J. Bec, D. R. Yankelevich, A. Dobbie, S. L. Tinling, R. F. Gandour-Edwards, W. L. Monsky, D. Gregory Farwell, and L. Marcu, "In vivo validation of a bimodal technique combining time-resolved fluorescence spectroscopy and ultrasonic backscatter microscopy for diagnosis of oral carcinoma," Journal of Biomedical Optics **17**, 116003–116003 (2012).

3.
H. Xie, J. Bec, J. Liu, Y. Sun, M. Lam, D. R. Yankelevich, and L. Marcu, "Multispectral scanning time-resolved fluorescence spectroscopy (TRFS) technique for intravascular diagnosis," Biomed. Opt. Express **3**, 1521–1533 (2012).

4.
J. Bec, D. M. Ma, D. R. Yankelevich, J. Liu, W. T. Ferrier, J. Southard, and L. Marcu, "Multispectral fluorescence lifetime imaging system for intravascular diagnostics with ultrasound guidance: in vivo validation in swine arteries," Journal of Biophotonics n/a-n/a (2013).

5.
H. Fatakdawala, S. Poti, F. Zhou, Y. Sun, J. Bec, J. Liu, D. R. Yankelevich, S. P. Tinling, R. F. Gandour-Edwards, D. G. Farwell, and L. Marcu, "Multimodal in vivo imaging of oral cancer using fluorescence lifetime, photoacoustic and ultrasound techniques," Biomed. Opt. Express **4**, 1724–1741 (2013).

6.
C. Li, K. Di, J. Bec, and S. R. Cherry, "X-ray luminescence optical tomography imaging: experimental studies," Opt. Lett. **38**, 2339–2341 (2013).

7.
A. Ferrero, Q. Peng, J. Zhou, G. Burkett, J. Bec, P. Gazi, M. G. B. Sumanasena, F. Godinez, J. Boone, and R. Badawi, "Performance characterization of a new generation breast and extremity PET/CT scanner," Journal of Nuclear Medicine **55**, 2144–2144 (2014).

8.
N. Ghata, R. C. Aldredge, J. Bec, and L. Marcu, "Computational analysis of the effectiveness of blood flushing with saline injection from an intravascular diagnostic catheter," International Journal for Numerical Methods in Biomedical Engineering n/a-n/a (2014).

9.
D. Ma, J. Bec, D. R. Yankelevich, D. Gorpas, H. Fatakdawala, and L. Marcu, "Rotational multispectral fluorescence lifetime imaging and intravascular

ultrasound: bimodal system for intravascular applications," Journal of Biomedical Optics **19**, 066004–066004 (2014).

10.

D. R. Yankelevich, D. Ma, J. Liu, Y. Sun, Y. Sun, J. Bec, D. S. Elson, and L. Marcu, "Design and evaluation of a device for fast multispectral time-resolved fluorescence spectroscopy and imaging," Review of Scientific Instruments **85**, (2014).

11.

A. Z. Kyme, K. Gong, M. S. Judenhofer, J. Bec, J. Du, J. Qi, S. R. Cherry, and S. R. Meikle, "Open-field mouse brain PET: Design considerations and detector development," 2015 IEEE Nuclear Science Symposium and Medical Imaging Conference (NSS/MIC) 1–3 (2015).

12.

J. Bec, D. Ma, D. Yankelevich, W. T. Ferrier, J. Southard, and L. Marcu, "In vivo high speed multispectral fluorescence lifetime imaging (FLIm) of swine coronary arteries," in *Optics in the Life Sciences*, OSA Technical Digest (Online) (Optical Society of America, 2015), p. BW3A.6.

13.

S. Dochow, D. Ma, I. Latka, T. Bocklitz, B. Hartl, J. Bec, H. Fatakdawala, E. Marple, K. Urmey, S. Wachsmann-Hogiu, M. Schmitt, L. Marcu, and J. Popp, "Combined fiber probe for fluorescence lifetime and Raman spectroscopy," Analytical and bioanalytical chemistry **407**, 8291–8301 (2015).

14.

J. Du, J. P. Schmall, K. Di, Y. Yang, M. Judenhofer, J. Bec, S. Buckley, C. Jackson, and S. R. Cherry, "Design and optimization of a high-resolution PET detector module for small-animal PET based on a 12 × 12 silicon photomultiplier array," Biomedical Physics & Engineering Express **1**, 045003 (2015).

15.

H. Fatakdawala, D. Gorpas, J. W. Bishop, J. Bec, D. Ma, J. A. Southard, K. B. Margulies, and L. Marcu, "Fluorescence Lifetime Imaging Combined with Conventional Intravascular Ultrasound for Enhanced Assessment of Atherosclerotic Plaques: an Ex Vivo Study in Human Coronary Arteries," Journal of Cardiovascular Translational Research (2015).

16.

D. Gorpas, H. Fatakdawala, J. Bec, Dinglong Ma, D. R. Yankelevich, Jinyi Qi, and L. Marcu, "Fluorescence Lifetime Imaging and Intravascular Ultrasound: Co-Registration Study Using Ex Vivo Human Coronaries," Medical Imaging, IEEE Transactions on **34**, 156–166 (2015).

17.

D. Ma, J. Bec, D. Gorpas, D. Yankelevich, and L. Marcu, "Technique for real-time tissue characterization based on scanning multispectral fluorescence lifetime spectroscopy (ms-TRFS)," Biomed. Opt. Express **6**, 987–1002 (2015).

18.

D. Gorpas, D. Ma, J. Bec, D. Yankelevich, and L. Marcu, "Real-Time Visualization of Tissue Surface Biochemical Features Derived from Fluorescence Lifetime Measurements," IEEE Transactions on Medical Imaging **PP**, 1–1 (2016).

19.

Y. Yang, J. Bec, J. zhou, M. Zhang, M. S. Judenhofer, X. Bai, K. Di, Y. Wu, M. Rodriguez, P. Dokhale, K. Shah, R. Farrell, J. Qi, and S. R. Cherry, "A high

resolution prototype small-animal PET scanner dedicated to mouse brain imaging," Journal of Nuclear Medicine (2016).

20.

J. Bec, J. E. Phipps, D. Gorpas, D. Ma, H. Fatakdawala, K. B. Margulies, J. A. Southard, and L. Marcu, "In vivo label-free structural and biochemical imaging of coronary arteries using an integrated ultrasound and multispectral fluorescence lifetime catheter system," Scientific Reports **7**, 8960 (2017).

21.

A. Z. Kyme, M. S. Judenhofer, K. Gong, J. Bec, A. Selfridge, J. Du, J. Qi, S. R. Cherry, and S. R. Meikle, "Open-field mouse brain PET: design optimisation and detector characterisation," Physics in Medicine & Biology **62**, 6207–6225 (2017).

22.

B. E. Sherlock, J. E. Phipps, J. Bec, and L. Marcu, "Simultaneous, label-free, multispectral fluorescence lifetime imaging and optical coherence tomography using a double-clad fiber," Opt. Lett. **42**, 3753–3756 (2017).

23.

X. Zhang, E. Berg, J. Bec, M. Judenhofer, M. Kapusta, M. Schmand, M. Casey, R. Badawi, S. Cherry, and J. Qi, "First Pre-Clinical Study of Total-Body Dynamic PET Imaging using the mini-EXPLORER Scanner," Journal of Nuclear Medicine **58**, 394–394 (2017).

24.

E. Berg, X. Zhang, J. Bec, M. S. Judenhofer, B. Patel, Q. Peng, M. Kapusta, M. Schmand, M. E. Casey, A. F. Tarantal, J. Qi, R. D. Badawi, and S. R. Cherry, "Development and Evaluation of mini-EXPLORER: A Long Axial Field-of-View PET Scanner for Nonhuman Primate Imaging," J Nucl Med **59**, 993–998 (2018).

25.

D. Gorpas, P. Davari, J. Bec, M. A. Fung, L. Marcu, D. G. Farwell, and N. Fazel, "Time-resolved fluorescence spectroscopy for the diagnosis of oral lichen planus," Clinical and Experimental Dermatology **43**, 546–552 (2018).

26.

J. L. Lagarto, J. E. Phipps, L. Faller, D. Ma, J. Unger, J. Bec, S. Griffey, J. Sorger, D. G. Farwell, and L. Marcu, "Electrocautery effects on fluorescence lifetime measurements: An in vivo study in the oral cavity," Journal of Photochemistry and Photobiology B: Biology **185**, 90–99 (2018).

27.

A. Alfonso-Garcia, J. Bec, S. Sridharan, B. Hartl, J. Unger, M. Bobinski, M. Lechpammer, F. Girgis, J. Boggan, and L. Marcu, "Real-time augmented reality for delineation of surgical margins during neurosurgery using autofluorescence lifetime contrast," Journal of Biophotonics **0**, e201900108 (2019).

28.

A. Alfonso-Garcia, C. Li, J. Bec, D. Yankelevich, L. Marcu, and B. Sherlock, "Fiber-based platform for synchronous imaging of endogenous and exogenous fluorescence of biological tissue," Opt. Lett. **44**, 3350–3353 (2019).

29.

J. Bec, C. Li, and L. Marcu, "Broadband, freeform focusing micro-optics for a side-viewing imaging catheter," Opt. Lett. **44**, 4961–4964 (2019).

30.

D. Gorpas, J. Phipps, J. Bec, D. Ma, S. Dochow, D. Yankelevich, J. Sorger, J. Popp, A. Bewley, R. Gandour-Edwards, L. Marcu, and D. G. Farwell, "Autofluorescence lifetime augmented reality as a means for real-time robotic surgery guidance in human patients," Scientific Reports **9**, 1187 (2019).

31.

B. E. Sherlock, C. Li, X. Zhou, A. Alfonso-Garcia, J. Bec, D. Yankelevich, and L. Marcu, "Multiscale, multispectral fluorescence lifetime imaging using a double-clad fiber," Opt. Lett. **44**, 2302–2305 (2019).

Conference presentations

1.
J. Bec, H.Xi, D. R. Yankelevitch, F. Zhou, Y. Sun, N. Ghata, R. Aldredge, and L. Marcu, "Design, construction, and validation of a multimodal intravascular diagnostic catheter combining IVUS and fluorescence lifetime spectroscopy detection channels," 7883D-78, Photonics West (2011), Oral presentation.

3.
J. Bec, D. Ma, D. R. Yankelevitch, and L. Marcu, "Design and validation of a small-profile rotational catheter for combined fluorescence lifetime imaging (FLIm) and intravascular ultrasound (IVUS) imaging of coronary arteries," 8565-135, Photonics West (2013), Oral presentation.

4.
J. Bec, D. Ma, D. R. Yankelevitch, D. Gorpas, W.T. Ferrier, J.A. Southard, and L. Marcu, "In-vivo validation of fluorescence lifetime imaging (FLIm) of coronary arteries in swine," 9303-523, Photonics West (2015), Oral presentation.

5.
J. Bec, D. Ma, D. R. Yankelevitch, D. Gorpas, W.T. Ferrier, J.A. Southard, and L. Marcu, " In vivo high-speed multispectral fluorescence lifetime imaging (FLIm) of swine coronary arteries," 2209002, OSA: Optics in the Life Sciences Congress (2015), Oral presentation.

6.
J. Bec, D. Gorpas, H. Fatakdawala, J.E. Phipps, D. Ma, D. R. Yankelevitch, J.A. Southard, and L. Marcu, " In-vivo validation of a multi-modal fluorescence lifetime imaging (FLIm)-IVUS catheter in swine coronary arteries," 9689-103, Photonics West (2016), Oral presentation.

7.
J. Bec, J.E. Phipps, K. B. Margulies, and L. Marcu, " Multivariate analysis of multispectral fluorescence lifetime imaging (FLIm) data: application to atherosclerotic plaque staging," 10042-24, Photonics West (2017), Oral presentation.

8.
J. Bec, J.E. Phipps, J. Unger, D. Vela, L. M. Buja, J.A. Southard, K.B. Margulies, and L. Marcu," FLIm and IVUS see things that OCT and NIRS do not," Optics in Cardiology (2017), Oral presentation.

9.
J. Bec, C. Li, B. Sherlock, and L. Marcu, " Freeform broad-band focusing micro optics: application to catheter-based fluorescence lifetime imaging of coronary arteries," 10471-3, Photonics West (2018), Oral presentation.

10.
J. Bec, D. Henry, R.D. Badawi and S.R.Cherry " Optical motion tracking for use with the EXPLORER total-body PET scanner" 1717, SNMMI (2018), Oral presentation.

11.
J. Bec, C. Li, and L. Marcu, " Systematic assessment of FLIm signature of ex-vivo human coronary atherosclerotic lesions: towards label-free quantitative

assessment of lesion composition," 10855-12, Photonics West (2019), Oral presentation.

Acknowledgments

I want to thank Prof. Dr. Laura Marcu for the opportunity to work in her research lab and for her continuing support and guidance over the last ten years. I also would like to thank Prof. Dr. Jürgen Popp for giving me the opportunity to work on my doctoral thesis in collaboration with his group.

I want to thank Dr. Diego Yankelevitch, Dr. Dinglong "Michael" Ma, Dr. Dimitris Gorpas, Dr. Hussein Fatakdawala, Dr. Jennifer Phipps, Dr. Jakob Unger, Dr. Benjamin Sherlock, Cai Li for the many discussions and fruitful collaboration over the years, pushing intravascular FLIm applications forward

My gratitude also goes to all past and present members of the UC Davis biophotonics Laboratory/ Marcu Lab with which I have enjoyed collaborating over the years on such a wide variety of research projects. The friendly and positive working environment you all helped to provide was key to navigate the sometimes thrilling, and sometimes trying times of academic research.

I would like to extend my thanks to our external collaborators. Dr. Jeffrey Southard, Dr. Bill Ferrier, and Dr. Deborah Vela's dedication and expertise in the fields of cardiovascular medicine, veterinary medicine, and pathology have been key to this work.

On a personal note, I would like to thank all my dear friends from Grenoble, Lyon, Turin, Modena, Paris, Davis, Jena and other places where I was fortunate to get to spend some time.

Above all, I would like to thank Dr. Emilie Roncali, outstanding scientist and amazing life partner. I cannot think of a better person to deal with the challenges and enjoy the rewards of two academic careers and three rambunctious kids. We got this!

Erklärungen

Selbstständigkeitserklärung

Ich erkläre, dass ich die vorliegende Arbeit selbstständig und unter Verwendung der angegebenen Hilfsmittel, persönlichen Mitteilungen und Quellen angefertigt habe.

Julien BEC

_____

(Datum)   (Ort)   (Unterschrift)

Erklärung zu den Eigenanteilen des Promovenden/der Promovendin sowie der weiteren Doktoranden/Doktorandinnen als Koautoren an den Publikationen und Zweitpublikationsrechten bei einer kumulativen Dissertation

Für alle in dieser kumulativen Dissertation verwendeten Manuskripte liegen die notwendigen Genehmigungen der Verlage („Reprint permissions") für die Zweitpublikation vor.

Die Co-Autoren der in dieser kumulativen Dissertation verwendeten Manuskripte sind sowohl über die Nutzung, als auch über die oben angegebenen Eigenanteile informiert und stimmen dem zu (es wird empfohlen, diese grundsätzliche Zustimmung bereits mit Einreichung der Veröffentlichung einzuholen bzw. die Gewichtung der Anteile parallel zur Einreihung zu klären).Die Anteile der Co-Autoren an den Publikationen sind in diesem Kapitel aufgeführt.

Julien BEC

_____

(Datum)   (Ort)   (Unterschrift)

Einverständniserklärung des Betreuers

Ich bin mit der Abfassung der Dissertation als publikationsbasiert, d.h. kumulativ, einverstanden und bestätige die vorstehenden Angaben. Eine entsprechend begründete Befürwortung mit Angabe des wissenschaftlichen Anteils des Doktoranden/der Doktorandin an den verwendeten Publikationen werde ich parallel an den Rat der Fakultät der Chemisch Geowissenschaftlichen Fakultät richten.

Prof. Dr. Jürgen Popp _____

(Datum) (Ort) (Unterschrift)